Charles University in Prague
Faculty of Mathematics and Physics
Astronomical Institute of the Charles University

Doctoral Thesis

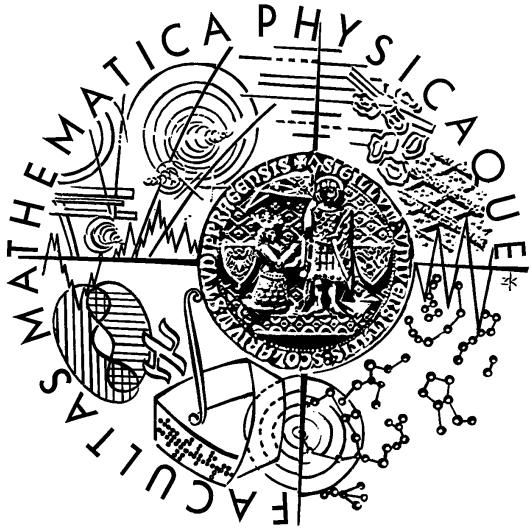

Radomír Šmída

Cosmic-Ray Physics with the Pierre Auger Observatory

Advisors:
RNDr. Jiří Grygar, CSc.,
doc. Jan Řídký, CSc.

Institute of Physics
Academy of Sciences of the Czech Republic

Prague 2009

I declare that I have worked out this doctoral thesis myself using only the literature stated. I agree with being it used for educational purposes.

Prague, May 21st, 2009

Acknowledgements

I would like to express my gratitude to all those who gave me the possibility to complete this thesis.

First of all I am grateful to Jiří Grygar and Jan Řídký for their steady support and encouragement which have been essential for the thesis preparation.

I owe a debt of gratitude to my friends and colleagues, particularly Martina Boháčová, Dalibor Nosek, Michael Prouza and Petr Trávníček, who have provided invaluable suggestions and feedbacks.

I deeply appreciate thoughtful and constructive comments made by colleagues from the Pierre Auger Observatory.

Finally I express sincere thanks to my parents for their love and confidence through the past years.

This work was supported by the grants KJB300100801 of the Grant Agency of the Academy of Sciences, MSMT LA08016 and MSMT LC527 of the Ministry of Education, Youth and Sports of the Czech Republic.

Contents

Thesis Overview

The origin and nature of the cosmic rays with the highest energies is one of the most enigmatic questions in physics. These particles are measured indirectly due to the observation of extensive air showers developing in the Earth's atmosphere. Currently the largest and most advanced experiment designed to investigate the highest energy cosmic rays and to resolve some of these problems is the Pierre Auger Observatory. The thesis is dedicated in particular to the study of the performance of the telescopes observing fluorescence emission from extensive air showers.

The work consists from two distinct parts. The first one is concentrated on the measurements and the origin of cosmic rays. It starts with a review of the history of cosmic ray observations and subsequently follows the description of cosmic-ray detection. The next part deals with the origin of cosmic rays in the Universe and their propagation from still unknown sources towards the Earth. The results of the study of particle and antiparticle tracking are focused on the most energetic cosmic rays, which are particularly interesting because of their smaller angular deflection in the Galactic magnetic field.

The first part of the work is concluded by a brief account on the Pierre Auger Observatory design and function, followed by the presentation of current results. The analysis of space-time distribution of observed gamma-ray extragalactic and galactic sources and cosmic rays is presented in chapter six.

The second part of the work deals with the fluorescence detector, which consists of telescopes observing fluorescence light from air showers in the atmosphere. The performance of the fluorescence detector is described and analyzed in detail. The obtained results led to significant improvement of detector performance and were used also in physical analysis.

Further the background light exposure and its time evolution are discussed. The importance of this analysis is essential for the detector sensitivity as was recently observed by the absolute calibration of the fluorescence telescopes.

The last chapter summarizes major achievements of the presented work. Chapters 3 and 6 in the first part and whole second part starting with chapter 7 are based on the results of author's work.

Chapter 1

Cosmic Rays

Cosmic rays are relativistic and mostly charged particles bombarding Earth's atmosphere from the outer space. They originate outside the Earth, but because of a distortion of their trajectories by chaotic magnetic fields in interstellar space their arrival directions do not point back to their site of origin. Nevertheless they bring important information about very energetic processes in the Universe and about the sources, interstellar space and magnetic fields. The observation of cosmic rays helps to explore the Universe and to reveal some of its mysteries. An explanation of the origin and nature of the most energetic cosmic rays is important not only to astronomers, but also to particle physicists. Their efforts are now united in rapidly evolving new field of science - astroparticle physics.

1.1 Discovery of Cosmic Rays

The history of cosmic rays has started with an exploration of charged gases in closed vessels at the beginning of 20th century. Two Canadian groups, McLennan and Burton from the University of Toronto [McL03] and Rutherford and Cooke from McGill University [Rut03] noticed in 1903 that the leakage of electric charge from an electroscope within an air-tight metal chamber could be reduced as much as 30% by enclosing the chamber within several centimeters thick metal shield. An additional lead failed to reduce the radiation further. The loss of the charge of the enclosed electroscope was due to some highly penetrating rays. It was attributed to radioactive materials in the ground or in the air.

The most penetrating known radiation known at that time was γ-ray with well-explored attenuation coefficient in the air. When γ-ray radiation passes through any matter, its intensity exponentially decreases. Such exponential decrease should be observed also when air ionization is measured.

Within following years it was found that the radiation did not decrease as rapidly with an altitude as was expected. The first report upon this point was made by Dutch Jesuit priest and physicist Theodor Wulf [Wul09], who made measurements in a lime-pit near the town Valkenburg and then at the top of the Eiffel Tower, the highest construction in the world in those days. Later Swiss physicist Gockel [Goc10] took an enclosed electroscope above the ground in a balloon.

Figure 1.1: Path of Hess's flight in the balloon Böhmen on August 7, 1912. Flight started from Ústi nad Labem (Aussig).

Austrian physicist Victor Franz Hess, working at the Physical Institute in Vienna in the field of radioactivity, had speculated whether the source of ionization is in the sky rather than in the Earth's crust. He realized ten balloon flights (five of them during night) with pressure and thermal stable instruments: two flights in 1911, seven in 1912, and one in 1913. During his first six flights he did not succeed to reach sufficient height above the ground. Before the seventh flight he filled a bag of the balloon named Böhmen with hydrogen instead of coalgas and ascended up to the altitude over 5 km (without an air mask). The balloon started its flight on August 7, 1912 from Ústí nad Labem (Aussig) with V. Hess, aviator W. Hoffory and meteorologist E. Wolf. The path of balloon flight is shown in Fig. 1.1.

Hess found that although electroscope's rate of discharge decreased initially up to about 610 m, thereafter it increased considerably, being four times larger at 4880 m than at sea level (see Fig. 1.2). He concluded, that the radiation of very high penetrating power enters into the atmosphere from above [Hes12]: *"The results of the present observations seem to be most readily explained by the assumption that a radiation of very high penetrating power enters our atmosphere from above, and still produces in the lower layers a part of the ionization observed in closed vessels."*

After five balloon flights made during night and one during an almost total eclipse of the Sun on April 12, 1912 Hess further concluded that, since he observed no change of the rate of discharge, the Sun could not itself be the main source of

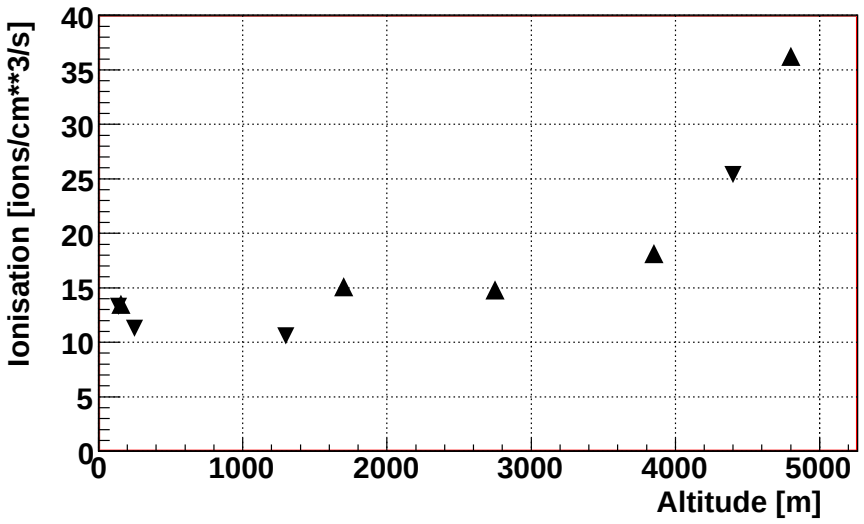

Figure 1.2: Observation of air ionisation measured by Hess in 1912. Depicted are averaged measurements from two detectors. Up/down triangles are for ascension/descent of the balloon Böhmen.

the radiation.

His results were confirmed by German physicist Werner Kolhörster [Kol13]. He measured the increase of the ionisation up to 9 km. This was a clear evidence that sources of the ionising radiation must be located well above the Earth's ground.

Hess's hypothesis about radiation coming from outer space did not receive general acceptance at the time he proposed it. Other propositions, such as lifting of radioactive sources from the ground into upper parts of the atmosphere, were still considered. But improved research after World War I supported Hess's suggestion.

In the twenties American physicist Robert Millikan made further studies by launching unmanned balloons. He reported no rise in the level of the radiation. His findings were correct, but it turned out that the level of cosmic radiation in studied regions was unusually low. Finally in 1925, Millikan performed experiments of submerging electroscopes in lakes at different depths and found that a depth of water equal in mass to the difference in atmospheric altitudes gave the same readings [Mil26]. Thus it was proved that rays must come from above and he named them "cosmic rays" (instead of usual Höhenstrahlung or Ultrastrahlung).

1.2 Investigation of Cosmic Ray Properties

For many years there was discussion whether cosmic rays are neutral γ-rays or charged particles. Millikan supported an idea that cosmic rays consist from high-energy γ-rays with some secondary electrons produced by Compton scattering of the γ-rays.

The invention of the Geiger-Müller detector in 1929 enabled a detection of individual cosmic rays. Walther Bothe and W. Kolhörster built a coincidence counter by using two counters, one placed above the other [Bot29]. They found that simul-

TABLE I. *Cosmic ray intensity at different localities*
(Ions per cc per sec. through 5 cm Pb, 2.5 cm Cu and 0.5 cm Fe)

Location	Lat.	Long.	Elev.	Barom.	I_C	I_L	Date
1 Mt. Evans	40°N	106°W	14,200ft	17.61in	6.88 ions	0.57	9/31
2 Summit Lake	40 N	106 W	12,700	18.70	5.84	0.34	9/31
3 Denver	40 N	105 W	5300	24.8	2.93	—	9/31
4 Jungfraujoch	47 N	6 E	11,400	19.70	5.08	0.51	10/31
5 Haleakala	21 N	156 W	9300	21.47	3.35 ± 0.05	0.60	4/32
6 Idlewild	21 N	156 W	4200	25.99	2.40 ± 0.05	0.37	4/32
7 Honolulu	21 N	158 W	70	30.09	1.89 ± 0.02	0.11	4/32
8 S. S. Aorangi	4 S	173 W	60	29.65	1.83 ± 0.05	0.32	4/32
9 Southern Alps	44 S	170 E	6700	23.69	3.39 ± 0.05	0.22	4/32
10 Southern Alps	44 S	170 E	3900	26.10	2.70 ± 0.04	0.21	4/32
11 Dunedin	46 S	170 E	80	30.08	2.16 ± 0.03	0.11	4/32
12 Wellington	41 S	175 E	400	29.85	2.16 ± 0.03	0.12	5/32

Figure 1.3: Latitude dependence of cosmic ray intensity. Local radiation sources were shielded by copper and lead shells. Taken from [Com32].

taneous discharges of the two detectors occurred very frequently, even when a strong absorber (a gold tablet) was placed between the detectors. The experiment strongly indicated that these particles are charged with sufficiently penetrating power, so they have to be very energetic because of their long ranges in the matter.

If charged particles constitute a majority of cosmic rays, they will be deflected by the geomagnetic field and the cosmic-ray flux will be strongest at the poles and weakest at the equator. In 1932 Arthur Holly Compton presented a result of series of his observations which showed variation of cosmic ray flux with the latitude (see Tab. 1.3).

In 1934 Bruno Rossi reported an observation of near-simultaneous discharges of two Geiger-Müller counters widely separated in a horizontal plane during a test of equipment he was using in a measurement of the east-west effect [Ros34]. Three years later Pierre Auger and Roland Maze, unaware of Rossi's earlier report, detected the same phenomenon and investigated it in more detail [Aug38].

Their experiments in Alps revealed that the cosmic radiation events were coincident in time on very large scale (at more than 200 m distance), meaning that they were associated with a single event. It can happened when a very high energetic particle from a space strikes into the Earth's atmosphere and interacts with nuclei of atmospheric gases. Subsequent collisions of born particles produce a cascade and a fraction of those produced particles hits the ground. From electromagnetic cascade theory Auger and his colleagues estimated an energy of the incoming particle creating large air showers to be at least 10^{15} electronvolts (eV), i.e. about one million particles of energy 10^8 eV (critical energy in the air) and a remaining factor of ten counts for energy losses from traversing the atmosphere [Aug39].

A wide variety of experimental investigations demonstrated that the primary cosmic rays striking Earth's atmosphere are mostly positively charged particles. There were also some indirect confirmations, such as an explanation of night aurorae phenomena, which can be observed in the polar zone [Sto30]. The secondary radiation observed at ground level is composed primarily of a "soft component"

of electrons and photons and a "hard component" of highly penetrating particles, muons, discovered by Carl D. Anderson and his student Seth H. Neddermeyer in 1936 [And36].

After these studies a common consensus about nature of cosmic rays has emerged. It was clear that cosmic rays are relativistic charged atomic nuclei moving through space which strike the Earth's atmosphere each generating cascades of secondary particles known as extensive air shower (EAS). The particles in the air showers proved to be a very interesting for particle physicists, since the cascades contained short-lived particles not easily found in the laboratory. The investigation of cosmic rays led also to discovery of the antimatter. First antiparticle positron, postulated by Paul Dirac in 1928, was discovered in 1932 by Carl David Anderson by passing cosmic rays through a cloud chamber and a lead plate surrounded by a magnet [And32].

Discoveries in cosmic ray field stimulated widespread interest among physicists, led to the genesis of two major fields of research: high-energy elementary-particle physics and cosmic-ray astrophysics. Physics of cosmic rays provided explanations for phenomena observed by the radioastronomy, notably the understanding of synchrotron radiation emitted in astronomical objects. Hess and Anderson shared the Nobel prize in physics in 1936 for the discovery of cosmic radiation and for the discovery of the positron, respectively.

1.3 Extensive Air Showers

High energy cosmic ray particles interact with nuclei in the atmosphere and subsequent collisions initialize cascades of secondary particles. The cascade is called extensive air shower (EAS). The first interaction typically occurs at the altitude between 10 and 30 km depending on an energy and a type of the primary particle. The total energy of the primary cosmic ray particle is distributed to rapidly growing number of secondaries and the cascading process continues until the energy of fragments becomes insufficient for further production of secondaries.

The secondaries of EAS can be separated into two main components: soft (electromagnetic) and hard (muons and hadrons). The most of the secondaries come from the electromagnetic part of EAS which is constituted from photons, electrons and positrons. There are also hadronic interactions (if primary particle was a hadron), which produce shortlived mesons (mainly pions) of which many decay into muons, electrons and photons. In addition, there are particles not contributing much to the total energy balance, i.e. UV photons (fluorescence and Čerenkov) and radio emission, or those which are not detected and are called invisible component (e.g. neutrinos and high energetic muons).

Electromagnetic particles, as the most abundant part of EAS, carry the largest fraction of the total energy (see Fig. 1.4). The electromagnetic shower develops fast, mainly by bremsstrahlung interactions and pair production. Ionization losses start to dominate over the production of new particles below the critical energy E_{crit} (equals to 84 MeV in the air) and the shower is absorbed by the atmosphere. Thus, the electromagnetic shower shows a maximum number of particles at some

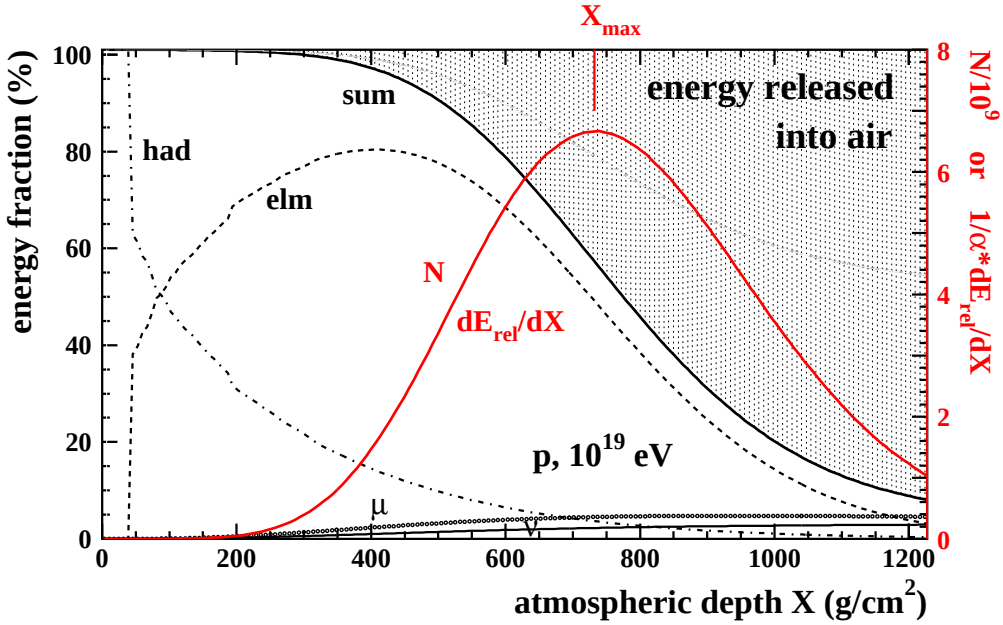

Figure 1.4: Energy fraction (left y-axis) and number of particles (right y-axis) of extensive air shower initiated by proton with energy 10^{19} eV as a function of atmospheric depth. From [Ris04].

stage of shower development. The location of this point given in a slant depth of the atmosphere is called the shower maximum X_{max}.

Muon as a highly penetrating particle hardly interacts and slowly loses its energy mainly due to the ionization. High energy muons can even penetrate kilometers of rock and reach deep underground detectors. Overall fluctuations of the muon number as a function of the slant depth are small and almost constant. The ratio of muonic and electromagnetic components at the ground depends on the type of primary particle (nuclei).

Hadronic particles stay close to the shower axis, which is same as the direction of velocity vector of the primary cosmic ray particle. After a few hadronic interactions, most of the hadronic energy is transferred into the electromagnetic and muonic shower parts. Since the hadronic shower core is long lived and therefore propagates deep into the atmosphere, it serves as a source of new electromagnetic particles and muons.

1.4 Cosmic Ray Energy Spectrum

The energy spectrum of cosmic rays extends from 1 GeV to energies above 10^{20} eV (see Fig. 1.5). Below 10^{14} eV the flux of particles is sufficiently high that individual nuclei can be studied by satellite or balloon experiments. It was found that the majority of particles are nuclei of common elements and around 1 GeV their abundances is similar to ordinary material in the Solar system. An exception is the abundance of light elements such as Li, Be and B which are over-abundant in cosmic

rays because of the fragmentation of heavier nuclei with inter-stellar hydrogen.

Techniques used to study the particles above 10^{14} eV result from discoveries made by Auger and his colleagues. When a high energy particle enters the atmosphere it initiates a cascade which is large enough and sufficiently penetrating to reach ground level. With detectors placed on the ground it is possible to measure basic characteristics of extensive air showers and subsequently to derive arrival direction and energy of primary particles.

The cosmic ray energy spectrum is nearly featureless lacking any lines or dips which would characterise an electromagnetic spectrum covering so many decades. It is often described in terms of a power-law which fits the data over many decades for various cosmic ray nuclei.

At lower energies (below 10^9 eV) an attenuation relative to the power-law observed at high energies is present. The energy and the shape of the cut-off vary with the phase of the solar cycle, the fluxes decrease during periods of high solar activity. It is an artefact of a diffusion of cosmic rays pointing towards the Earth from the interstellar space through the outflowing solar wind. This phenomenon is known as solar modulation (see Fig. 1.6).

The cosmic rays originating outside the Solar system show a smooth flux spectrum and are almost entirely made up from protons and fully ionized nuclei. The observations of the cosmic rays themselves (mainly satellite- and balloon-borne experiments), and of the nonthermal radioemission from our Galaxy as well as from all other well observed galaxies suggest that cosmic rays (except for spallation products) have an universal spectrum with a constant slope (see also Section 2.3).

Only at higher energies the overall cosmic ray flux spectrum shows two distinct features: a steepening of the slope around 3×10^{15} eV and a flattening at an energy above 10^{18} eV. These features were named *knee* and *ankle* in an analogy with the shape of a human leg. The basic slope of the spectrum curve is probably associated with the effectivity of an acceleration mechanism in the variable magnetic field, but both changes of spectral index are still puzzling and could say something about sources and the propagation of CR.

1.5 Detection Techniques

The steeply falling cosmic ray spectrum yields very low fluxes for the highest energy particles. Large detection areas and long measuring times are therefore needed for the observations. Basic characteristics of cosmic rays (such as energy, arrival direction and type of primary particle) are estimated indirectly from observed extensive air showers.

In the energy regime of our interest ($E > 10^{17}$ eV) two methods of EAS detection have been developed: a measurement of a density of shower particles at the ground and an observation of fluorescence light emitted by the atmosphere as the shower passes through it. Both techniques can also be combined together (hybrid measurements). Possible third and presently tested radio detection of EAS uses arrays of dipole antennae tracing synchrotron radiation emitted by electrons and positrons deflected in geomagnetic field.

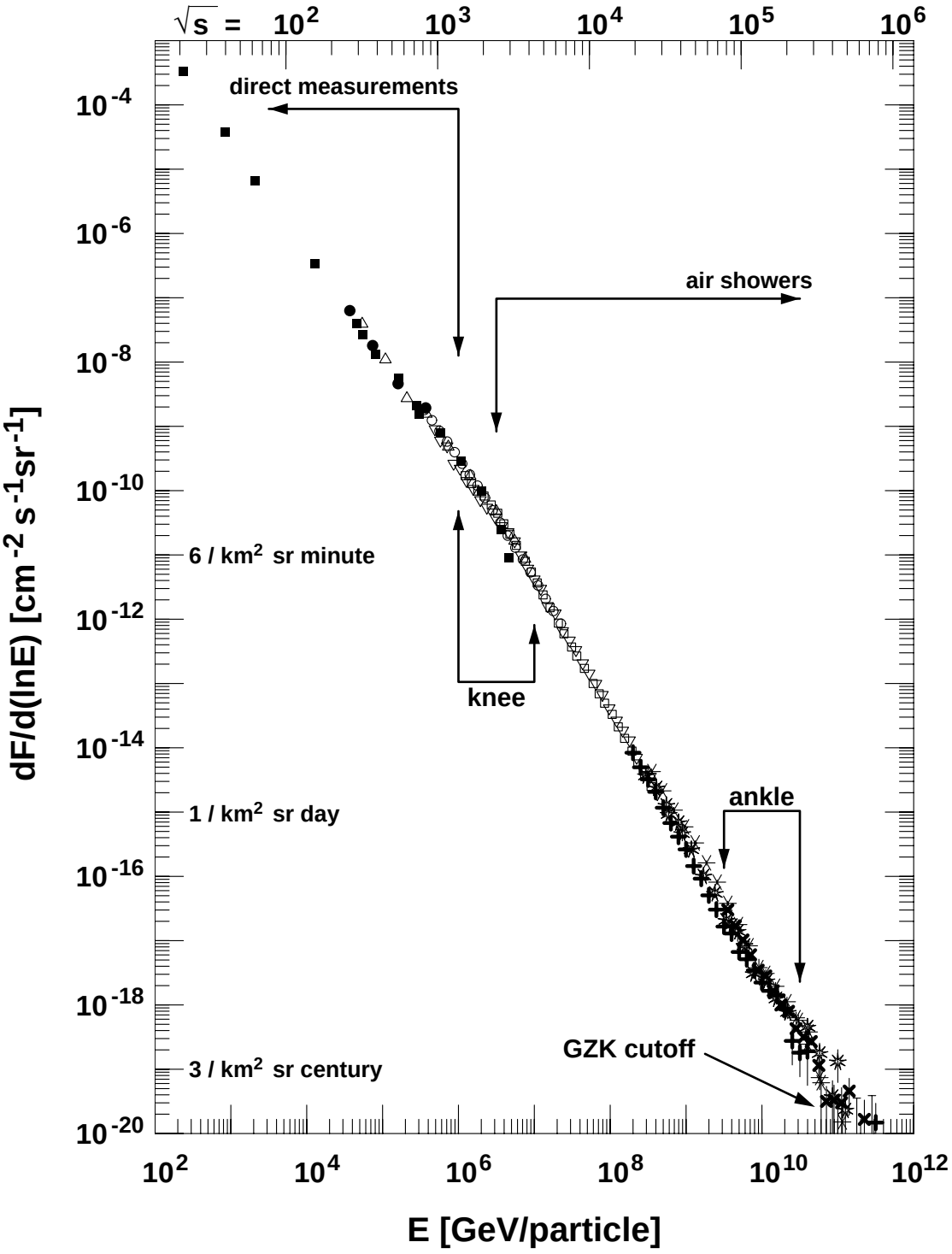

Figure 1.5: Spectrum of cosmic rays compiled from the observations. Different symbols refer to different experiments and they can be find in [Cro97].

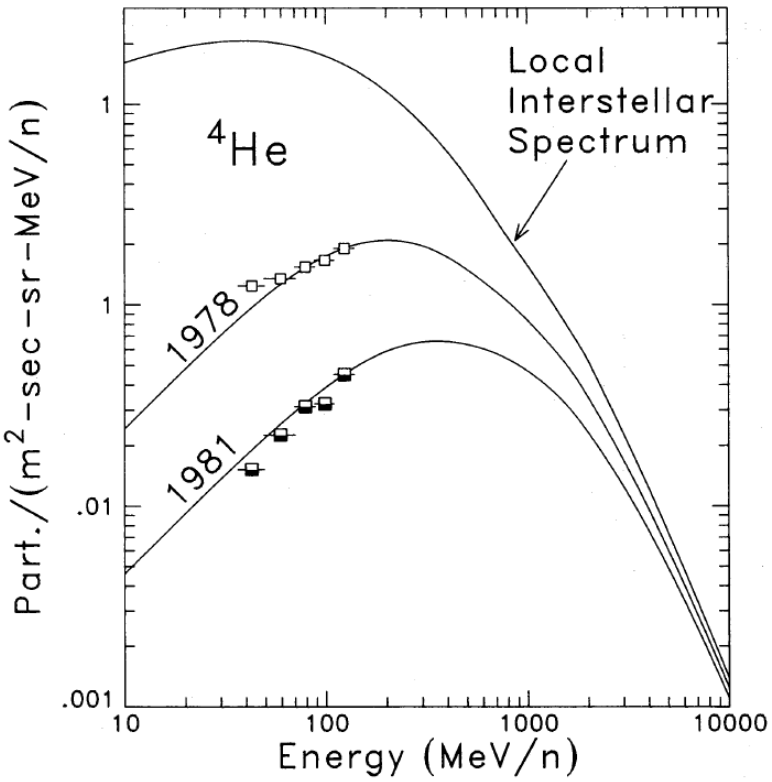

Figure 1.6: Calculated local interstellar ^{4}He spectrum and measured spectra in 1978 and 1981 (period of minimum and maximum solar activity). From [Kro86].

Detectors designed for measurement of cosmic rays go back to the coincidence counter developed by Kolhörster and Bothe in 1929. The first large array of EAS detectors Volcano Ranch had been operated since 1958 by a group from Massachusetts Institute of Technology under the leadership of John Linsley and Livio Scarsi near Albuquerque in New Mexico.

An array of sparse ground detectors samples the shower front and registers information about shower's arrival time and signal intensity. The detectors are typically either scintillator slabs or tanks filled with water, which have different sensitivity to particle components of the shower. Scintillators are primarily sensitive to electrons and photons, but appropriate shielding can allow one to separate out the muon and hadron component as well as differentiate the electrons from the photons. Water tanks, which detect shower particles by the Čerenkov radiation they emit while passing through the detector, are much more sensitive to muons than to electromagnetic particles. Figure 1.7 shows example of modelled particle density on the ground

The momentum of the primary particle is so much greater than any transverse momentum generated in the shower that the shower axis points in the same direction as the velocity vector of the primary particle. The shower direction is inferred from the relative timing of the various detector elements as the shower front proceeds across them. The accuracy of geometrical reconstruction depends on a number of stricken detectors, a zenith angle of shower axis and an accuracy of a time signal.

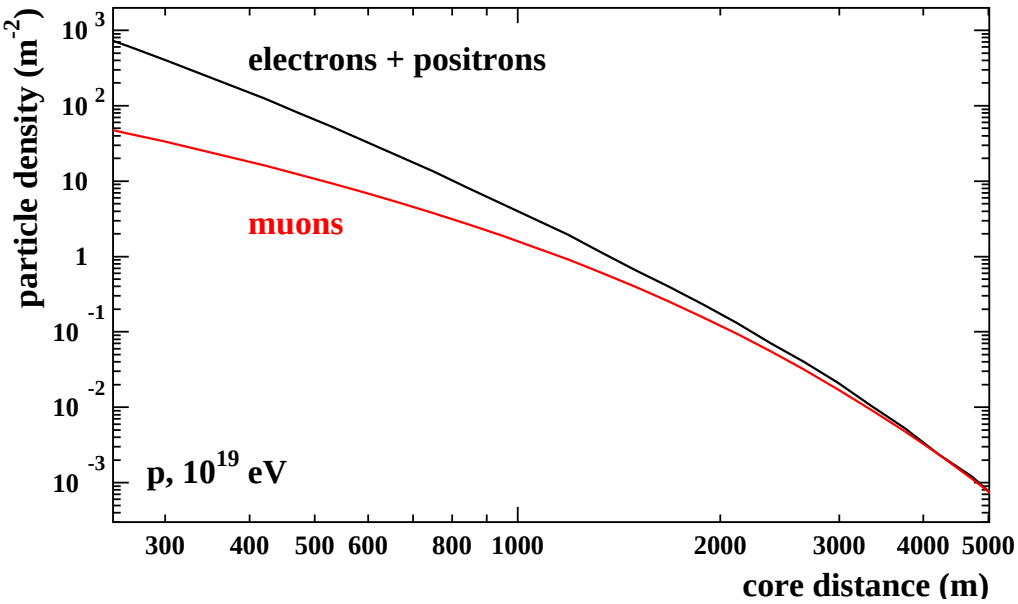

Figure 1.7: Particle density on the ground initiated by 10^{19} eV proton shower. From [Ris04].

The energy of the shower must be inferred indirectly from the size and shape of the shower footprint. The energy of the primary particle goes into the shower and most of the shower energy is deposited in the atmosphere. The shower energy is usually determined by particle density at a given distance from the core (usually around 1 km depending on the array geometry), because it is roughly proportional to particle density and the shower-to-shower density fluctuations are reduced at this distance. However, one must take into account the attenuation of the shower at different zenith angles. Both the normalization and the attenuation correction contribute to systematic uncertainties and are dependent on shower development modeling. One can gain more information by having separate ground stations which are sensitive to electrons or to muons or to photons, but the model dependence is hard to avoid.

Other detection technique collects the fluorescence light generated as the shower particles excite atmospheric nitrogen. The amount of light produced in this way is directly proportional to the energy of primary particle. Prompt emission of fluorescence light lies in UV part of spectra, see Fig. 1.8. The energy reconstruction is affected by an uncertainty in absolute fluorescence yield and its dependence on atmospheric conditions (such as pressure, humidity and temperature).

The type of the primary particle must be inferred from the way EAS develops, which makes it hard to determine the particle type on a shower-by-shower basis even for the best measurements of EAS development. The parameters depending on the type of a primary particle for a given energy can be found in both detection techniques. The longitudinal development of the shower is observed by fluorescence telescopes and crucial parameter - the depth in the atmosphere at which the shower reached its maximum size (X_{max}) - can be directly seen.

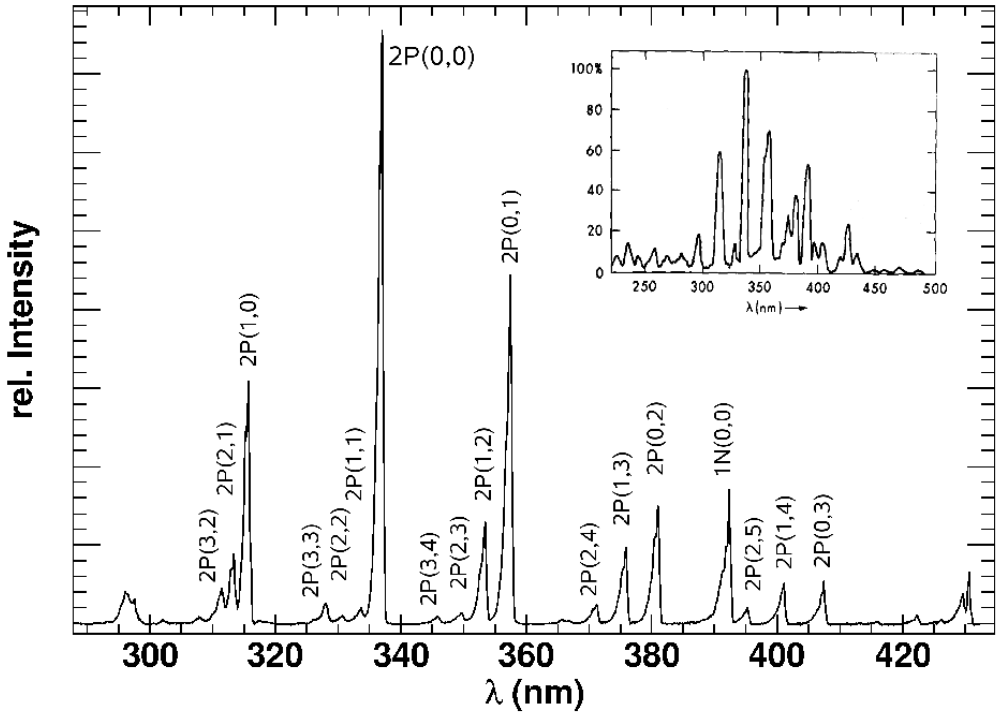

Figure 1.8: Fluorescence spectrum of air recorded by AIRFLY experiment. The gas was excited by 3 MeV electrons at a pressure 800 hPa. The spectrum reported by Bunner in 1967 is shown in the right upper corner. Taken from [Obe07].

The direction of the shower measured by fluorescence telescopes can be determined from the relative timing of light signals on pixels of a camera. More precise determination of the shower geometry is available from stereo observations, when two telescopes at different positions see the same shower and the geometry is determined by the intersection of the two shower-detector planes. Any measurement from just one ground detector also improves geometrical reconstruction.

Observation of longitudinal shower development, slightly model-dependent energy reconstruction (a fraction of an invisible component must be modelled), and large aperture are the advantages of fluorescence techniques. Unfortunately its observation is possible only during nights with good weather conditions and without the presence of the moonlight. In addition, one must control the transparency of the atmosphere by choosing an appropriate (desert) site and by regular measurements of atmospheric conditions. Surface detectors can run continuously, they are almost insensitive to weather conditions and an aperture is proportional to an area which they cover. However, they observe only lateral distribution of secondary particles on the ground and their energy calibration is strongly model-dependent. A combination of both detection techniques is the best choice.

1.6 Cosmic Rays of Ultra-High Energy

In this work we will define ultra-high energy cosmic rays (UHECRs) as primary cosmic ray particles with energy above 10^{18} eV. Their flux at the Earth is very low and they occur at a rate only about 1 per km^2 per year which rapidly decreases with the energy. The discovery of particles with an energy above 10^{19} eV and afterwards above 10^{20} eV, see Fig. 1.9, in 1960s ([Lin61] and [Lin63]) have returned the attention of astronomers and particle physicists back to the study of cosmic rays. It was realized that such an energy cannot be achieved in any man-made accelerator and moreover arrival directions of UHECRs should point to their sources in a case of proton primaries, because of small deflections in magnetic fields.

The first experiment capable to detect UHECRs was Volcano Ranch in New Mexico. It consisted of 19 plastic scintillators, each of 3.3 m^2 detecting surface area, viewed by 5-inch photomultiplier. With 884 m spacing of the stations the array covered an area of 8 km^2 [Lin61]. Also the first successful detection of fluorescence light took place here in 1972.

Another extensive cosmic ray detector SUGAR (Sydney University Giant Air shower Recorder) was operated in Australia between years 1968 and 1979 (see [Win86]). The 54 km^2 array was built from 54 pairs of liquid scintillation detectors (6 m^2 viewed by a single photomultiplier tube) separated by 50 m on a mile (1600 m) square grid. This was the only experiment observing the southern sky until a construction of the Pierre Auger Observatory. But its data suffered from problems with afterpulsing in photomultipliers and the achieved precision contrasts poorly with other experiments. Thus, one should be cautious about taking the energies ascribed to events from SUGAR.

The use of an array of Čerenkov water tanks as the surface detector was pioneered by Haverah Park group from 1968 to 1987 [Law91]. The array was formed by several

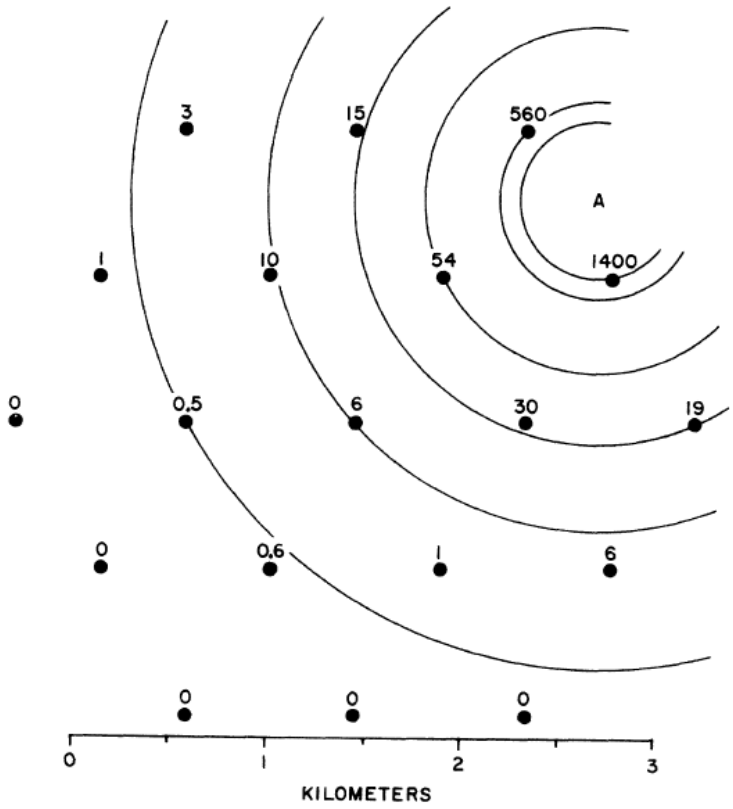

Figure 1.9: Distribution of detected signals (particles/m^2) and estimated core location "A" of 10^{20} eV shower registered at Volcano Ranch in February 1962.

subarrays in an irregular grid, complemented in the last years by 8 scintillators used for cross-calibration with other experiments. Water Čerenkov detectors (2.29 m^2) housed in wooden huts were distributed over an area of 12 km^2. The Čerenkov light was collected by a single 5-inch diameter photomultiplier. During its lifetime many thousands of extensive air showers were recorded including four exceptional ones with the energy above 10^{20} eV.

Scintillator array started in Yakutsk in 1970 is still operational (see for example [Glu95]), although it was rearranged in 1990s. It combines a smaller and larger station separations to increase the energy range of the whole detector. In addition to the scintillators for detecting charged particles, there is an array of Čerenkov detectors, consisting of large photocathode photomultiplier tubes collecting EAS light directly.

The last and the largest scintillator array was operational in 1990 through 2004 near Akeno in Japan. The AGASA (Akeno Giant Air Shower Array) was an array of 111 scintillators with an area of 2.2 m^2, on a roughly square grid with a spacing of about 1 km. It covered a total area of 100 km^2. Another 27 muon detectors were later added. AGASA collected one of the longest list of UHECRs which does not indicate any rapid decrease of their flux at the highest energies.

The first successful measurement of UHECRs due to an observation of fluorescence light from developing EAS was executed by the Fly's Eye experiment in Utah.

The new method provides a tool for tracking the passage of a shower through atmosphere. The first set of telescopes was built in 1981 and consisted of 67 mirror segments 1.5 m in a diameter with total of 880 photomultipliers (5.5° field of view each) covering the whole sky. Second part was built 5 years later 3.4 km apart looking towards the first group of telescopes. The only UHECR event detected by this experiment happened to be the largest ever observed, energy equals to 3.2×10^{20} eV was assigned to it [Bir95].

The next generation of the detector, High Resolution Flys Eye (HiRes), started operation in May 1997 at the site of Fly's Eye experiment on the Five Mill Hill. It also consists of two parts deployed on two desert hills separated by 12.6 km. These detectors were arranged to view nearly 360 degrees in azimuth from an elevation angle of 3 to 17 degrees. A second ring of telescopes located on Camels Back Ridge extends elevation coverage of the second HiRes station to 30 degrees (it began observation in late 1999). Each telescope featured a spherical segmented 3.75 m^2 mirror that focused light onto a camera of 256 photomultiplier tubes. Each photomultiplier viewed approximately 1° cone of the sky. The HiRes monocular data set represents a cumulative exposure of 3000 km^2 sr yr at 5×10^{19} eV. The operation was stopped in April 2006.

Although both detection techniques worked successfully, their results did not fit very well. A shape of the cosmic rays flux measured by AGASA continued beyond $10^{19.4}$ eV unchanged, while the HiRes flux exhibited a significant cut-off (see Fig. 1.10). Both, the disagreement of their results together with large uncertainties and low statistics of observed cosmic rays, were calling for a new generation detector with larger collecting area and an improved detection technique. Most of these conditions were satisfied by Pierre Auger Observatory.

There is another detector Telescope Array being currently constructed in the desert in Millard County in Utah. It will observe EAS at three fluorescence sites and a separate ground array consisting of 576 scintillation detectors each of which contains two layers of a 1.2 cm thick plastic scintillator plate of 3 m^2. They will be deployed in a grid of 1.2 km spacing covering the ground area of 760 km^2. Up to now no result was presented from this experiment.

The All-sky Survey High Resolution Air-shower Detector (ASHRA) located on the island of Hawaii will have among others large target mass for neutrinos and large effective aperture for UHECR. Several observational stations composed of 12 wide-angle high-precision telescopes are planned. They will completely cover all-sky view and will allow simultaneous observation of air fluorescence and Čerenkov lights with 1 arcmin resolution.

A proposal for observations from satellite orbits was also presented. Telescope EUSO will observe Earth's atmosphere from the International Space Station and detect air shower's fluorescence light. Very large detection area could be achieved from orbit, but greater requirement on effective filtering of background light is necessary and the calculation of the effective exposure is difficult.

More information about the experiments can be find in [Nag00] and references therein. Pierre Auger Observatory will be described in the following chapters. Basic information about geography and number of detected highest energy cosmic rays

are shown in Tab. 1.1. Exposures (i.e. area of a detector times field of view in steradians per year) of individual experiments are compared in Fig. 1.11. For a surface detector the exposure is calculated easily from an area covered by the array of detectors. The calculation of the exposure for fluorescence detectors depends on atmosphere's quality and also the knowledge about particle composition and spectral index are required.

Positions of measured cosmic rays with energy above 57 EeV (no energy corrections were applied) are shown in Fig. 1.12. Angular resolution differs between experiments and also the uncertainty in the energy reconstruction must be taken into account in any study (see e.g. [Nag00]).

1.7 Propagation of Ultra-High Energy Cosmic Rays

The power-law fall of cosmic ray spectra with almost constant slope apparently refers to the same acceleration mechanism over many decades of energy. Any deviation from a constant slope could indicate changes in cosmic ray source mechanisms or in a propagation of cosmic rays through interstellar space.

Because of unavoidable problems with an interpretation of cosmic ray data there is no clear explanation for both outstanding features in cosmic rays spectra: knee and ankle. The knee lies at energy where it is expected that galactic sources start to lose their acceleration efficiency. At the same region cosmic rays start to escape from the Galactic magnetic field. The region of ankle seems to indicate an overlaping of Galactic cosmic rays (majority of them are heavy nuclei here) by an extragalactic ones. However, there is an alternative hypothesis trying to explain this feature as a by-product of interactions of the most energetic cosmic rays.

The origin of particles above 10^{20} eV is a puzzle for any known astrophysical mechanisms for many years. Maybe decays of mysterious superheavy dark matter particles or a violation of basic physical laws would explain the existence of them. There is a chance that ultrahigh energy protons, slightly deflected in magnetic fields, point back to sites of origin and their arrival directions map distribution of their sources. In addition distances to sources are limited to only a few tens of megaparsecs (Mpc) from the Earth as will be explained further.

As was shown in 1966, shortly after discovery of Cosmic Microwave Background (CMB) [Pen65], the Universe is not transparent for ultra-high energy cosmic rays. American physicist Kenneth Ingvard Greisen [Gre66] and independently Russians Georgiy Timofeyevich Zatsepin and Vadim Alexeevich Kuzmin [Zat66] calculated a cutoff in the spectrum of protons at energy 6×10^{19} eV caused by photopion production on the microwave background. This has become known as the Greisen-Zatsepin-Kuzmin (GZK) cutoff.

Interactions between cosmic ray proton of extragalactic origin and background photons take place till the center-of-mass energy of colliding particles decreases below the threshold for pion production. Dominant background photons are those in cosmic microwave background radiation (CMB). CMB has a thermal blackbody

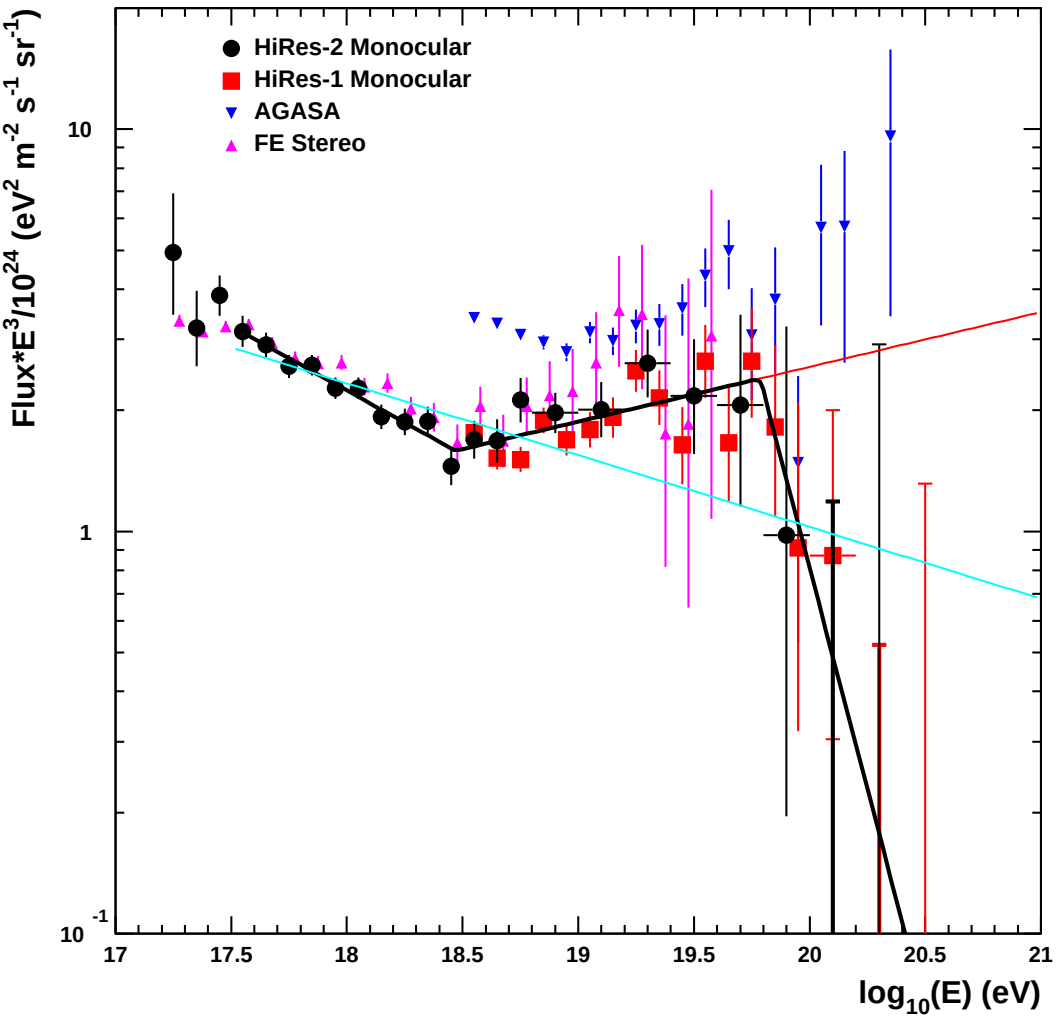

Figure 1.10: Comparison of energy spectra measured by AGASA, Fly's Eye and HiRes. Vertical lines show statistical uncertainties. From [Abb05].

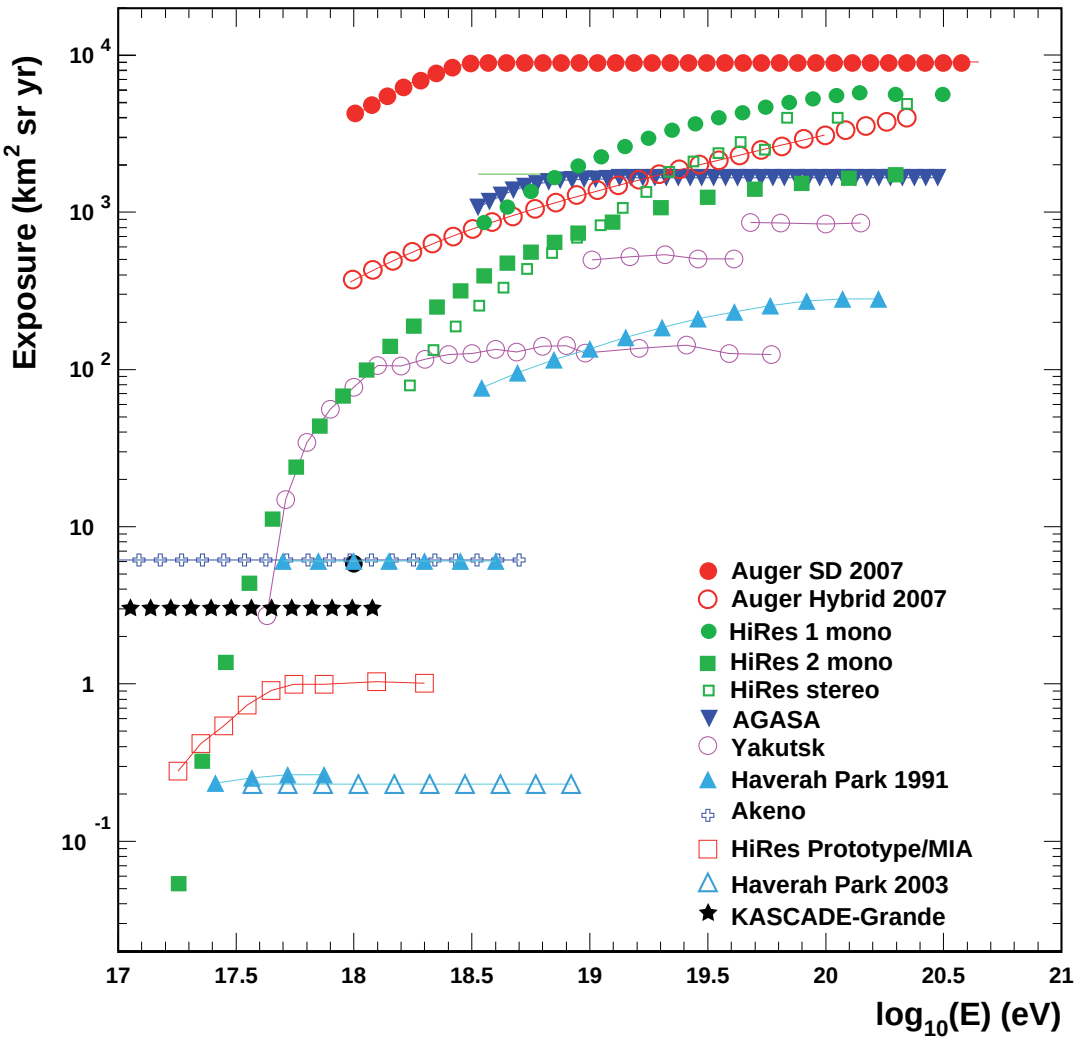

Figure 1.11: Yearly accumulated exposure of cosmic ray experiments for energies above 10^{17} eV [Kam08].

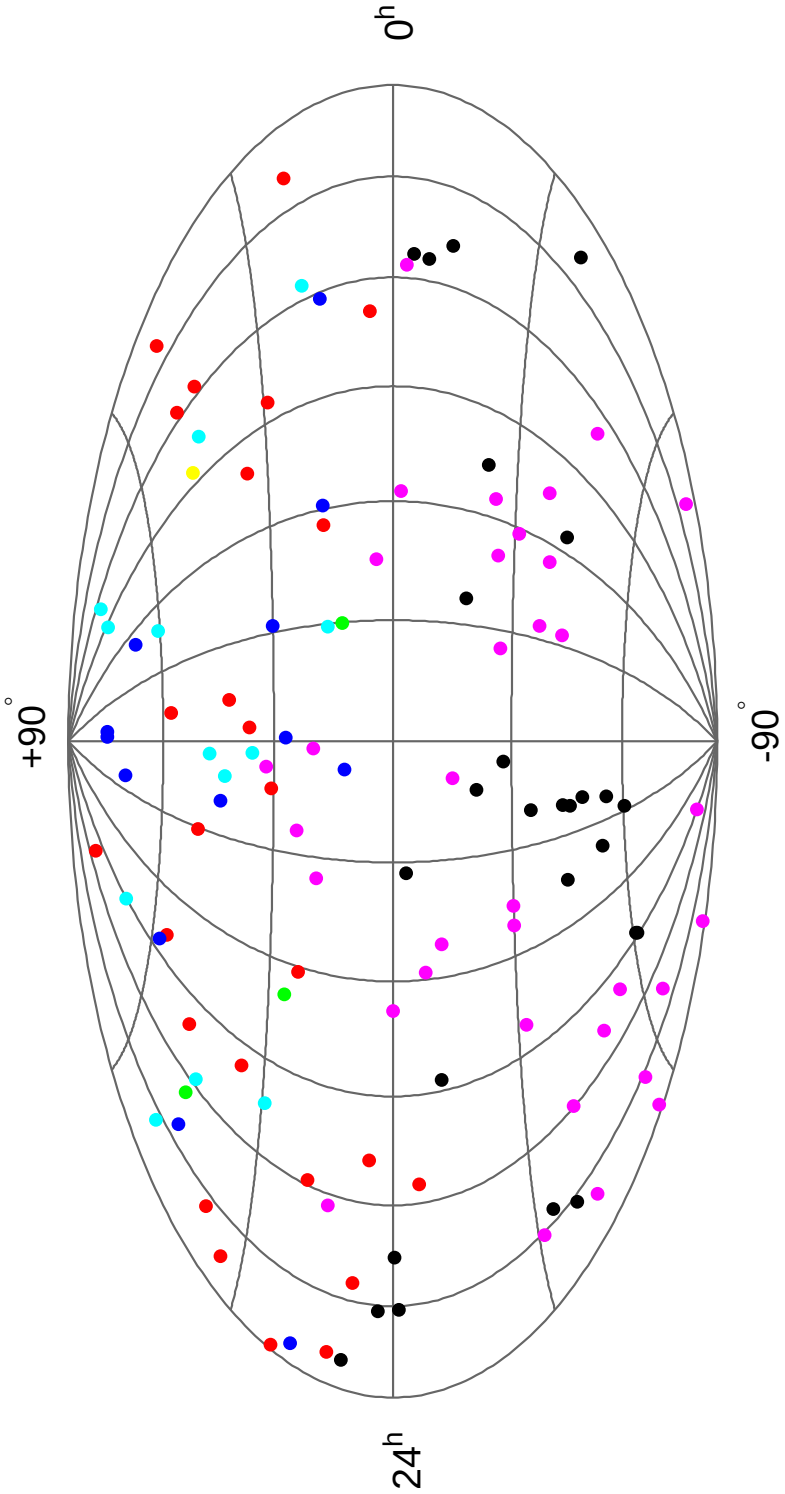

Figure 1.12: Positions of cosmic rays with energy above 57 EeV in equatorial coordinates measured by AGASA(26 red), AUGER (27 black), Haverah Park (13 blue), Sugar (35 magenta), Volcano Ranch (3 green) and Yakutsk (13 azure blue). Fly's Eye collaboration published only the position of the most energetic event (yellow point). No catalogue of cosmic rays from HiRes was presented.

Table 1.1: Sites of UHECR detectors operated in 20th century and approximate number of measured cosmic rays above given energies.

Experiment	Operation	Latitude	Longitude	Altitude [m]	Depth [g/cm^2]	Area [km^2]	Detection	# Events > 10 (> 50) EeV
Volcano Ranch	1959-63	35.1° N	106.8° W	1770	834	8	SC	44 (5)
SUGAR	1968-79	30.5° S	149.6° E	250	1015	60	SC	423 (47)
Haverah Park	1968-87	54.0° N	1.6° W	200	1016	12	WČ	106 (10)
Yakutsk	1974-	61.7° N	129.4° E	105	1020	18/10	SC/AČ	171 (6)
Fly's Eye	1981-93	40.3° N	112.8° W	1597	860		F	?
AGASA	1990-2004	35.8° N	138.5° E	900	920	100	SC	886 (46)
HiRes I	1997-2006	40.2° N	112.8° W	1597	860		F	561 (31)
HiRes II	1999-2006			1553			F	179 (12)
HiRes stereo							F	270 (11)

spectrum at a temperature of 2.73 K and photon density is 410 per cm^3. Just above the threshold for pion production the crossection furthermore significantly increases due to the presence of the $\Delta(1232)$ resonance that has quite large production cross-section. Pion from the decay of the $\Delta(1232)$ resonance carries away about 20% of the proton energy on average. The principal reactions of protons p with background photons γ_{cmb} are following

$$p \ + \ \gamma_{cmb} \ \rightarrow \Delta(1232) \ \rightarrow \ n \ + \ \pi^+ \quad \text{or} \quad p \ + \ \pi^0 \tag{1.1}$$

and

$$p \ + \ \gamma_{cmb} \ \rightarrow \ p \ + \ e^+ \ + \ e^-. \tag{1.2}$$

UHE proton energy losses continue until proton energy falls below the threshold for pion production. The threshold is set by the temperature of the CMB and the mass and the width of the $\Delta(1232)$ resonance. It is about 6×10^{19} eV for protons from extragalactic sources homogenously distributed throughout the universe and cosmic ray energy spectrum going beyond 10^{20} eV. Cosmic ray spectrum will be affected above 10^{20} eV even if there is local overabundance or under-abundance in the distribution of sources. For example an underabundance of local sources will lead to steep fall-off in the spectrum above GZK energy as indicated in Fig. 1.13.

Electron-positron pair production also occurs in interactions between protons and CMB photons. Although the threshold energy for pair production is about 10^{18} eV and the mean free path is about only 1 Mpc, compared to $10^{19.6}$ eV and about 6 Mpc for pion production, energy loss per interaction for pair production is only 0.1% compared to 20% for pion production. Thus significantly less energy is lost by UHE proton by pair production and it takes more than an order of magnitude longer travel distance before there is noticeable effect on proton energy.

There was predicted a dip in cosmic ray spectrum for electron-positron loss mechanism around the energy of 10^{19} eV for pure proton composition [Bere04]. Such dip can be associated with the ankle (see Fig. 1.14). But whether the ankle is really caused by pair production is unclear. The comparison of cosmic ray spectra measured by different experiments used in [Bere04] is disputed and must be examined further. Other scenarios explaining origin of the ankle such as a transition from galactic into extragalactic flux are not excluded.

Photodisintegration [Pug76] and pair production processes [Blu70] are important in the case of heavy nuclei. The main channel is the emission of one nucleon (i.e. production of neutron or proton). The energy-loss rate through double-nucleon emission (such as two neutrons, two protons or proton with neutron) is about one order of magnitude lower than that through single-nucleon emission.

In a case of gamma rays, pair creation through interaction with the cosmic microwave background radiation is most important in a wide energy range above the threshold of 4×10^{14} eV [Wdo72]. The attenuation due to pair creation on diffuse background radio photons becomes dominant over microwave effects above 2×10^{19} eV.

Unstable neutrons with energy above 10^{20} eV (which could be borned as products of interactions of charged ultra high energy particles in sources) have very low probability to survive large extragalactic distances. In a case of other neutral

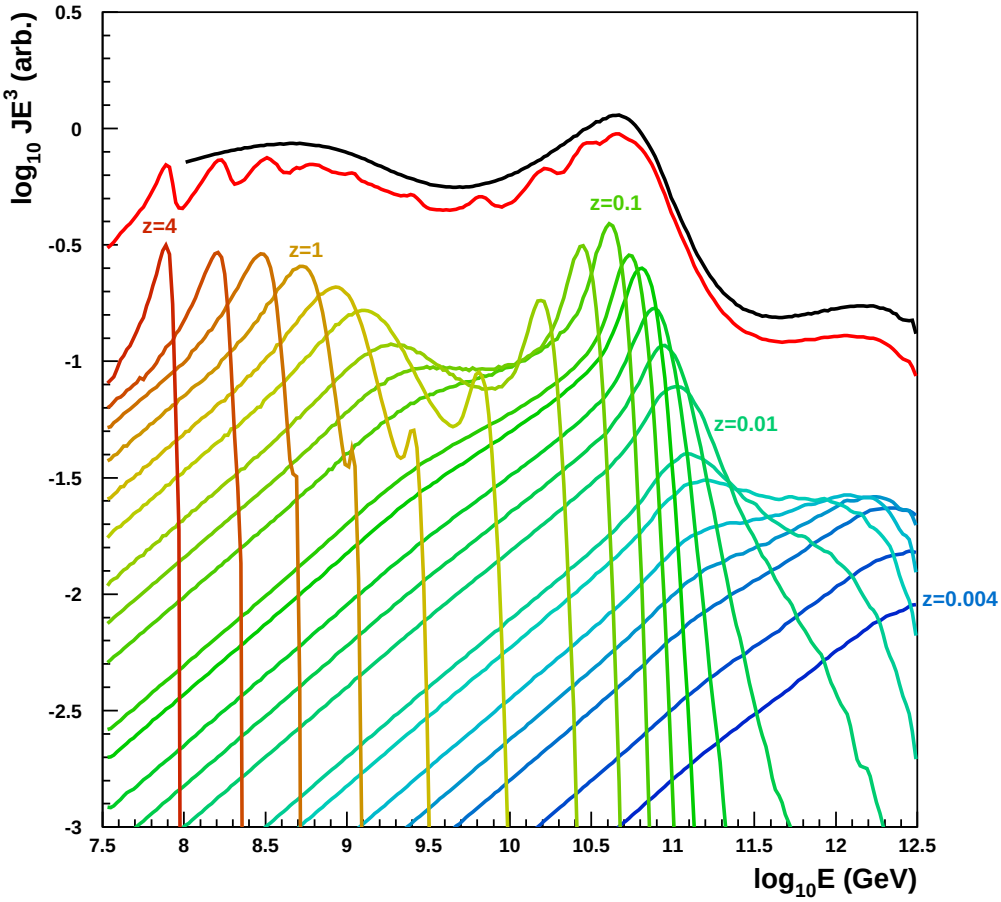

Figure 1.13: Contribution of sources grouped in shells of redshift into cosmic ray spectrum. Model with pure proton composition and source spectral index 2.4 was used [Berg06].

but stable particle, neutrino, the question about its origin must be first answered. Known mechanism of ultra-high neutrino generation are interactions of particles with ambient matter. Therefore we will need even more energetic protons (nuclei) to explain the origin of 10^{20} eV neutrinos. Other possibility are decays of some superheavy particles.

1.8 Attenuation lengths

All the above described interactions are statistical processes and the particle energy as well as their attenuation lengths will fluctuate around their mean values. Figure 1.15 presents attenuation lengths for different types of primary particles propagating through the Universe. (The attenuation length is defined as a distance for which particle loses 1/e of its energy due to interaction.)

An observer is thus naturally asking following question [Cro05]: "If a cosmic

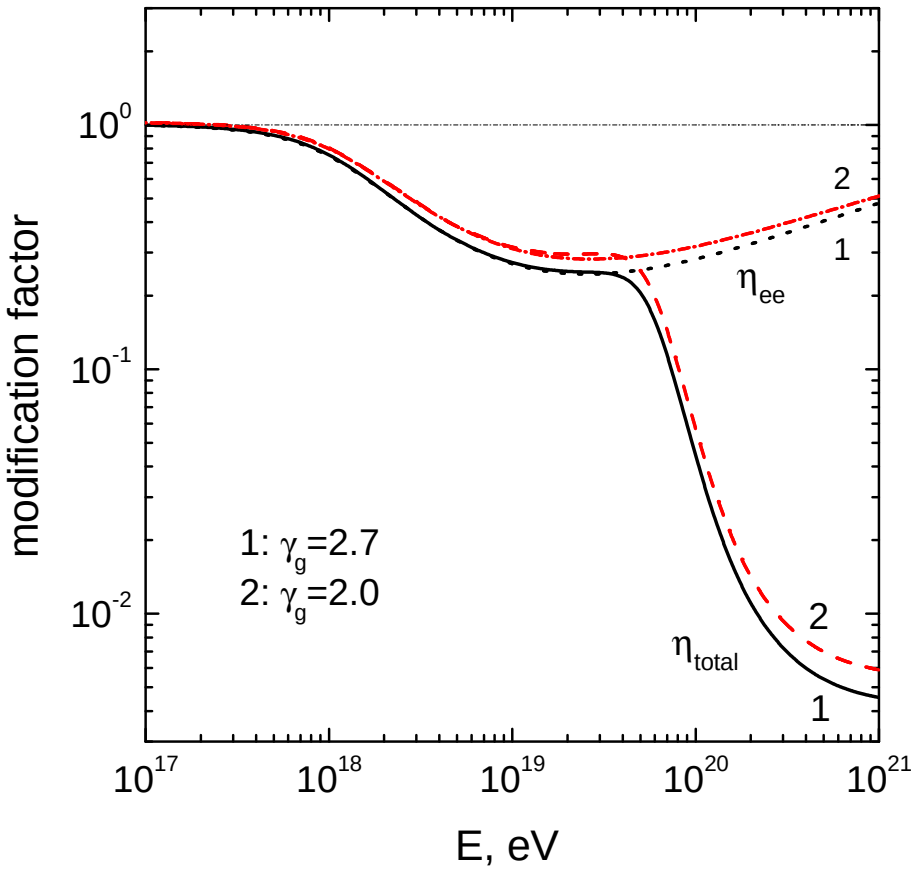

Figure 1.14: Modification of two power-law cosmic ray spectra (source slope γ_g) due to pair production losses η_{ee}. Total energy losses η_{total} are also shown [Alo07].

ray is observed with a particular energy, what is a probability that it came from a distance greater than a specified amount?". To calculate such probability requires an assumption about the spectrum at the source. The answer for one particular source spectrum is shown in Fig. 1.16.

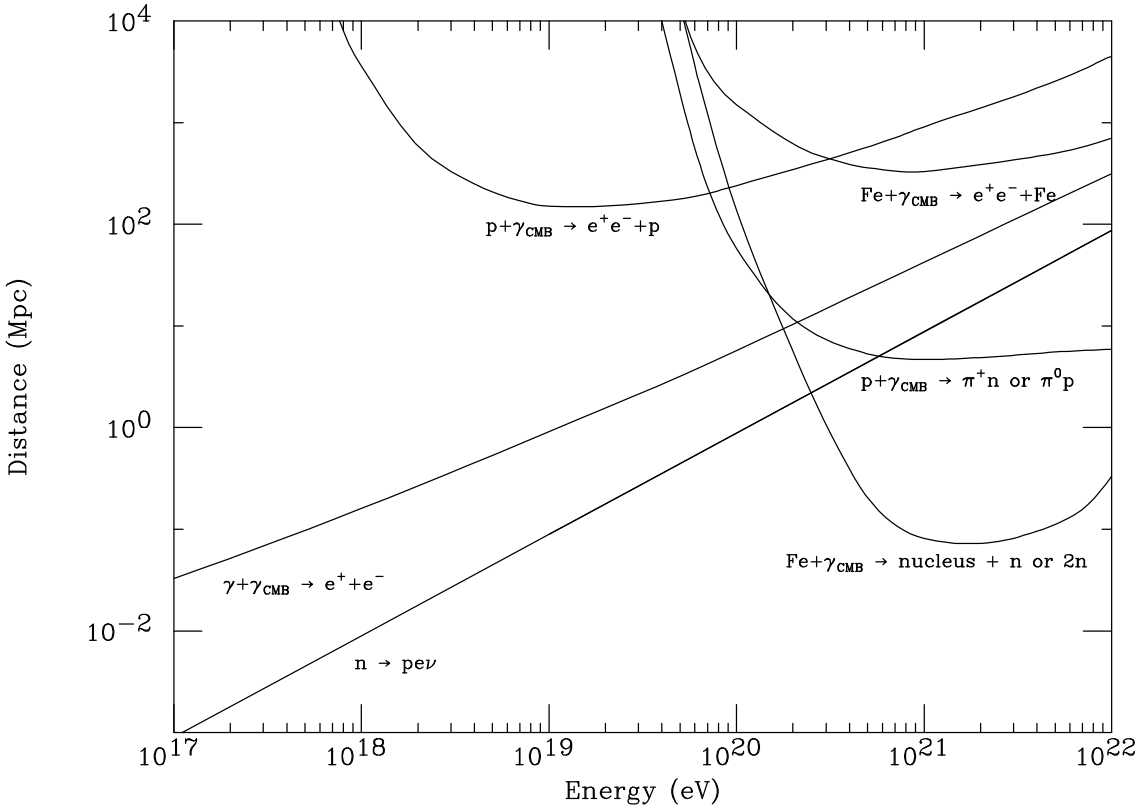

Figure 1.15: Attenuation lengths for interactions between CMB and protons, iron nuclei or high energy photons and mean decay length for neutrons. From [Cro05].

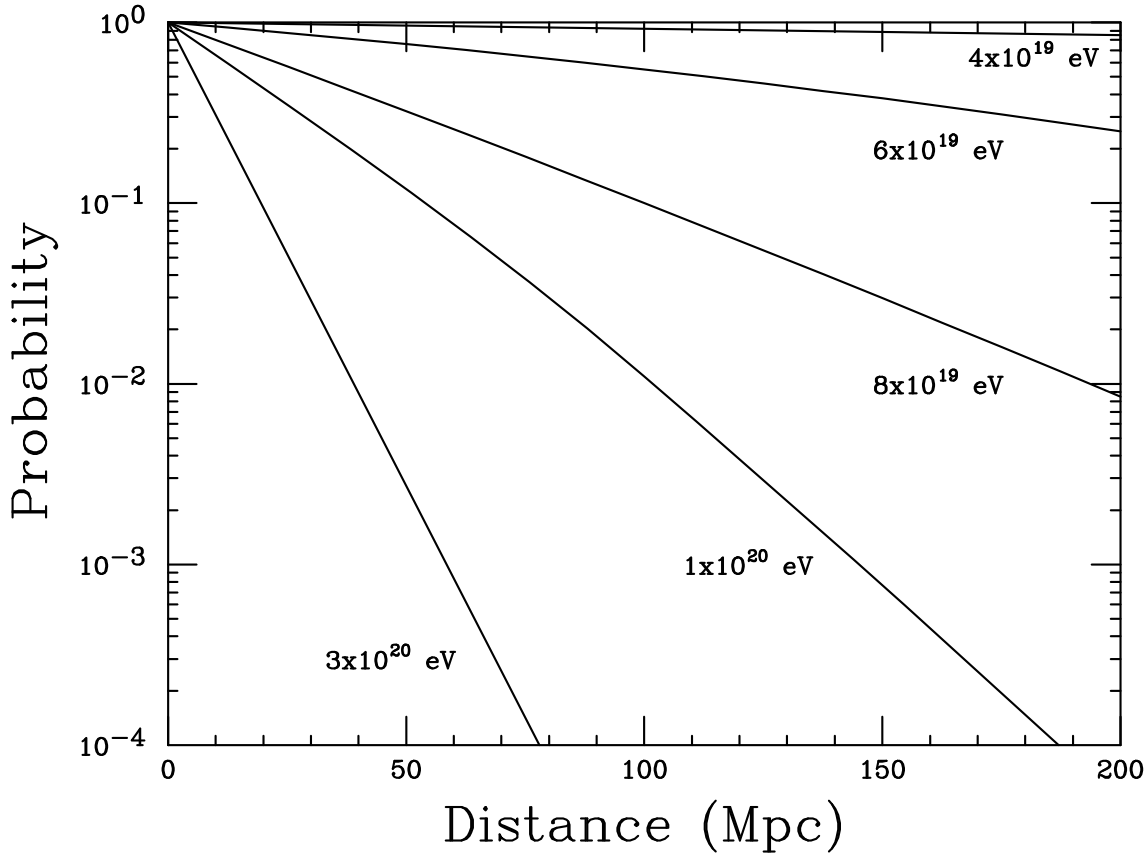

Figure 1.16: Probability that protons with given energy comes from source at distance greater than indicated. Source spectrum proportional to $E^{2.5}$ was assumed. From [Cro05].

Chapter 2

Possible Sources

The origin of ultra-high energy cosmic rays remain unknown after more than four decades of investigation. Two different scenarios have been proposed: an acceleration by strong electromagnetic fields or by long-term statistical shock-wave process in astronomical objects, and decays of superheavy particles which have their rest masses well above 10^{20} eV (so called *top-down* models). Presented scenarios predicted different spectral shape, particle composition and distribution of sources in the Universe.

Since the Larmor radius of particle trajectories at energy in EeV region becomes larger than a thickness of the Galactic disk, it is likely that their sources are extragalactic. An interesting aspect of the extragalactic cosmic rays is the energy loss due to the interactions with cosmic microwave background. GZK mechanism constrains source distance to be less than 100 Mpc and predicts rapid falling of measured spectra (GZK cutoff).

2.1 Original Fermi Theory

The mechanism explaining the acceleration and non-thermal inverse power-law energy distribution of cosmic rays was suggested by Enrico Fermi [Fer49]. It describes how charged particle being reflected by moving interstellar magnetic field in gas cloud either gains or loses energy, depending on whether the cloud is approaching or receding. In a typical environment a probability of a head-on collision is greater than an overtaking collision, so particles will be, on the average, accelerated.

If relativistic particle approaches stable non-relativistic plane boundary of a cloud, the Lorentz transformation of 4-momenta P from the laboratory frame (E, p) into the object (i.e. cloud) rest frame ($E^{'}$, $p^{'}$) can be calculated. The 4-momenta in case of elasting scattering is as following:

$$\begin{pmatrix} E^{'}/c \\ p^{'}_{||} \end{pmatrix} = \begin{pmatrix} \gamma & -\gamma\beta \\ -\gamma\beta & \gamma \end{pmatrix} \begin{pmatrix} E/c \\ p_{||} \end{pmatrix}. \tag{2.1}$$

And from the object rest frame into the laboratory one (see Fig. 2.1):

$$\begin{pmatrix} E/c \\ p_{||} \end{pmatrix} = \begin{pmatrix} \gamma & \gamma\beta \\ \gamma\beta & \gamma \end{pmatrix} \begin{pmatrix} E^{'}/c \\ p^{'}_{||} \end{pmatrix}, \tag{2.2}$$

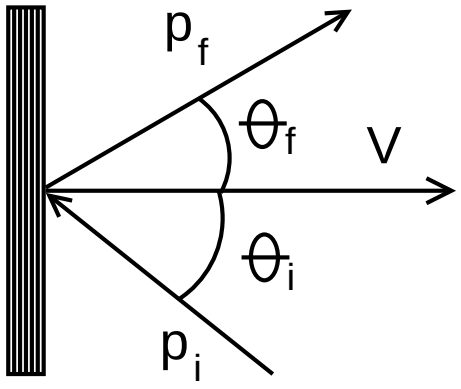

Figure 2.1: Bouncing of a particle off an object moving with velocity V.

where $\gamma = (1-\beta^2)^{-1/2}$, $\beta = V/c$, V is the velocity of the cloud and $p_{||}$ is the component of 3-momentum parallel to β. (The perpendicular component does not change, i.e. $p_t^{'}$=p_t).

Assuming a relativistic particle, i.e. $E_i \simeq pc$, the initial particle energy in the object rest frame will be

$$E_i' = \gamma E_i(1 - \beta\cos\theta_i), \tag{2.3}$$

where primes denote quantities measured in the object rest frame and θ_i is an angle between particle and cloud's momentum. After scattering inside the cloud, the particle emerges with the energy E_f and the momentum p_f at angle θ_f to clouds direction:

$$E_f = \gamma E_f'(1 + \beta\cos\theta_f'). \tag{2.4}$$

Since an elastic scattering on a magnetic field tied to the massive object is assumed there will be no change in energy and total energy of the particle will be conserved in the rest frame of the moving object: $E_i' = E_f'$. For the final particle energy we obtain

$$E_f = \gamma^2 E_i(1 - \beta\cos\theta_i)(1 + \beta\cos\theta_f') \tag{2.5}$$

which can be rewritten as a fractional change in energy

$$\frac{E_f - E_i}{E_i} = \frac{\Delta E}{E_i} = \frac{1 - \beta\cos\theta_i + \beta\cos\theta_f' - \beta^2\cos\theta_i\cos\theta_f'}{1-\beta^2} - 1. \tag{2.6}$$

Inside the cloud the cosmic-ray particle scatters many times so that its direction is randomized and it emerges from the cloud in a random direction. Therefore all θ_f' have equal probability and

$$< \cos\theta_f' >= 0. \tag{2.7}$$

The average value of $\cos\theta_i$ depends on the rate at which cosmic rays collide with the cloud at different angles. The rate of collision is proportional to the relative velocity between the cloud and the particle, thus the probability per unit solid

angle of having a collision at angle θ_i is proportional to $(v - V\cos\theta_i)$. Hence, for ultrarelativistic particles ($v \approx c$) we obtain

$$< \cos\theta_i >= \frac{\int_{-1}^{+1} \cos\theta_i(1 - \beta\cos\theta_i)d(\cos\theta_i)}{\int_{-1}^{+1} \cos\theta_i d(\cos\theta_i)} = -\frac{\beta}{3}. \tag{2.8}$$

Averaging Eq. 2.6 over the angles leads to the formula

$$\frac{\Delta E}{E_i} = \frac{1 + \beta^2/3}{1 - \beta^2} - 1 \approx \frac{4}{3}\beta^2. \tag{2.9}$$

Final change of particle energy $\frac{\Delta E}{E_i} \propto \beta^2$ is positive (energy gain). It is 2nd order in β and because $\beta \ll 1$ (gas clouds in the interstellar matter have random velocities of tens km/s superimposed on their random motion around the Galaxy) the average energy gain is very small. This mechanism, now called second order Fermi acceleration, accelerates particles very slowly, but it was the first mechanism explaining an power-law spectrum of accelerated particles (see Section 2.3).

2.2 First Order Fermi Acceleration

Acceleration mechanism presented by Enrico Fermi has been successfully applied in various objects observed by astronomers. In many of them better conditions for particle acceleration have been described. In the seventies new formula for energy gain in supernova shock waves was found (e.g. [Bel78a], [Bel78b] and [Bla78]). Same mechanism can be applied for shock waves also in other astronomical objects. Geometrical conditions in shock waves lead into gain of energy proportional to β as it is discussed later.

In the shock rest frame an upstream gas flows into the shock front at velocity $v_1 = U$ (where U is shock velocity in laboratory frame) and leaves the shock with downstream velocity v_2 (see Fig. 2.2). From the equation of continuity (conservation of mass across the shock) we have $v_1\varrho_1 = v_2\varrho_2$, where ϱ_i are upstream and downstream densities. For ionized gas the compression rate defined as

$$R = \frac{\varrho_2}{\varrho_1} \tag{2.10}$$

equals to 4. Therefore the downstream velocity $v_2 = v_1/4$.

Fast particles are prevented from streaming away upstream of a shock front by several mechanisms, for example by scattering off Alfvén waves [Bel78a] which they themselves generate or by magnetic mirrors [Jok66] which drift with thermal plasma. A scattering confines particles inside the region around the shock, where multiple passing through the shock is possible.

This acceleration becomes more efficient, because motions are not random: $\cos\theta'_f$ is always positive and $\cos\theta_i$ always negative. So every time the particle crosses the shock it receives an increase of energy and this gain is same in both directions.

For the planar shock the following conditions are defined: $-1 \leq \cos\theta_i \leq 0$ and $0 \leq \cos\theta'_f \leq 1$. Number of particles N entering and leaving moving shock follows

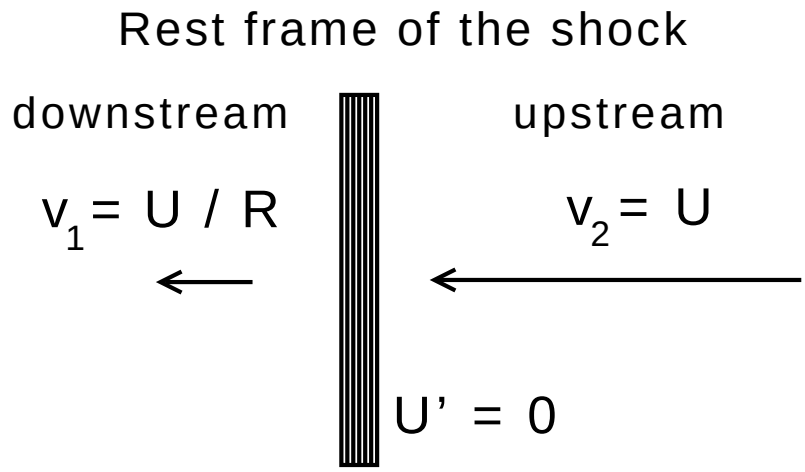

Figure 2.2: Shock front in its rest frame.

$\frac{dN}{d\cos\theta} \propto \cos\theta$. For mean initial cosine of angle between particle and cloud velocity we obtain

$$< \cos\theta_i >= \frac{\int_1^0 \cos^2\theta_i d(\cos\theta_i)}{\int_1^0 \cos\theta_i d(\cos\theta_i)} = -\frac{2}{3}. \tag{2.11}$$

and in same way for the mean value of final angle

$$< \cos\theta'_f >= +\frac{2}{3}. \tag{2.12}$$

The change of particle energy then equals to

$$\frac{\Delta E}{E_i} = \frac{1 + 4\beta/3 + 4\beta^2/9}{1-\beta^2} - 1 \approx \frac{4}{3}\beta \simeq \frac{4}{3}\frac{R-1}{R}\frac{U}{c}, \tag{2.13}$$

where $\beta = V_P/c \ll 1$ refers to the relative velocity of plasma flow.

Equation 2.13 was derived for non-relativistic velocities of the shock. Calculations for relativistic shock waves give analogical result ([Kir87], [Hea88] and others).

2.3 Power-Law Spectrum

The flux of cosmic rays follows a power-law distribution with a constant slope. As it can be shown, such spectrum emerges naturally from the Fermi acceleration mechanism.

The change of energy per one cycle can be characterized as $\Delta E = \eta E_0$, where E_0 is initial particle energy and η is energy gain per 1 cycle. If η is constant, the total energy after k cycles will be

$$E_k = E_0(1+\eta)^k \tag{2.14}$$

To reach the energy E_k there have to be k cycles which can be calculated as

$$k = \log_{1+\eta}\left(\frac{E_k}{E_0}\right) = \frac{\ln(E_k/E_0)}{\ln(1+\eta)}. \tag{2.15}$$

The total probability for the particle to reach the energy E_k after k cycles is

$$P_k = (1-P)^k, \tag{2.16}$$

where P is an escape probability from the acceleration region. Its value will be constant in our calculations.

If there were N_0 particles with the energy E_0, the number of particles with the energy E_k will be (with the substitution from Eq. 2.15)

$$n_k = n(E_k) = N_0 P_k = N_0(1-P)^k = N_0 P\left(\frac{E_k}{E_0}\right)^{\frac{\ln(1-P)}{\ln(1+\eta)}}. \tag{2.17}$$

The power law distribution automatically develops from the Fermi acceleration:

$$\frac{dn(E)}{dE} \propto E^{-(\alpha+1)} \tag{2.18}$$

and the integral spectral index can be defined[1] for small values of P and η as

$$\alpha = -\frac{\ln(1-P)}{\ln(1+\eta)} \simeq \frac{P}{\eta}. \tag{2.19}$$

If we look at a diffusion of a cosmic ray as seen in the rest frame of the shock, there is a net flow of energetic particles in the downstream direction. The net flow rate downstream gives the rate at which cosmic rays are lost downstream

$$r_{loss} = n_{CR}\frac{U}{R}, \tag{2.20}$$

since cosmic rays with number density n_{CR} at the shock are advected downstream with the velocity U/R (from right to left in Fig. 2.2) and we have neglected relativistic transformations of the rates ($U \ll c$).

Cosmic rays travelling with the velocity $v \sim c$ at angle θ to the shock normal (as seen in the laboratory frame) approach the shock from the upstream with the velocity $(U + v\cos\theta)$ as seen in the shock frame. To cross the shock the angle θ must satisfy the condition $\cos\theta > -U/v$. Assuming isotropic flux of cosmic rays from upstream, the rate at which they cross from upstream to downstream is

$$r_{cross} = \frac{n_{CR}}{4\pi}\int_0^{2\pi} d\phi \int_{-U/v}^{1} (U + v\cos\theta)d(\cos\theta) = n_{CR}\frac{v}{4}. \tag{2.21}$$

[1]With a help of Taylor series $\ln(1+x) = \sum_{n=1}^{\infty}\frac{(-1)^{n+1}}{n}x^n$ for $|x| \leq 1$.

The probability of crossing the shock only once and then escaping from the shock (being lost downstream) is the ratio of these two rates:

$$P = \frac{r_{loss}}{r_{cross}} = \frac{4}{R}\frac{U}{v}. \tag{2.22}$$

For 1st order Fermi acceleration ($\eta = \beta$) in typical shock waves ($R \simeq 4$) and for relativistic particles $v \sim c$ we obtain universal integral spectral index $\alpha \simeq 1$ and differential spectrum has therefore slope $\simeq 2$.

Classic mechanism assumes isotropic distribution of particles in the rest frame of the flow, which is not true for relativistic flows. The final spectral index for relativistic collisionless shocks was analytically calculated by [Kes05] and its value is $20/9 = 2.22$.

Fermi acceleration gives constant spectral index for many categories of astrophysical sources in large range of energy. Spectral shape is unavoidably influenced by propagation effects which lead into energy losses in interstellar and intergalactic space. Source spectral index is therefore changed into higher values by a factor of about 0.5. Calculated spectral index is finally in a very good agreement with the observed value (see Fig. 1.5). The explanation of the shape of cosmic ray energy spectra was a great success of the Fermi theory.

2.4 Direct Acceleration

Other mechanism of particle acceleration is an acceleration by some extended electric field arising in rapidly rotating magnetized conductors. Such a mechanism has an advantage of being fast. But its main difficulty is the requirement of sufficiently large voltages.

Most commonly considered sources are unipolar inductors, such as rapidly spinning magnetized neutron stars or black holes. In case of young pulsars, the extremely fast rotation gives rise to an electromagnetic field which could accelerate iron nuclei to energies above 10^{20} eV [MeT97]. Other sources under consideration are spinning black holes with accretion disks in the centers of massive galaxies. They can generate an electromagnetic field sufficient to accelerate even protons up to the highest energies (see e.g. [Has92]).

In all described scenarios the presence of dense plasma and intense radiation is unavoidable which might cause significant energy losses of accelerated particles. It is also unclear, how stable power law energy spectrum could emerge from such scenarios.

2.5 Hillas Diagram

In all acceleration scenarios described in the previous sections there must exist a magnetic field which confines particles within acceleration region. Thus the size L of the given region containing the magnetic field, where particle makes many irregular loops while gaining energy, must be much greater than Larmor radius

of the relativistic particle with the electric charge Ze and the total energy E in the magnetic field B (i.e. the component of magnetic field normal to the particle velocity). It leads to following formula:

$$\left(\frac{r_g}{\mathrm{pc}}\right) \sim 2 \left(\frac{E}{10^{15}\,\mathrm{eV}}\right) \left(\frac{B}{\mu\mathrm{G}}\right)^{-1}. \tag{2.23}$$

If the effect of characteristic velocity βc of scattering centers is included one gets the general condition for maximum energy [Hil84]:

$$E_{max} = \beta\ Z\ e\ B\ L. \tag{2.24}$$

The same condition with typical astronomical units is as following:

$$\left(\frac{B}{\mu\mathrm{G}}\right) \left(\frac{L}{\mathrm{pc}}\right) > 2 \left(\frac{E}{10^{15}\,\mathrm{eV}}\right) \frac{1}{Z\beta}. \tag{2.25}$$

The dimensional argument expressed by Eq. 2.25 is often presented in the form of the Hillas diagram shown in Fig. 2.3. Given types of cosmic particles accelerated up to given energies are represented by diagonal lines (from top to bottom in the figure: protons of 10^{21} eV, protons of 10^{20} eV and iron nuclei of 10^{20} eV). It is clear that only a few sites appear to be able to generate protons with energies above 10^{20} eV. Typically only compact stellar objects with very strong magnetic field or extended structures with much weaker magnetic fields could be potential sources of UHECRs. Young neutron stars belonging to the first group can be also found in our Galaxy. Gamma-ray bursts are typically detected in cosmological distances and are therefore excluded because of the GZK mechanism. Other possible astronomical sources of ultra-high energy particles with rather weak magnetic fields but with large dimension include galaxy clusters, AGN, radio galaxies (Fanaroff-Riley class II) and dead quasars. Some of these objects with the sufficient acceleration potential are presented in Tab. 2.1.

2.6 Multiwavelength Observations

The present day task for UHECRs astrophysics is the location of cosmic ray sources. New precise data are necessary for the critical evaluation of considered acceleration models. Besides the traditional questions about UHECRs (spectrum, anisotropy, type of primary particles, propagation processes), a number of astrophysical issues must be resolved like the understanding of intergalactic magnetic-field structures, the existence of galactic winds, the evidence of cosmic dark matter, etc.

However, it has to be noticed that also electrons are accelerated apart from protons and nuclei. Protons and nuclei can achieve much higher energies than electrons within given magnetic environments (because of smaller synchrotron losses). On the other hand energy losses of relativistic electrons lead to nonthermal photon radiation.

In comparison with the charged particles, which are the primary products of cosmic accelerators, γ-rays have the substantial advantage that they propagate on

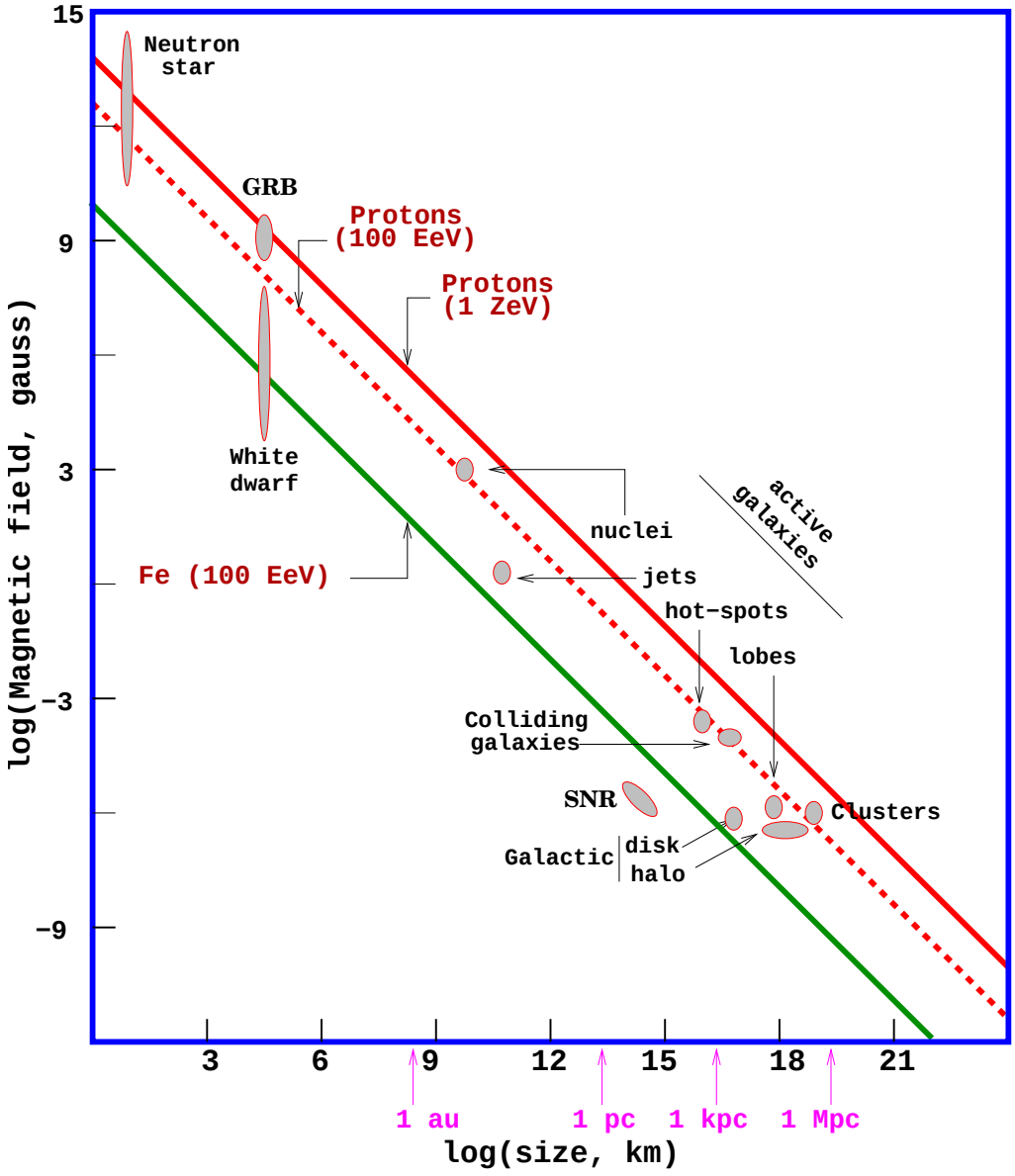

Figure 2.3: Hillas diagram showing size and magnetic field strengths of typical objects where particles can be accelerated. Objects below diagonal lines cannot accelerate protons or iron nuclei above the given energy [Hil84].

Table 2.1: Candidates for UHECR acceleration sites: typical energies achievable for nuclei in question are given (here O stands for all medium atomic number nuclei) with expected factors which could reduce maximal energy E_{max}. From [Ost02].

Acceleration site	Expression for E_{max}/eV	Nuclei	E_{max}	Reducing factors
Relativistic jets				
a) Terminal shock	$r_g < H$	p	$> 10^{20}$	Realistic mag. field structure
b) Side boundary	$r_g < R_j$	p	$> 10^{20}$	Realistic mag. field structure
Supergalactic accretion shocks	$r_g < 1$ Mpc	p	$> 10^{19}$	particle escape
Rotating neutron stars				
a) region of strong mag. field	$10^{20} Z B_{13} R_6^2 / T_{-3}$	Fe	$> 10^{20}$	geometric factors, pairs
b) wind and shock	$4 \times 10^{20} B_{13} \Omega_3^2$	Fe	$> 10^{20}$	injection efficiency
Dead quasars	$4 \times 10^{20} Z B_4 M_9$	p, O, Fe	$> 10^{21}$	details of physical process
GRB shocks	$r_g < \Gamma L$	p, O, Fe	$> 10^{20}$	mag. field structure

straight lines through the Universe and their sources can be located. The charged particles are, on the other hand, deflected by galactic and intergalactic magnetic fields and therefore do not point directly to locations of their sources.

An observation of high energy γ-rays can be an indirect confirmation of particle acceleration in many astronomical objects. High-energy γ-rays can be produced by interactions of accelerated particles with nuclei of ambient medium from decays of neutral pions π^0. Highly energetic electrons may undergo bremsstrahlung in the ambient medium, may suffer synchrotron radiation losses in local magnetic fields, or a significant part of their energy may be transferred to ambient photons in the inverse Compton scattering process. High-energy γ-rays emerge from all such processes.

2.7 Top-Down Models

Difficulties with acceleration scenarios of UHECRs in astronomical objects motivated new proposal of the top-down models, where cosmic rays, instead of being accelerated, are decay products of some superheavy particles. Another support for the top-down models comes from the absence of GZK cutoff.

A mathematical description of the standard model of the weak, electromagnetic and strong interactions suggests an unification of these forces at energies about 2×10^{25} eV, five orders of magnitude above the highest energy observed in cosmic rays. The grand unified theories (GUTs) predict an existence of an X particle with mass m_X around the GUT scale of $\sim 2 \times 10^{25}$ eV. If its lifetime is comparable to or larger than the age of the Universe, it would be dark-matter candidate and its decay could contribute to UHECRs flux today, with an anisotropy pattern that reflects expected dark matter distribution. Such models avoid the GZK cutoff because the cosmic ray flux will be dominated by particles from decays in the halo of our Galaxy.

However, in many GUTs, supermassive particles are expected to have lifetimes not much longer than their inverse masses [Sig01]:

$$\tau \sim 6.6 \times 10^{-41} \left(\frac{10^{25}\,\mathrm{eV}}{m_X} \right) \mathrm{s}, \tag{2.26}$$

and thus they must be produced continuously. This might occur by an emission from topological defects which can be relics of cosmological phase transitions that could have occurred during an inflationary epochs in early Universe when its temperature was close to the GUT scale.

The X particles will typically decay into quarks and leptons. The quarks hadronize, i.e. produce hadronic jets (jet is a shower of particles confined in a narrow cone whose axis lies along a direction of propagation of an original quark) containing mainly pions with a small percentage of baryons (mainly protons). The pions later decay into photons, neutrinos and charged leptons. As we can see a large fraction of high energetic photons and neutrinos is expected from top-down models and only a small fraction of protons (about 10%) and zero fraction of heavier nuclei.

In order to observe the decay products of the X particles as UHECRs today, three basic conditions must be satisfied:

1. The X particles must decay in recent cosmological epoch, or equivalently at non-cosmological distances ($\leq$100 Mpc) from the Earth. Otherwise the decay products of the X particles lose their energy by interacting with the background radiation. A possible exception is the case when neutrinos originating from X particle decay at large cosmological distance $\gg$ 100 Mpc give rise to UHE proton and/or photons within 100 Mpc from the Earth through the decay of Z bosons resonantly produced due to an interaction of UHE neutrino with the thermal relic background (anti)neutrinos (this scenario is known as Z bursts).

2. The X particles must be sufficiently massive, i.e. $m_X \gg 10^{20}$ eV.

3. The number density and the rate of decay of the X particles must be large enough to produce detectable flux of ultra-high energy cosmic rays.

Predictions of top-down models can be confronted with the results of Pierre Auger Observatory and in such a way many of them were recently disproved (see Section 5.2).

Chapter 3

Propagation in Magnetic Fields

It is generally accepted that majority of primary particles with energies above 10^{12} eV are fully ionized nuclei. Therefore an influence of magnetic fields on their propagation must be considered when arrival directions on the Earth are studied. The deflection of arrival direction depends on particle charge and energy. At energies above 50 EeV the typical deflection of protons propagating through galactic and extragalactic magnetic fields is supposed to be only a few degrees and therefore the observed arrival directions could point back to the positions of their sources.

The strength and configuration of magnetic fields can be inferred only due to indirect measurements. The radio observations of many galaxies reveal some common features in configurations of their magnetic fields. Of course the magnetic field in our Galaxy has been closely studied and some models of its configuration and strength have been presented.

As follows from cosmological models, the strength of magnetic fields changes with baryon density (see Fig. 3.1). In such a way upper limits on a strength of extragalactic magnetic fields can be simply estimated.

There are strong evidences from the measurements, that the Galactic magnetic field has also turbulent component. These turbulent magnetic fields have typical sizes of 50 pc and randomly oriented magnetic field vectors. Turbulent magnetic field strength ranges typically from 0.5 $B_{regular}$ to about 2 $B_{regular}$, where $B_{regular}$ is the strength of the regular (large-scale) magnetic field. Because of the unknown distribution of the turbulent magnetic fields in the Galaxy, their influence on the propagation of cosmic rays can be studied only statistically. These turbulences may influence cosmic rays, particularly if primary particles are heavy nuclei.

However, in this work only the study of the influence of the most common models of large-scale Galactic magnetic field on a propagation of cosmic rays will be presented. As will be shown, the Galactic magnetic field plays significant role in the propagation of cosmic rays and its influence must be considered.

3.1 Galactic Magnetic Field

The first evidence of the existence of the Galactic magnetic field was derived from the observation of linear polarization of starlight [Hil49]. Plenty of new measurements

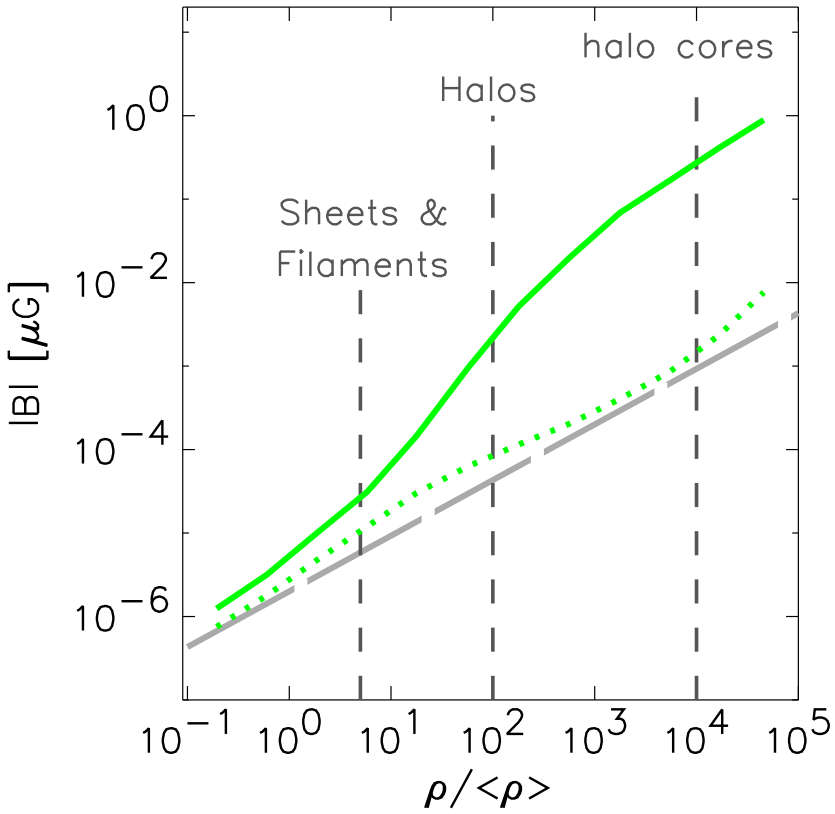

Figure 3.1: Magnetic field strength as function of relative baryon density. Lines show expectations for different types of cosmological large structure formation [Dol05].

were done since then using the Zeeman spectral-line splitting (gaseous clouds, central region of the Galaxy), the optical polarization data (large-scale structures of the magnetic field in the local spiral arm) and the Faraday rotation measurements in the radio continuum emission of pulsars and of the extragalactic sources. The last mentioned method is probably also the most reliable for the large-scale magnetic field structures. The measurements reveal that the Galactic magnetic field has, in the same way as magnetic fields in other galaxies, two components: regular and turbulent.

The global models omit the presence of turbulent fields and describe just the regular component. We adopted the model of magnetic field component in the Galactic plane based on the Faraday-rotation measurements of hundreds of pulsars [Han94]. The model assumes a two-arm logarithmic spiral with constant pitch angle and it shows π-symmetry and is called bisymmetric (BSS) magnetic field model. More exactly, it has also a dipole character (it has field reversals and odd parity with respect to the Galactic plane), so it is called BSS-A model.

Alternative models with another field configurations were also proposed. The another possible configuration is the axisymmetric (ASS) configuration without re-

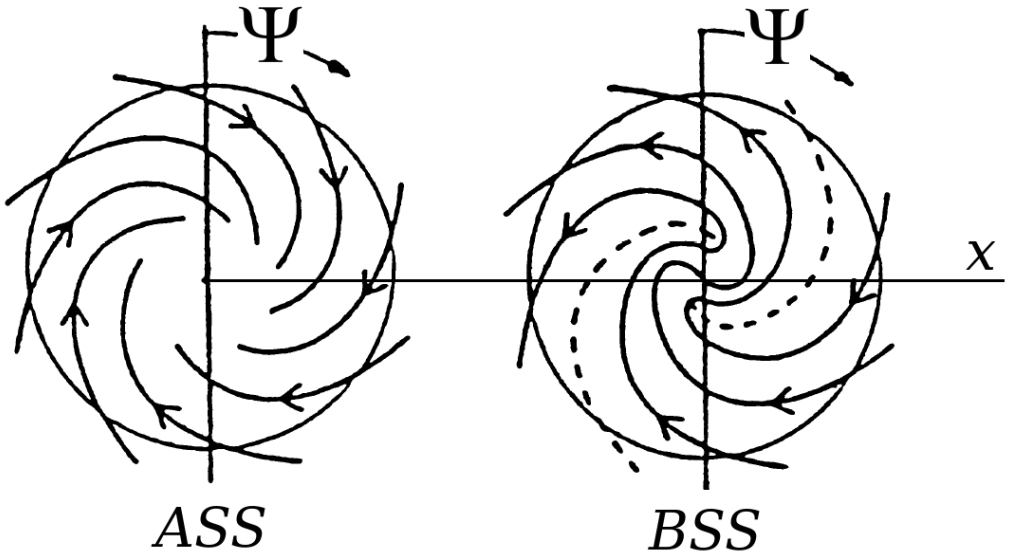

Figure 3.2: Axisymmetric and bisymmetric models.

versals and with even parity (ASS-S) [Sta97]. This configuration could be easier modeled using prefered dynamo model of magnetic field generation [Els92]. The bisymmetric mode can also be obtained from dynamo model, but in such case the use of strong non-axisymmetric perturbations is necessary. The other two possibilities of magnetic field configurations: bisymmetric dipole type (BSS-S) and axisymmetric quadrupole type (ASS-A) are not completely excluded by observations [Bec96].

The dynamo model has one very interesting consequence for the propagation of CRs, namely that except of relatively flat field in the galactic disc it contains also a toroidal field above and under the galactic plane. The existence of such field is indirectly supported by the existence of radio thick disc. The existence of third poloidal (dipole) component of regular large scale magnetic field in our Galaxy is supported by observation of vertical component of 0.2 μG in the Earth's vicinity and intensive filaments near the Galactic center.

In our directional analysis of cosmic-ray arrival directions we use Galactic magnetic field model introduced in [Pro03]. The position of the Earth in cartesian coordinates is $(x = 0, y = R, z = 0)$, where $R = 8.5$ kpc is the Galactocentric distance of the Earth. In the spherical coordinates the position of the Earth is $(r = R, \theta = \frac{\pi}{2}, \phi = \frac{\pi}{2})$ (θ ranges from 0 to π and it goes from the north to the south galactic pole).

The field strength of **spiral model** at a point $(r,\Psi = -(\phi - \frac{\pi}{2}))$ in the Galactic plane in the bisymmetric model is

$$B(r, \phi) = B_0(r) \cos\left(\Psi - \beta \ln \frac{r}{r_0}\right) \tag{3.1}$$

and following form holds for the axisymmetric

$$B(r,\phi) = B_0(r)\left|\cos\left(\Psi - \beta \ln\frac{r}{r_0}\right)\right|. \tag{3.2}$$

The radial B_r and azimuthal B_ϕ components of the field are

$$B_r = B_0(r,\phi)\sin p,\ B_\phi = B_0(r,\phi)\cos p. \tag{3.3}$$

The radial distance is r, Ψ is the position angle, $p = -10^\circ$ denotes the pitch angle, $r_0 = 9$ kpc is the Galactocentric distance of the maximum field strength at galactic longitude $l = 0^\circ$ and for $B_0(r) = 3\frac{R}{r}$. The field above and under the Galactic plane is taken as exponentially decreasing

$$|B(r,\phi,z)| = |B(r,\phi)|\exp(-|z|/z_0), \tag{3.4}$$

with $z_0 = 1$ kpc.

For **toroidal field** we choose the model with simple geometry (circular discs above and under the Galactic plane with Lorentzian profile in z-axis). For cartesian components of toroidal field it holds

$$B_x = -B_T\sin(\phi),\ B_y = B_T\cos(\phi) \tag{3.5}$$

The equations above are valid only in the northern Galactic hemisphere, in the southern hemisphere the field has opposite direction, so B_x and B_y components change their sign there. For the value of B_T we have

$$B_T = B_{max}\frac{1}{1+\left(\frac{z-H}{P}\right)^2} \tag{3.6}$$

for $x^2 + y^2 < R^2$ and otherwise

$$B_T = B_{max}\frac{1}{1+\left(\frac{z-H}{P}\right)^2}\exp\left(1 - \frac{(x^2+y^2)^{1/2}}{R}\right), \tag{3.7}$$

where x, y are positions in the Galactic plane. Meaning and values of used constants follow: the radius of a circle with toroidal field $R = 15$ kpc, height above the Galactic plane $H = 1.5$ kpc, half-width of Lorentzian distribution $P = 0.3$ kpc, and maximal value of toroidal magnetic field $B_{max} = 1$ μG.

Equation for the total **poloidal field** strength in polar coordinates is

$$B = \frac{K}{r^3}(1 + 3\cos^2(\theta))^{1/2} \tag{3.8}$$

and its radial and horizontal components as following

$$B_r = -\frac{2K}{r^3}\cos\theta, B_\theta = \frac{K}{r^3}\sin\theta. \tag{3.9}$$

A cylinder (height 300 pc, diameter 100 pc) with constant strength of magnetic field equals to 2 mG was put into the Galactic center to avoid a problem with too

strong field near $r \sim 0$. In a such way the total field strength was kept in observed bounds. The constant K was selected as follows: $K = 1.23 \times 10^5$ G.pc^3 for outer regions ($r > 5$ kpc) and $K = 200$ G.pc^3 for central region ($r \leq 585$ pc) of the Galaxy. For the intermediate region (0.585 kpc $< r \leq 5$ kpc) we used constant absolute field strength 1μ G. These values correspond to the observed features of Galactic magnetic field: milligauss field restricted only to the central cylinder and the vertical magnetic field equals to 0.2 μG at the distance of the Sun.

For more details see [Pro03] and references therein.

3.2 Deflection of Cosmic Rays

A charged particle moving through magnetic field is affected by the Lorentz force:

$$\vec{F} = q(\vec{E} + \vec{v} \times \vec{B}), \tag{3.10}$$

where q and $\vec{v}$ are the particle charge and velocity (which is almost equal to the velocity of light in vacuum, the relativistic γ factor equals to 10^{10} at energy 10^{19} eV). $\vec{E}$ is the electric field and $\vec{B}$ is the magnetic field, respectively. The Galaxy has no net electric field, so the equation of motion reduces to:

$$\vec{F} = q(\vec{v} \times \vec{B}). \tag{3.11}$$

For cosmic ray studies it can be rewritten into

$$\vec{a} = \frac{q}{m}(\vec{v} \times \vec{B}) = \frac{Zc^2}{E[\mathrm{eV}]}(\vec{v} \times \vec{B}), \tag{3.12}$$

where $\vec{a}$ is an acceleration of the particle with the mass $m = \gamma m_0$, Z is the atomic number and c is the velocity of light in the vacuum.

For motions in complicated magnetic fields, this ordinary differential equation must be solved by numerical methods. The fourth-order Runge-Kutta routine with adaptive step size control was used for an integration of the equation of motion. By this method the Lorentz force equation reduces to six first-order differential equations (two for each spatial dimension):

$$\begin{aligned}
&\vec{K}_1 = \vec{v}_n, && \vec{L}_1 = \vec{v}_n \times \vec{B}_0; \\
&\vec{K}_2 = \vec{v}_n + \vec{L}_1 dt/2, && \vec{L}_2 = \vec{K}_2 \times \vec{B}_0; \\
&\vec{K}_3 = \vec{v}_n + \vec{L}_2 dt/2, && \vec{L}_3 = \vec{K}_3 \times \vec{B}_0; \\
&\vec{K}_4 = \vec{v}_n + \vec{L}_3 dt, && \vec{L}_4 = \vec{K}_4 \times \vec{B}_0; \\
&\vec{x}_{n+1} = \vec{x}_n + (\vec{K}_1 + 2\vec{K}_2 + 2\vec{K}_3 + \vec{K}_4)dt/6, \\
&\vec{v}_{n+1} = \vec{v}_n + (\vec{L}_1 + 2\vec{L}_2 + 2\vec{L}_3 + \vec{L}_4)dt/6
\end{aligned} \tag{3.13}$$

where we define $\vec{B}_0 = \frac{q}{m}\vec{B}$. To be able to model the motion of the particle through any magnetic field, we need to choose the appropriate magnetic field for the Galaxy.

The antiparticle tracking method was used, where an antiparticle (i.e. particle carrying an opposite charge than the observed one) starts its propagation at the

position of the Earth. Components of its initial velocity vector in spherical coordinates are: radial component c (equals almost to the velocity of the light) and galactic coordinates of its arrival direction b and l, galactic latitude and longitude, respectively. Because of the opposite charge and the opposite velocity vector the antiparticle propagates through the given magnetic field on the same trajectory as did the particle, but in the opposite direction. When propagated antiparticle leaves the Galactic magnetic field (here defined as 50 kpc sphere centered at Earth's position), new coordinates can be evaluated. They show the direction from which the particle observed at the Earth entered into the Galaxy.

3.3 Maps with Results

The sky views of angular deflections for one-component and also more complex models of the Galactic magnetic field in galactic coordinates (see Fig. 3.3 to 3.8) show the arrows pointing from the starting position of an antiproton (at the Earth) towards its final direction of the velocity vector outside the Galaxy (at the distance of 50 kpc from the Earth). Antiprotons with energy of 50 EeV were propagated through magnetic fields till their distance from the Earth was larger than 50 kpc.

The angular deflection generally increases with the strength and the complexity of the magnetic field model. Therefore the largest influence on particle propagation can be found for trajectories lying inside the disk of the Galaxy. However, several cases with large angular deflection can be found also for trajectories lying outside the disk. See for example the cases with poloidal (Fig. 3.5) and toroidal (Fig. 3.6) field components and their combination with spiral magnetic field (Fig. 3.7).

We also studied angular deflection of cosmic rays observed by the Pierre Auger Observatory. Together 36 cosmic rays with energy above 57 EeV observed till September 2007 [Abr08] were used in our analysis. Figure 3.9 shows the fraction of these cosmic rays with an angular difference between starting and final direction of velocity vector lower than the value shown on x-axis for given models of the Galactic magnetic field. The particles were propagated from the position of the Earth as antiprotons. The same procedure was applied for particles starting from the positions of AGN with redshifts below 0.018 (i.e. closer than 75 Mpc) taken from [Ver06]. The antiprotons with energy of 70 EeV were pointed from the Earth to AGN directions and traced up to the distance 50 kpc. The fraction of angular deflection lower than given angle are shown in Fig. 3.11. Following figures (3.10 and 3.12) show same results for anti-iron nuclei.

The anisotropy of arrival direction of cosmic rays above 57 EeV observed by the Pierre Auger Observatory (see Section 5.4), verified by statistical test with the catalogue of AGN, immediately lead to suggestion of localization of sources close to the positions of AGN. Such suggestion can be valid if primary cosmic ray particles are rather light nuclei (i.e. nuclei with low charge Z). Angular deflections of different possible primary particles (protons Z=1, helium Z=2, carbon Z=6, and iron nuclei Z=26) propagated through the Galactic magnetic field averaged over the sky are shown in Tab. 3.1. Particles were propagated from 5° distant points in galactic latitude and 10° in galactic longitude. The largest variances are caused

Table 3.1: Angular deflections in degrees averaged over the whole sky for components of the Galactic magnetic field (GMF) and their variances. Values are in degrees.

GMF	H	σ^2_H	He	σ^2_{He}	C	σ^2_C	Fe	σ^2_{Fe}
BSS	2.0	0.3	4.0	1.1	12.6	12.4	55.5	180
ASS	2.9	4.6	5.6	12.6	16.3	68.7	63.0	180
Pol	1.7	1.4	3.4	5.4	10.2	46.4	43.5	180
Tor	1.4	3.3	2.5	6.3	6.1	19.1	19.1	180
BSS+Pol+Tor	3.1	2.9	6.2	9.2	18.3	91.9	75.0	180
ASS+Pol+Tor	2.9	4.2	5.7	12.3	17.7	87.3	80.1	180

by deflections suffered by particles propagated typically close to the Galactic plane (i.e. sky positions with absolute values of galactic latitude $b \leq 10$ degrees).

As can be seen, sources can be identified with the closest AGN in the vicinity of observed cosmic ray event's arrival directions only if the majority of cosmic rays are protons. Already in the case of helium nuclei the angular deflections are higher than 3 degrees and if their large variances are considered, it will be hardly possible to identify a source for each individual cosmic ray event. Current observation of $\langle X_{max} \rangle$ are against pure proton composition of observed UHECRs (see Section 5.3).

Also the angular deflection of antiprotons propagating from the Earth to the position of Centaurus A was studied as a function of particle energy. Fig. 3.13 shows mean values of angular deflections of 81 test particles with root mean squares. The mean value of angular deflection shows distinctive differences for applied models of magnetic field. For two the most complex models of magnetic field the angular deflections are higher than 3 degrees even for the most energetic protons (E=100 EeV).

Extragalactic magnetic fields were not implemented in our model, but they can also play important role in the propagation of UHECRs. There are not many measurements in the intergalactic space, but their strengths can be estimated from the models of cosmological evolution [Das08].

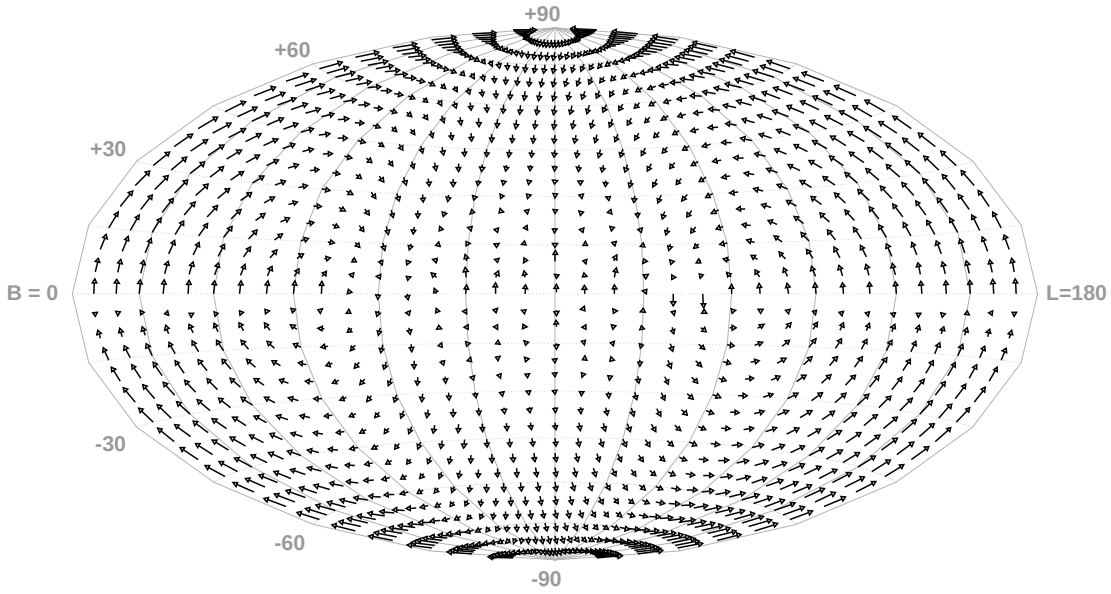

Figure 3.3: Angular deflection of protons with energy of 50 EeV propagated through BSS spiral model of Galactic magnetic field. Arrows show indicate shift of direction of particle velocity vector in galactic coordinates.

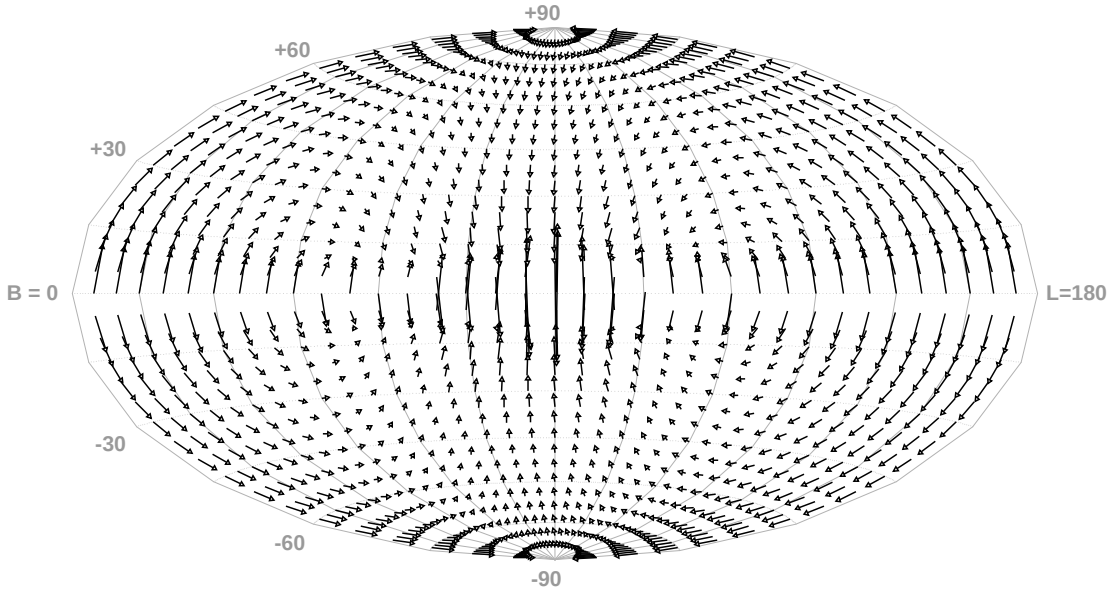

Figure 3.4: Same description as in Fig. 3.3, but for ASS spiral model.

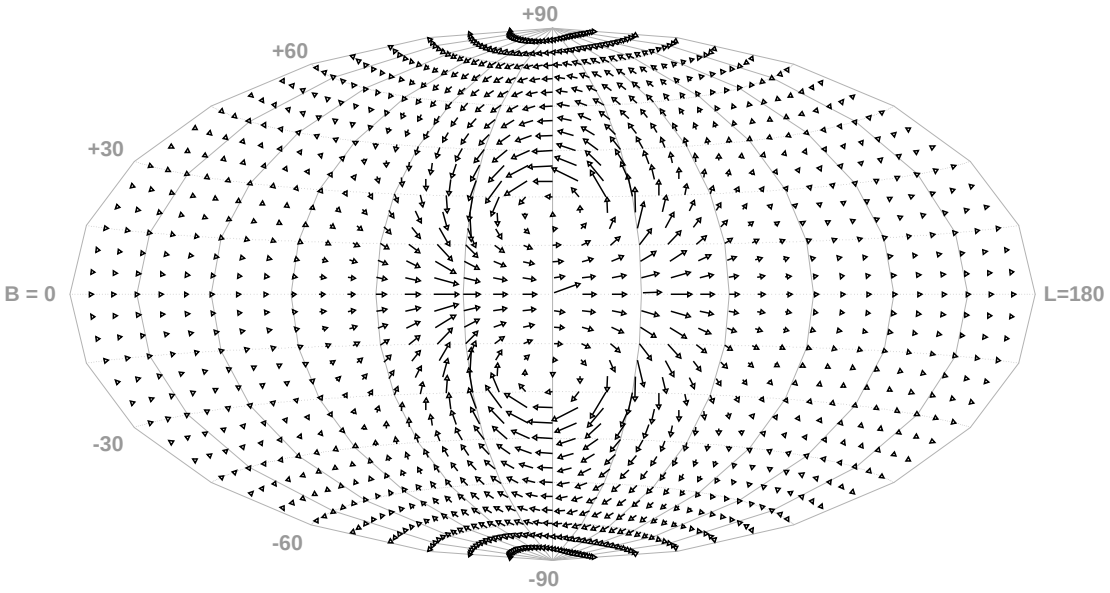

Figure 3.5: Same description as in Fig. 3.3, but for poloidal model.

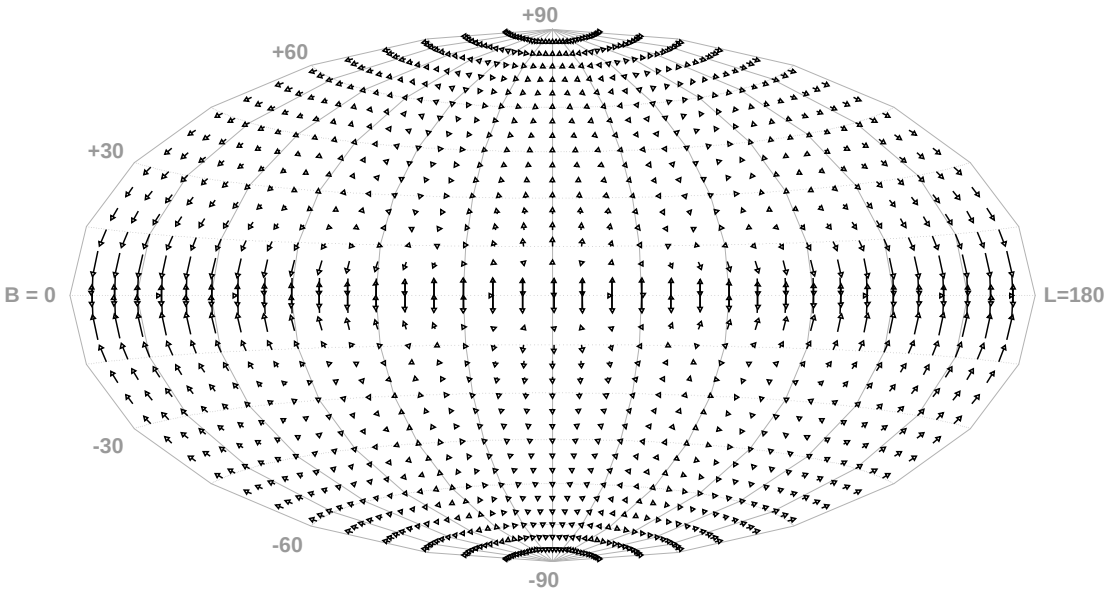

Figure 3.6: Same description as in Fig. 3.3, but for toroidal model.

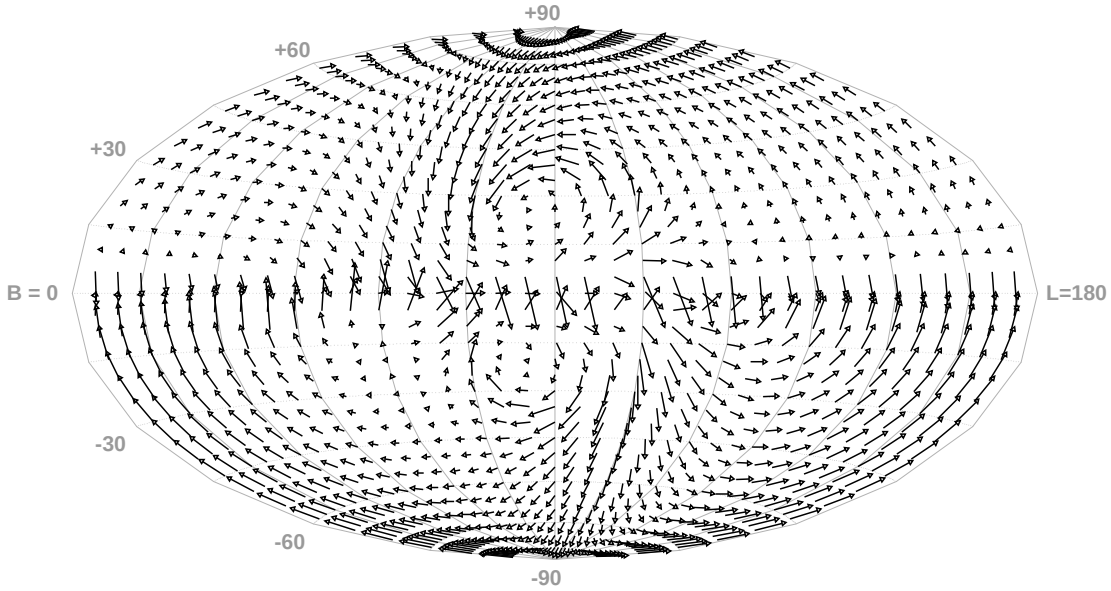

Figure 3.7: Same description as in Fig. 3.3, but for combination of BSS spiral, poloidal and toroidal models.

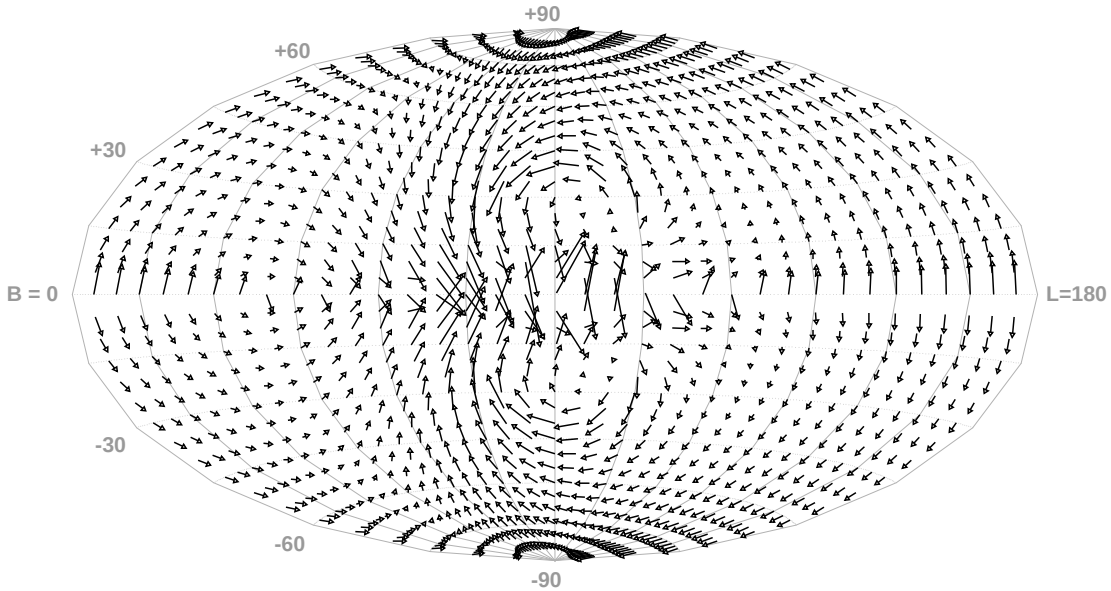

Figure 3.8: Same description as in Fig. 3.3, but for combination of ASS spiral, poloidal and toroidal models.

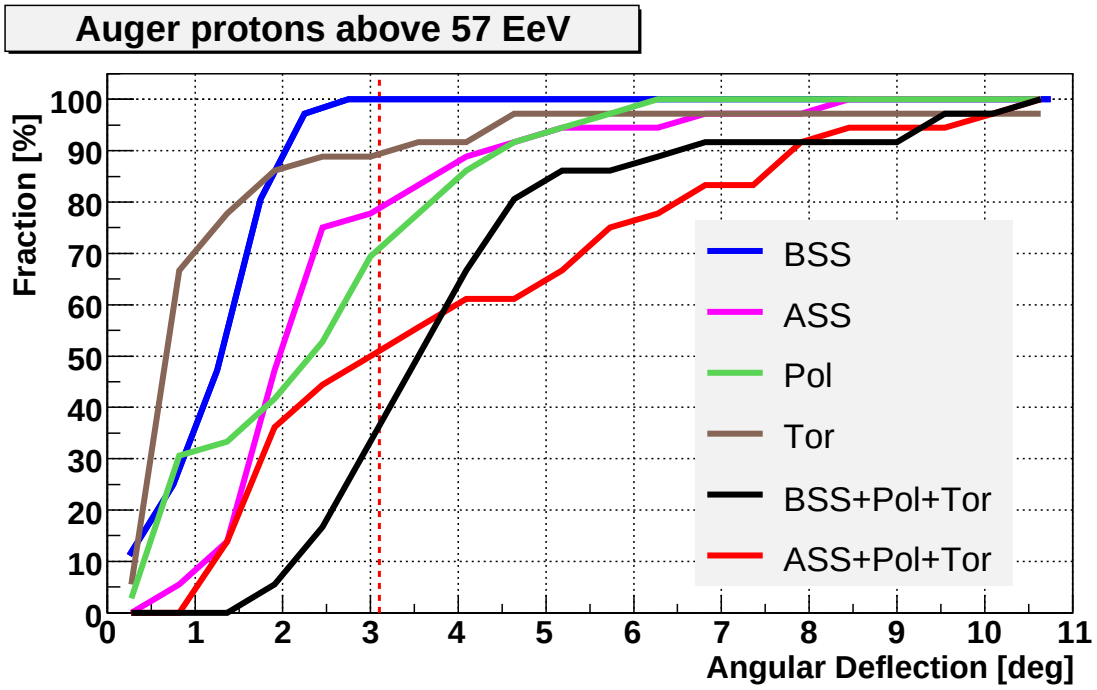

Figure 3.9: Fraction of cosmic rays observed by Pierre Auger Observatory above energy 57 EeV (36 till March 2008) traced as antiprotons from the Earth with deflection angle lower than value on x-axis for given models of Galactic magnetic field.

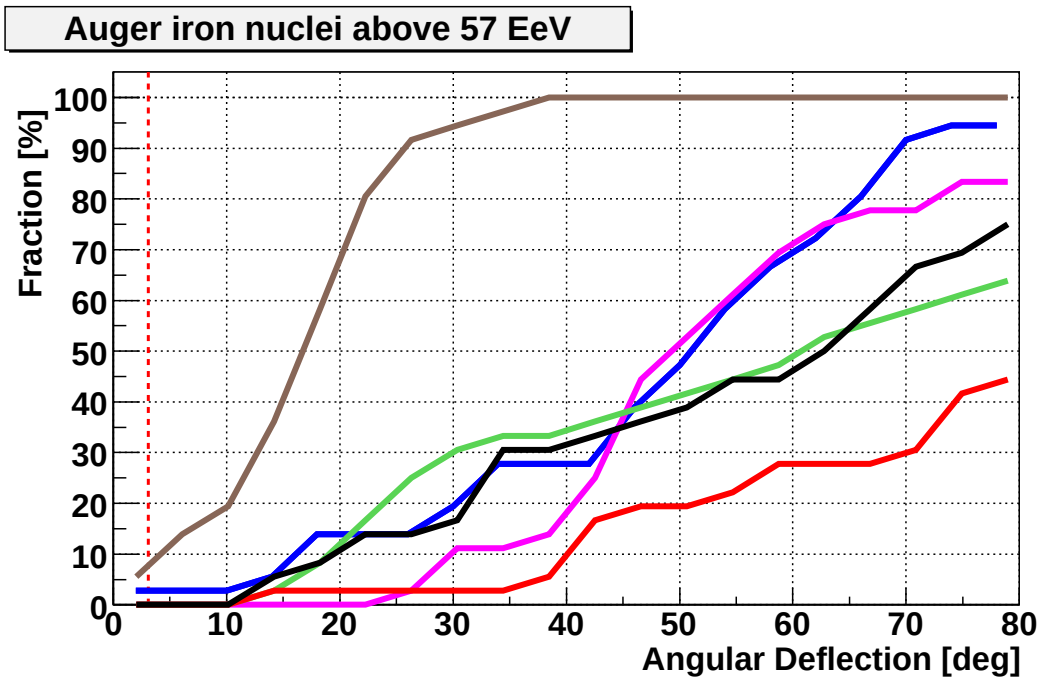

Figure 3.10: Fraction of cosmic rays observed by Pierre Auger Observatory above energy 57 EeV (36 till March 2008) traced as anti-iron nuclei from the Earth with deflection angle lower than value on x-axis for given models of Galactic magnetic field. Meaning of lines is same as in Fig. 3.9.

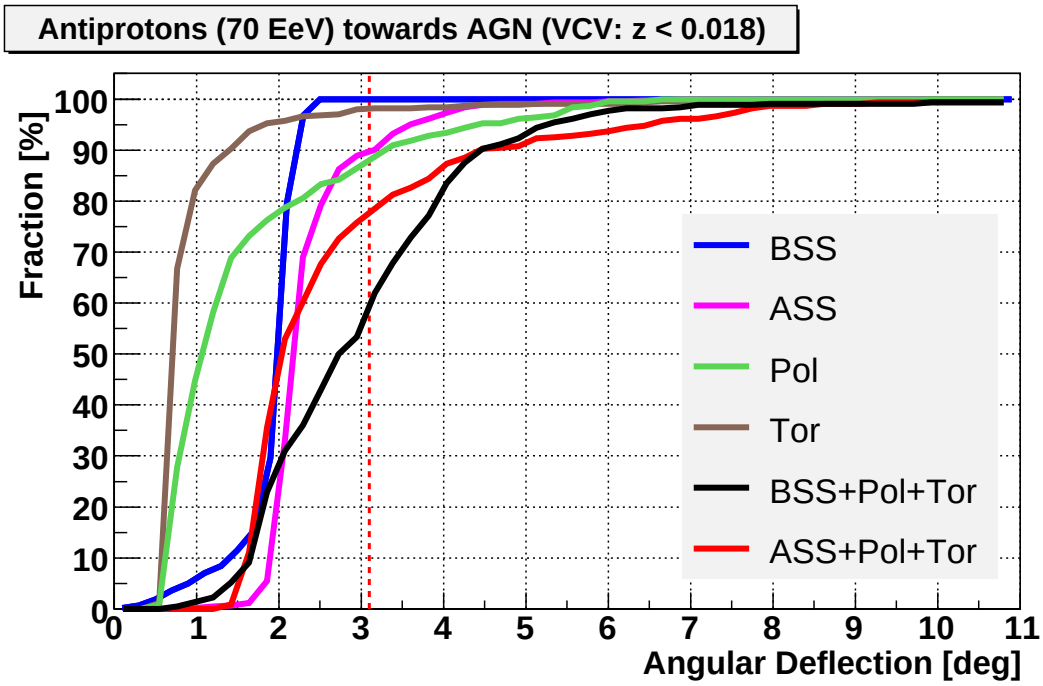

Figure 3.11: Fraction of antiprotons with energy 70 EeV traced from the Earth towards positions of 442 AGN (taken from [Ver06] with redshift lower than 0.018) with deflection angle lower than value on x-axis for given models of Galactic magnetic field.

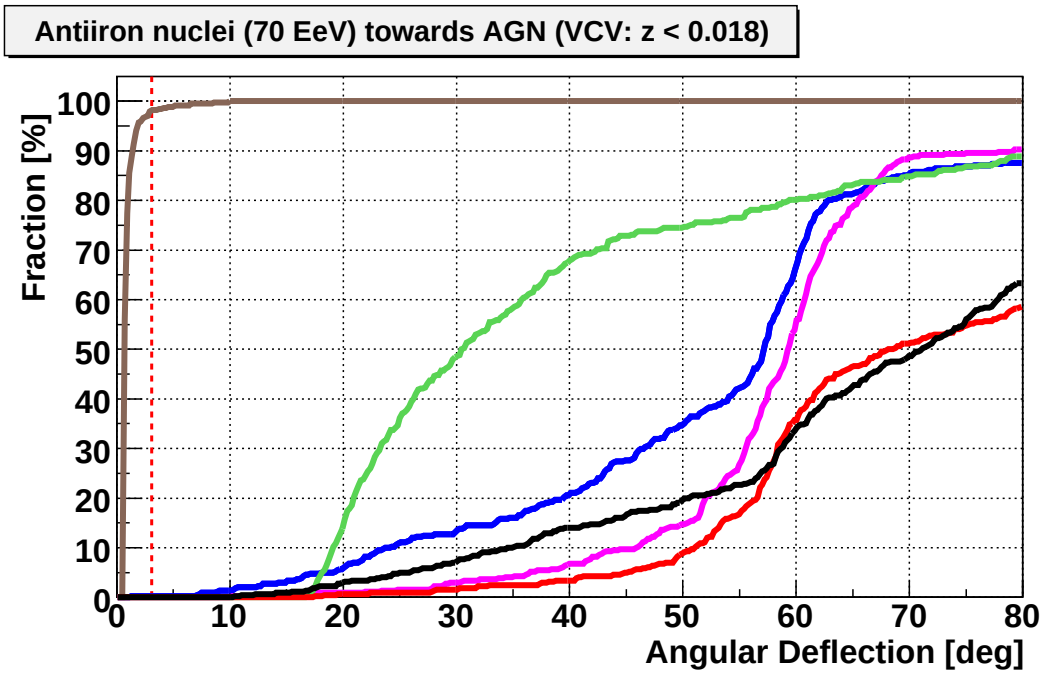

Figure 3.12: Fraction of anti-iron nuclei with energy 70 EeV traced from the Earth towards positions of 442 AGN (taken from [Ver06] with redshift lower than 0.018) with deflection angle lower than value on x-axis for given models of Galactic magnetic field. Meaning of lines is same as in Fig. 3.11.

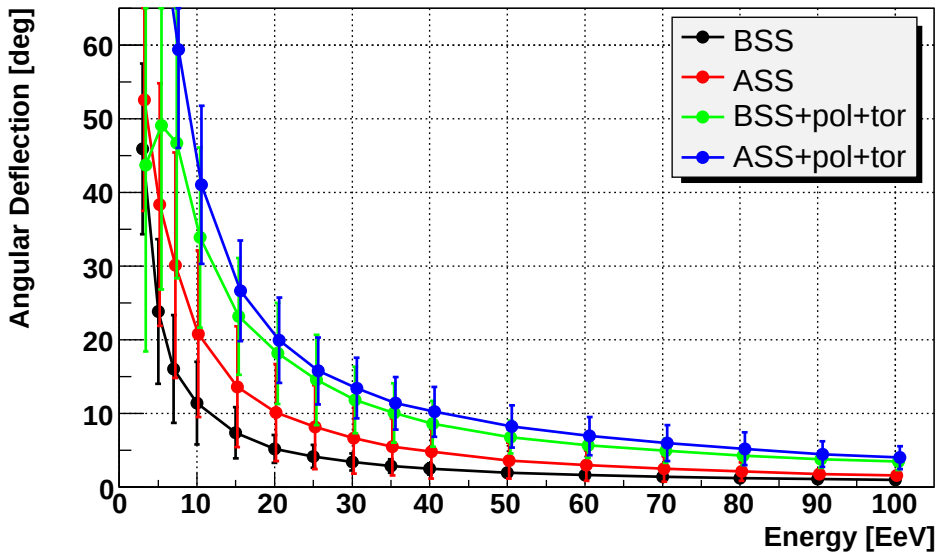

Figure 3.13: Angular deflections of antiprotons starting at the Earth propagating through the Galactic magnetic field of different models as the function of their energy. Velocity vectors of 81 traced antiparticles were pointed within matrix of 3° steps in galactic coordinates. Matrix was centered at the position of Centaurus A (galactic longitude l=309.5° and latitude b=+19.4°). Points show mean value of angular deflections and lines indicate root mean squares of mean values.

Chapter 4

Pierre Auger Observatory

Pierre Auger Observatory is located in the southern hemisphere in western Argentina province of Mendoza close to the city of Malargüe. Detectors cover an semi-desert area of 3,000 km^2 and are overlooked by four fluorescence detector buildings each with six telescopes (see Fig. 4.1). Names of these buildings are: Los Leones (LL), Los Morados (LM), Loma Amarilla (LA) and Coihueco (CO). The geographical coordinates of the array are as follows: 35.1° to 35.5° S and 69.0° to 69.6° W. For more details see Tab. 4.1 and [Abr04].

The size of the detector and particularly the quality of measured data make the observatory unique. One of the most important features of the Pierre Auger Observatory is its hybrid-detector setup. Extensive air showers are detected independently by two different detection techniques (the array of surface detector and the fluorescence detector) which significantly improve quality of shower reconstruction.

4.1 Surface Detector

The water Čerenkov tanks of the surface array are arranged on a regular hexagonal grid with a spacing of 1.5 km. An area of 3,000 km^2 is covered by more than 1600 of these tanks. Each tank is operating completely autonomously and its components

Table 4.1: Geographical coordinates of fluorescence telescope buildings and two laser facilities.

Name	Latitude	Longitude	Altitude
Los Leones	35° 29′ S	69° 27′ W	1421 m
Los Morados	35° 17′ S	69° 01′ W	1423 m
Loma Amarilla	34° 56′ S	69° 13′ W	1484 m
Coihueco	35° 07′ S	69° 36′ W	1719 m
CLF	35° 17′ S	69° 20′ W	1402 m
XLF	35° 11′ S	69° 17′ W	1413 m

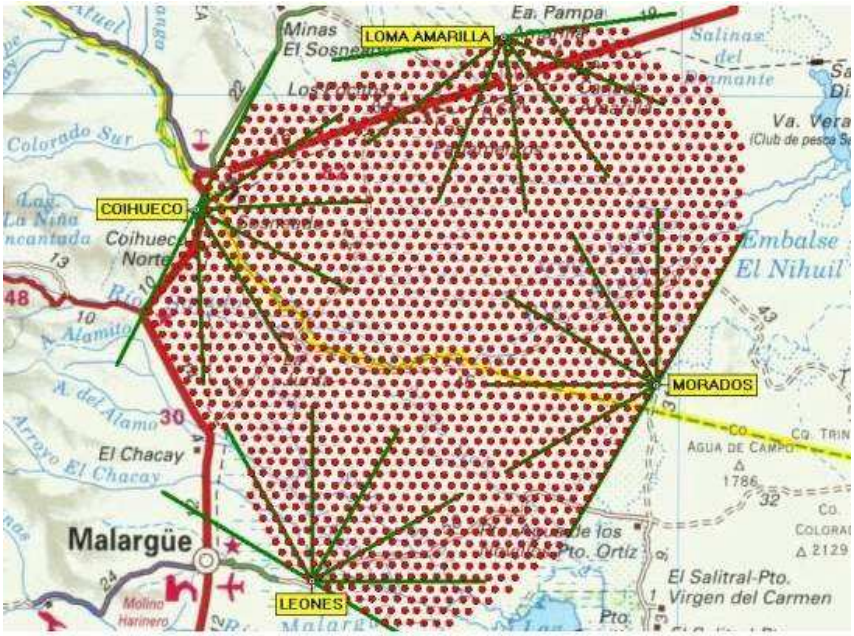

Figure 4.1: Map of the array of the observatory. Red points indicate positions of water tanks of surface detector overlooked by four buildings with fluorescence telescopes: Los Leones, Los Morados, Loma Amarilla and Coihueco.

are shown in Fig. 4.2.

The surface detector station is filled with 12 tons of clean water inside a sealed liner with a reflective inner surface. Charged particle passing through water produces Čerenkov light which is collected by three nine-inch-diameter photomultiplier tubes (PMTs) looking downwards into the water. Signals from PMTs are digitized with 40 MHz sampling rate. The data processing of measured data are described in [Ber06] and [All07].

The low event rate of the highest energy cosmic rays requires an area large enough to accumulate good statistics in a reasonable time. By covering an area of 3,000 km^2, the aperture achieved with the surface array for zenith angles less than 60° is 7,350 km^2 sr. By including events with larger zenith angles (up to 80°) in the analysis, the aperture can be increased by 30%. The detection efficiency at the trigger level reaches 100% for cosmic ray events with energy above 3×10^{18} eV.

The duty cycle of the surface detector is full time in ideal case. Hardware and software problems could affect the operation, but typically more than 98.5% of the stations are operational at any time.

The events recorded by the SD are reconstructed using the arrival time and the signal size from the shower particles reaching the detectors. The magnitude of the signal at 1 km from the intersection of the shower axis with the ground is S(1000), measured in units of vertical equivalent muon (VEM)[1]. The total signal is estimated from the lateral distribution function (LDF) fit as a size parameter of the shower. Two cosmic rays of the same energy, but incident at different zenith angles, will yield

[1]Average signal size given by muon crossing the tank verticaly

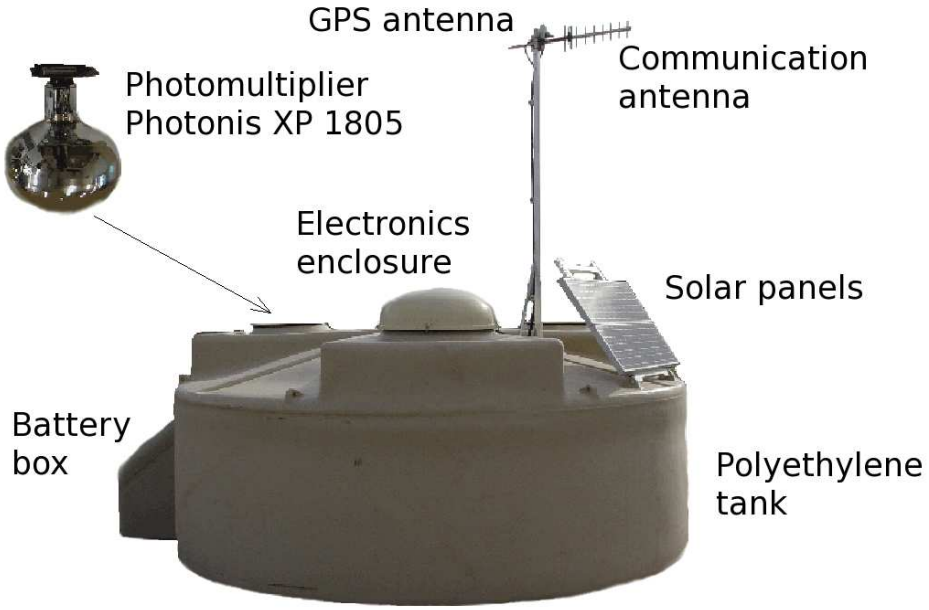

Figure 4.2: Schematic view of the surface detector station showing its main components.

different values of $S(1000)$ due to an attenuation of the shower in the atmosphere. The attenuation curve can be obtained from data.

The shower energy can be obtained from calculations of particle density for given distances from the shower core. However, these calculations rely on Monte-Carlo simulations which require assumptions about the hadronic interaction model and the primary-chemical composition. With the subset of events detected in hybrid mode (simultaneous measurement with both surface and fluorescence detectors) the link between $S(1000)$ for given zenith angle and the primary energy can be established independently using data from fluorescence detector which provides calorimetric energy measurement. The energy obtained from fluorescence detector is only slightly dependent on hadronic interaction models with only small correction to an energy carried by shower components (neutrinos and muons) invisible for fluorescence detector.

The arrival direction of the primary particle is inferred from the relative arrival times of the shower front at different surface detectors. The angular resolution improves with energy and zenith angle because of greater number of triggered stations. The surface array has the angular precision better than 1° in case of measurement of extensive air shower by at least four tanks.

The surface array has the following advantages:

- Almost 100% duty cycle.
- Well-defined aperture that is independent of the energy above 3×10^{18} eV.
- The uniform coverage in right ascension on a daily basis.

- The response largely independent of weather conditions.
- The quality of the data improves with the energy of events.
- The sensitivity to showers arriving at large zenith angles.
- In situ calibration of the detectors by cosmic ray muons.

4.2 Fluorescence Detector

Four buildings each with six telescopes were built atop of small hills on the boundary of the area covered by the surface detector. The telescopes are built like the Schmidt optics (therefore the real image is inverted on a camera: i.e. top and bottom are reversed, as are left and right), consisting of a spherical mirror of radius 3.4 m and a spherical pixel camera. A circular aperture with 0.85 m radius was increased by a ring-shaped corrector lens into 1.1 m while preserving the quality of a spot on the camera. Light is focused by a large 3.5 m $\times$ 3.5 m spherical segmented mirror onto the camera, which accommodates the 30° azimuth $\times$ 28.6° elevation field of view.

The camera is an array of 440 hexagonal pixels, each of them has a field of view of approximately 1.5°. Each pixel has an 8-stage PMT tube (Photonis XP3062) with a 40 mm side-to-side hexagonal photocathode, complemented by light collectors. The photomultiplier array is made of 22 rows and 20 columns.

The center of the spherical mirror and of the camera are both placed on the optical axis, resulting in a fully concentric setup. Only the steel support of the camera, which is mounted on the floor between the mirror and the aperture, adds a small asymmetry (see Fig. 4.4).

All 24 telescopes are operated independently with respect to actual hardware, software and weather conditions. The trigger algorithms are described in [Gem00]. In brief, there is four-layer hierarchy of triggers. The first level trigger (FLT) works on the level of individual pixels. It requires the sum over 10 consecutive time bins of the analog-to-digital converter (ADC) signals to be above the FLT threshold. A fast hardware-implemented second level trigger collects all FLTs from one camera and searches for geometric patterns. The third level trigger (T3) is a software trigger operating on telescope level. T3 algorithm is based on track length and space-time compatibility requirements and selects shower candidates and performs a fast reconstruction of the shower geometry. Calculated direction and time of impact on the ground of good showers are sent to the central data acquisition system (CDAS) in order to trigger data readout of the corresponding parts of the SD array.

The telescopes observe development of the nitrogen fluorescence caused by charged particles of cosmic ray air showers. The number of emitted fluorescence photons is proportional to the energy deposited in the atmosphere due to electromagnetic losses by the charged secondary particles. The timing information of pixels observing the shower is used for the reconstruction of shower geometry. The reconstruction can be improved with combination of measurement from surface detector (hybrid observation) or by a combination of measurement from fluorescence telescopes located in different buildings.

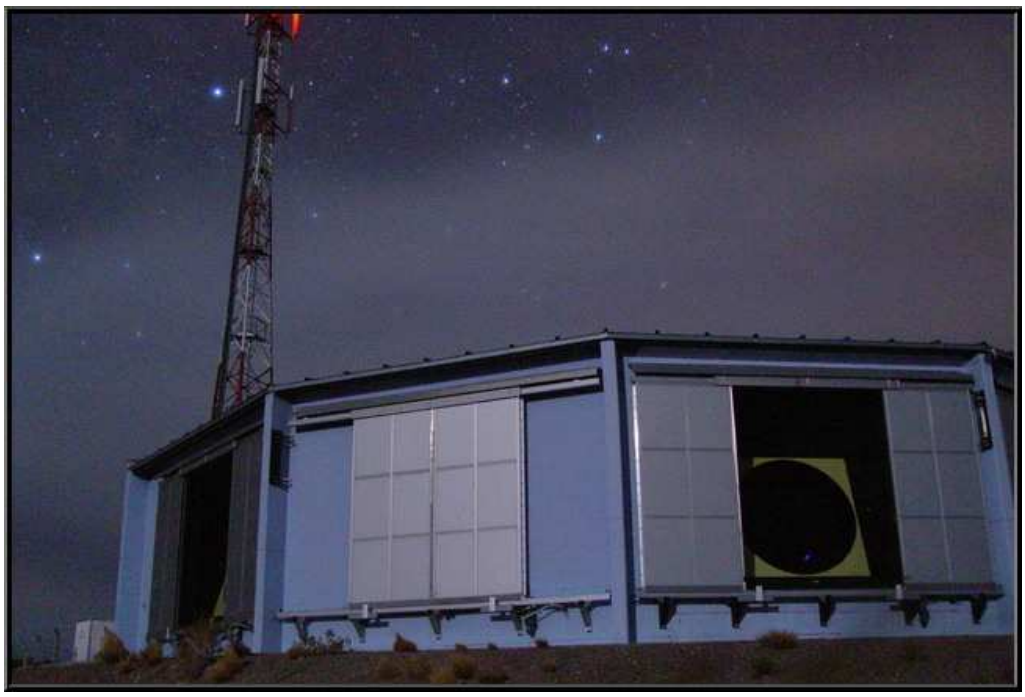

Figure 4.3: Fluorescence detector at Los Leones during observation. Shutters of one telescope are closed because of the moonlight.

The fluorescence detector can be operated only during clear nights with not too bright night sky background (see Chapter 7). It has the following advantages:

- The longitudinal development profile is measured directly.
- Direct observation of a maximum of extensive air shower.
- Reconstructed energy is a function of directly observed amount of light which has to be corrected to a transparency of atmosphere and missing energy (i.e. energy carried away by muons and neutrinos).
- It has lower energy threshold than surface detector.
- A coincidence of a single detector of the surface array with a single fluorescence telescope constrains the shower geometry as precisely as a stereo fluorescence detector.
- Geometry reconstruction improves with an observation from more fluorescence buildings.
- Possibility to detect very inclined and upward extensive air showers.
- Its aperture increases with an energy of cosmic rays, but it changes with the quality of the atmosphere.

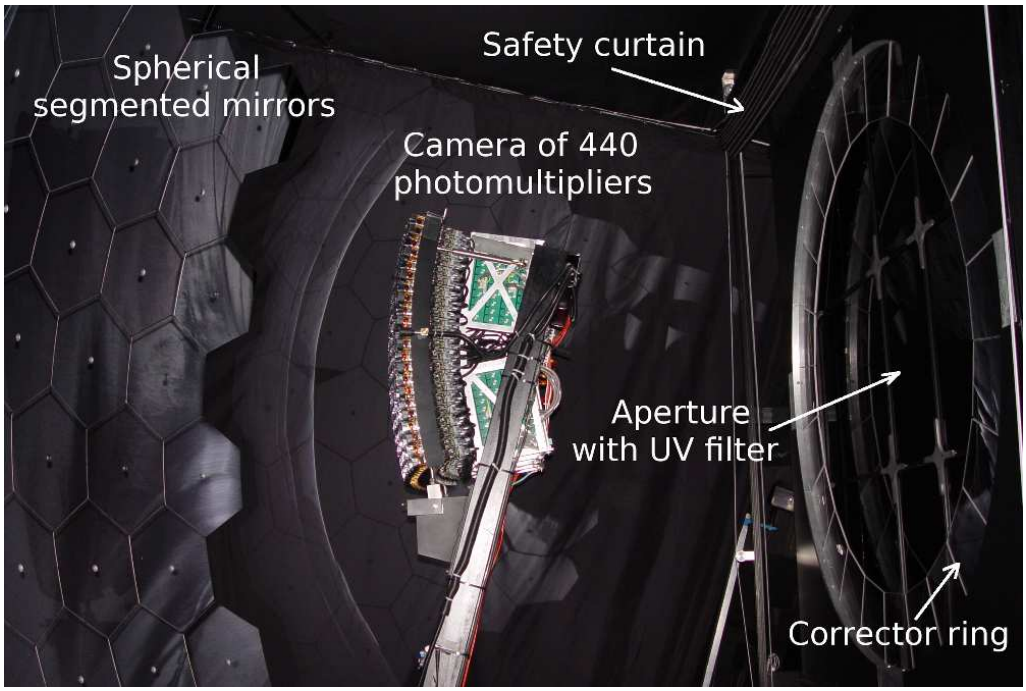

Figure 4.4: Inside a Schmidt telescope at Coihueco. Aperture with corrector ring, safety curtain, camera of 440 PMTs and segmented mirros are visible.

4.3 Atmospheric Monitoring

Since extensive air showers are initiated by primary cosmic ray particles at high altitude above the ground, they propagate through the entire atmosphere. The atmosphere is the largest part of the detector. Thus it is essential to monitor the state of the atmosphere permanently. Weather and atmospheric conditions are very dynamic because the detector is located on the down-wind side of the Andes Mountains.

For optical observations, as it is in case of fluorescence detector, it is important to measure the effect of atmosphere on observed cosmic air showers. Instruments which constantly monitor scattering and atmospheric attenuation of photons (see Fig. 1.8) were deployed at observatory site:

- Radiosondes are launched frequently to measure vertical temperature, density profiles and humidity above the observatory site [Kei04].
- Cloud cameras installed on the top of each telescope building perform a full sky infrared imaging to detect clouds.
- LIDAR (light detection and ranging) stations are placed next to each FD building, to scan the sky for clouds and measure aerosol backscattering with high repetition lasers [Ben07].
- CLF and XLF (central laser facility and extra laser facility) facilities permanently generate a well known sequence of laser events in all telescope detectors

to monitor geometric alignment, timing and aerosol scattering in the atmosphere [Fic06].

- HAM (horizontal attenuation measurement) light source shoots horizontally from one FD building to another to measure horizontal attenuation near ground.

- APF (aerosol phase function) lasers shoot horizontally and in a short distance in front of the FD detectors to observe scattered laser light over a large scattering angle range. This is used to measure the Mie scattering phase function [Ben07b].

- FRAM (fotometric robotic telescope for atmospheric monitoring) robotic telescopes observe a large number of known bright ultraviolet stars in order to detect clouds and attenuation of light in the atmosphere [Ben07c]. It is operated automaticaly and designed also for astronomical measurements [Jel06].

Chapter 5

Results of Pierre Auger Observatory

Pierre Auger Observatory has been collecting data while it was being still under construction. Presented results use data measured since January 2004, when only a small part of the detector was functional. Recently the number of deployed and working detector stations reached 1600 and all 24 fluorescence telescopes were operated, thus the Observatory is fully completed.

Figure 5.1 shows an extensive air shower observed by all fluorescence buildings and triggering also the water tanks. Such air showers independently triggering surface and fluorescence detector provide data for energy calibration of the surface detector by fluorescence measurements and improves angular reconstruction.

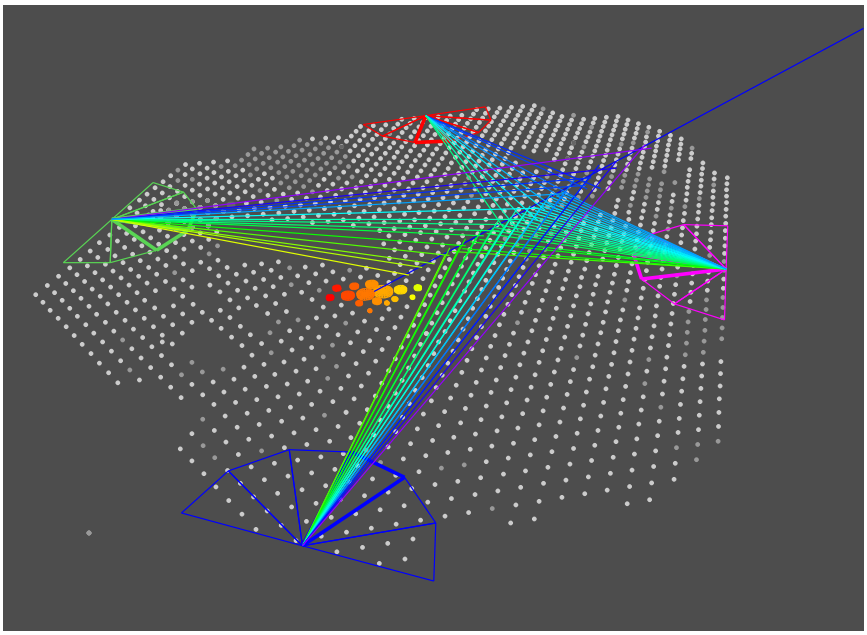

Figure 5.1: Extensive air shower hitting an array of surface detector and fluorescence light simultaneously observed by telescopes at all four buildings.

5.1 Energy Spectrum

The shape of the energy spectrum of cosmic rays with the highest energy can be formed by several mechanisms (see Section 1.7). In particular very important is the end of cosmic ray spectra, where the rapid decrease of cosmic ray flux is expected as has been predicted by GZK mechanism. A comparable decrease can be also caused by losses of acceleration efficiency in (still unknown) sources. A superposition of cosmic ray spectrum from different sites of origin (e.g. galactic and extragalactic) can play crucial role in spectrum formation.

The comparison of cosmic ray fluxes measured by Pierre Auger Observatory and previous experiment HiRes is shown in Fig. 5.3. Data from Pierre Auger Observatory shows constant cosmic ray flux with spectral index equal to 2.69 between 4×10^{18} eV and 4×10^{19} eV. The spectral index above 4×10^{19} eV changes to 4.2 and a single power-law hypothesis above 4×10^{19} eV is rejected with a significance of more than 6 standard deviations [Abr08c]. The observed suppression of cosmic ray flux is consistent with the prediction of GZK mechanism, but effects caused by sources cannot be yet excluded.

Both HiRes and the Pierre Auger Observatory cosmic-ray energy spectra indicate rapid decrease of the flux at the highest energies. On the contrary japanese experiment AGASA indicates no rapid decrease of cosmic ray flux at the highest energies. There was observed also discrepancy in absolute energy scale of cosmic ray fluxes measured by surface and fluorescence detectors. It could come from the conversion of measured quantities into the energy: the absolute fluorescence yield and the atmospheric attenuation in the case of fluorescence observation and the conversion of measured lateral distribution function into the energy in the case of surface detector.

The hybrid detection represents a clear advantage in absolute energy determination, because otherwise the dependence on knowledge of interaction models or of the primary composition is incomplete. Using information from FD the energy corresponding to SD energy estimator S_{38° can be estimated with small corrections to missing energy (i.e. fraction of air shower energy not measured by FD). The energy calibration was obtained for a subset of high-quality events measured simultaneously by SD and FD (i.e. hybrid events) [Abr08c]. The correlation between FD energy E_{FD} and SD energy estimator S_{38° is shown in Fig. 5.2.

Fluorescence detector uncertainties dominate systematic uncertainties of energy determination in the results from Pierre Auger Observatory - above all the systematic uncertainties in fluorescence yield, calibration and reconstruction. Activity on several fronts are in progress to reduce them. Total systematic uncertainty is 22% at present.

Another uncertainties in energy spectrum obtained solely from fluorescence observation could come from the exposure calculation. The calculation depends on the assumptions about hadronic interaction models, chemical composition of primary cosmic rays and spectrum slope. Therefore the energy spectrum is taken either from surface detector[1] or hybrid measurements. The hybrid spectrum measured by the

[1] Even if the energy calibration is based on fluorescence data.

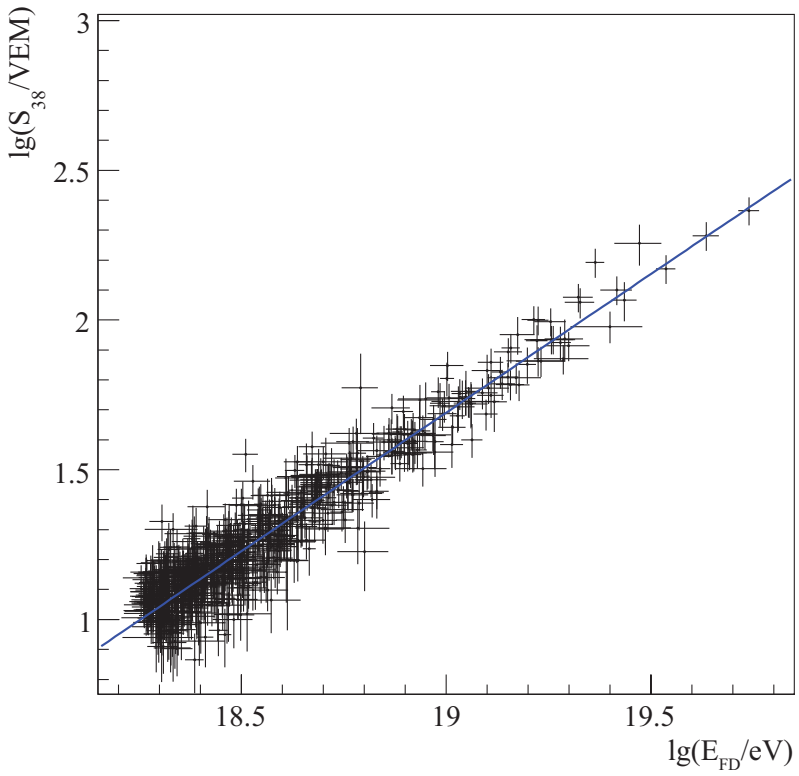

Figure 5.2: Correlation between parameter S_{38° and energy measured by FD obtained for hybrid events. The full line is the best fit to data.

Pierre Auger Observatory can be found in Fig. 5.4.

5.2 Upper Limit on Photon and Neutrino Fluxes

Neither photons or neutrinos were detected above 100 TeV yet. Both of them are stable and neutral particles which are not affected by magnetic fields during their propagation in space and therefore they point back to their sources. The successful detection of ultra high energy photon or neutrino will open the discussion about their origin, which could solve the whole mystery of cosmic rays and lead to discovery of point sources or indicate a need for a "new" physics. The detection of small flux of ultra-high energy photons could among others confirm GZK mechanism.

The Pierre Auger Observatory has sensitivity for detection of photons. Measured upper limit on the fraction of photons in the integral cosmic-ray flux is shown in Fig. 5.5. The limit ruled out many top-down models of cosmic-ray origin and in the future it could reach the level of GZK photons (i.e photons produced during interaction of UHECRs with CMB).

The surface detector of the Pierre Auger Observatory is sensitive to Earth skimming tau neutrinos that interact in the Earth's crust. The upper limit on a diffusive flux of tau neutrinos is based on analysis of nearly horizontal showers at EeV energies and presented in Fig. 5.6.

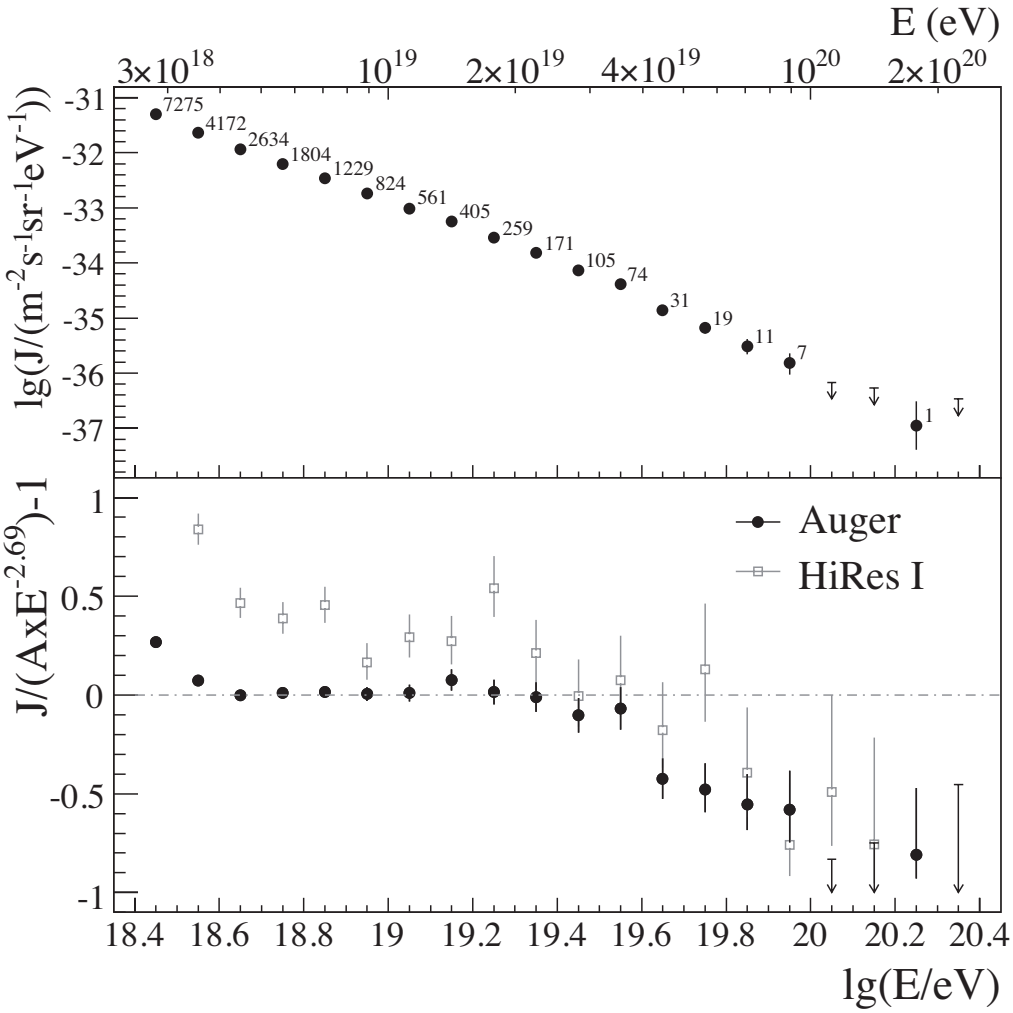

Figure 5.3: Differential flux as function of energy, with statistical uncertainties (upper panel) and fractional differences between Auger and HiRes mono data compared with spectrum with index of 2.69.

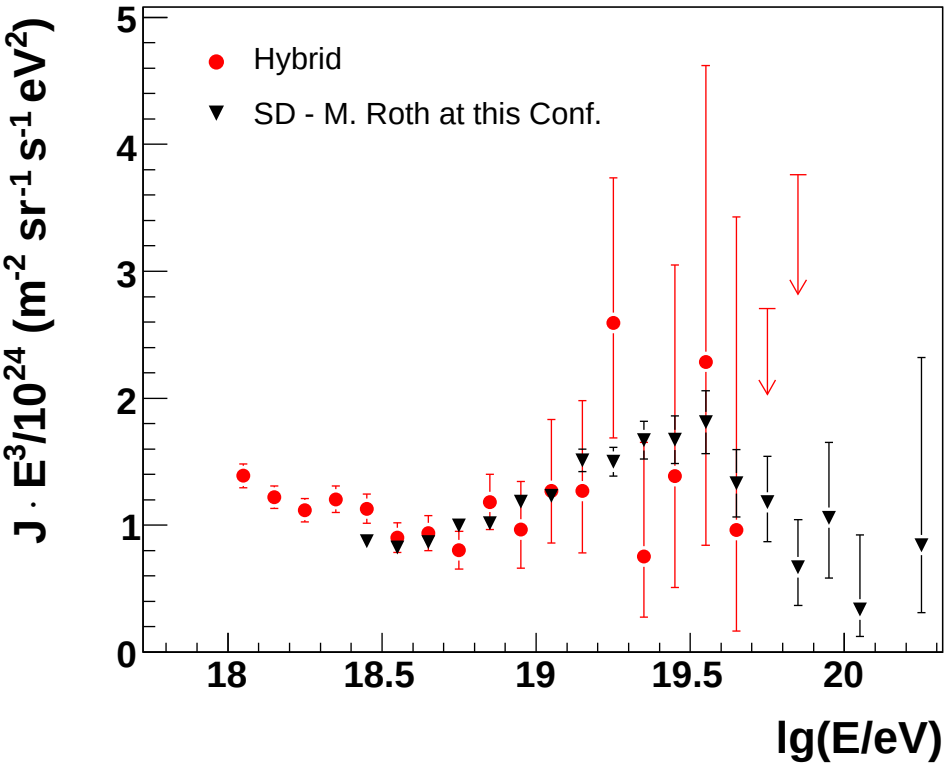

Figure 5.4: Hybrid energy spectrum shown in comparison with surface detector spectrum presented at International Cosmic Rays Conference 2007 [Per07]. Only statistical uncertainties are given here.

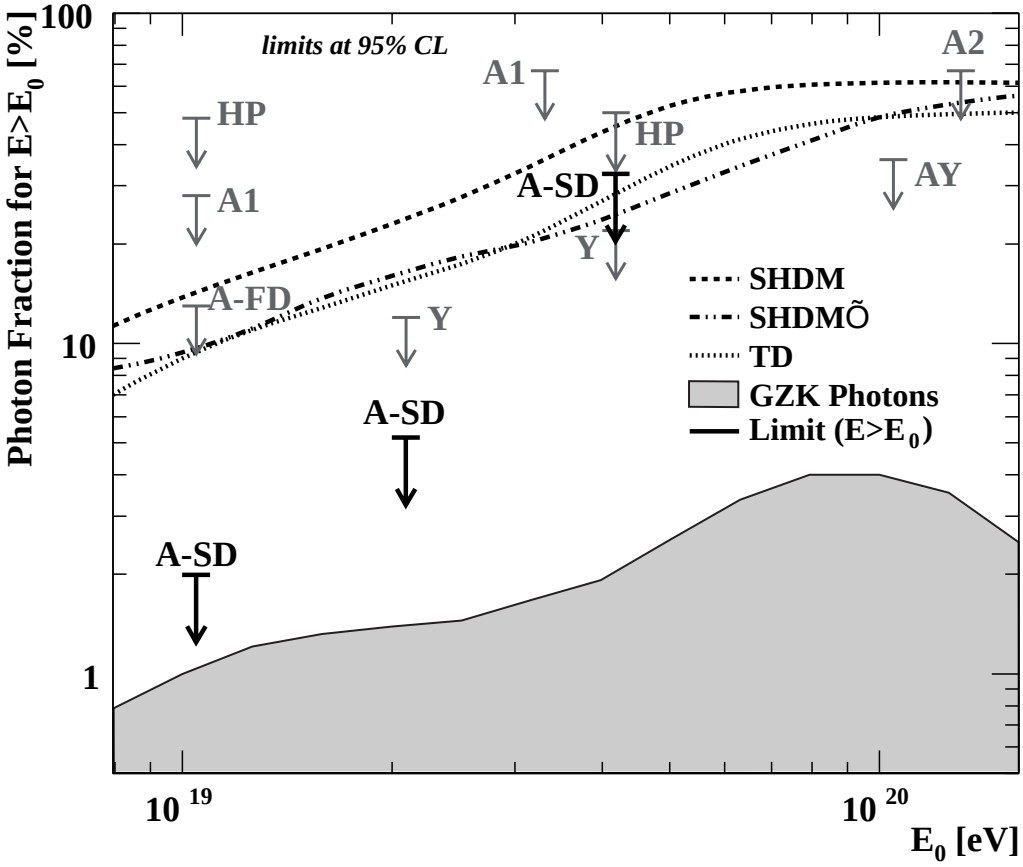

Figure 5.5: Upper limits on the fraction of photons in the integral cosmic-ray flux compared to the expected fluxes of photons coming from the annihilation of dark matter. Points labeled as A-SD (A-FD) belongs to results from SD (FD) observations at the Pierre Auger Observatory. Other points show results from previous experiments [Abr08a]. Lines indicate predictions on photon flux for different models.

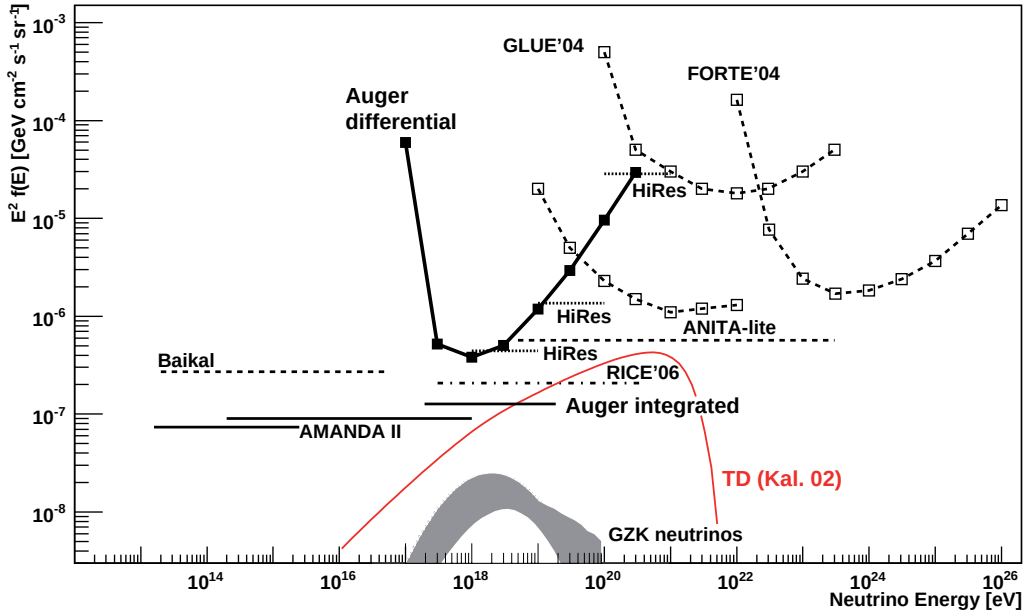

Figure 5.6: Limits at the 90% confidence level for a diffuse flux of tau neutrinos ν_τ assuming a 1:1:1 ratio of the 3 neutrino flavors and predictions for a top-down model. Figure from [Abr08b].

5.3 Chemical Composition

The chemical composition can be studied indirectly by a comparison of observed properties of extensive air showers with the predictions of simulations for different nuclei. In Fig. 5.7 the mean air depth of the shower maximum X_{max} is shown as a function of energy together with the predictions from air shower simulations. Observed data suggests transition from heavy to light elements in the ankle region. For the highest energies the transition seems to change back from light to heavier elements. The comparison of observed data with two theoretical predictions (discussed in Section 1.7) are also shown.

Hadronic interactions used in air shower simulations for cosmic-ray energies studied by the Pierre Auger Observatory are extrapolated from measurements made at energies many magnitudes lower. Therefore the interpretation of the comparison of measured and predicted data is questionable.

A comparison with previous experiment HiRes shows agreement within their uncertainties at the highest energies. Still data collected by the Pierre Auger Observatory has significantly larger statistics and its statistical precision exceeds that of the preceding experiment.

5.4 Anisotropy of Arrival Directions

As was discussed in Chapter 3 and shown in Figures 5.5 and 5.6 the majority of cosmic rays are charged particles. Their trajectories are therefore deflected during propagation towards the Earth. Only in the case of protons with energy above

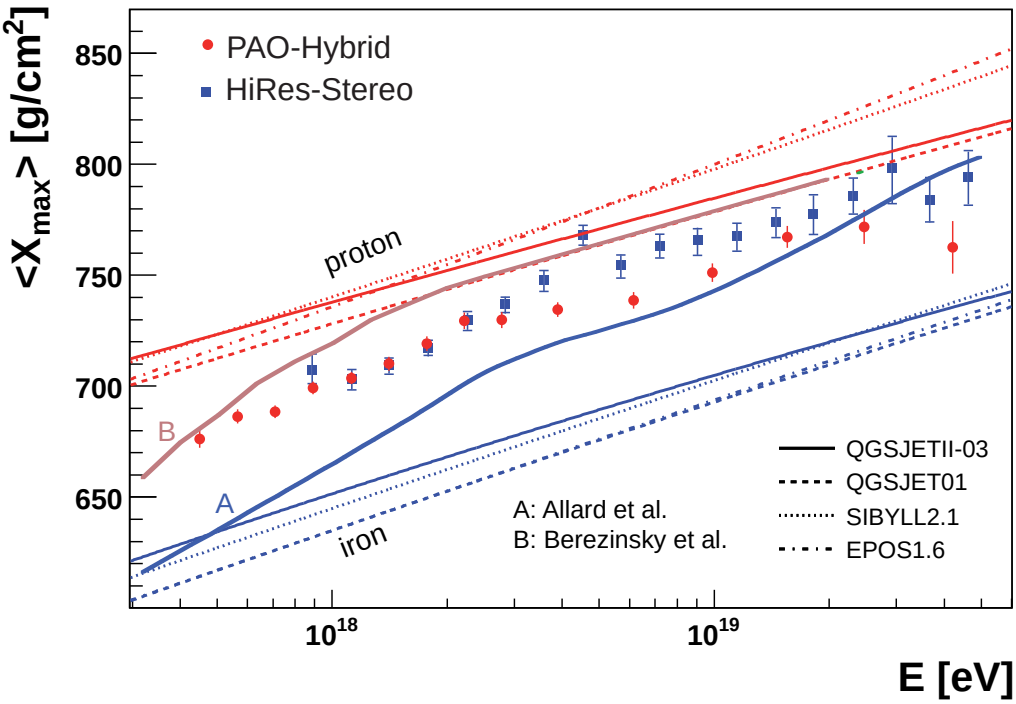

Figure 5.7: Mean X_{max} as a function of energy for HiRes stereo and Pierre Auger Observatory hybrid data compared to proton and iron predictions using different hadronic interaction models (solid curves) and different models of UHECR origin. Figure from [Ung07].

50 EeV the arrival directions on the Earth can point back towards sources within few degrees as arises from particle tracking simulations for several models of galactic and extragalactic magnetic field (see Chapter 3).

The neighbourhood of the Galactic center is a promising region for anisotropy analysis of arrival directions of observed cosmic rays. Due to interactions of accelerated particles with ambient matter the neutrons could be produced. The distance of the Galactic center from the Earth is 8.5 kpc and a significant fraction of neutrons with energy higher than EeV will survive their path to the Earth. As neutral particles the neutrons will point back to their site of origin, which in discussed case will be around the position of the Galactic center. The exposure of the position of the Galactic center at the Pierre Auger Observatory is significantly higher than that of previous experiments. No excesses of cosmic rays coming from any area around the position of the Galactic center have been observed. An upper bound on the flux of neutrons was set.

Analyses of observed arrival directions on different angular scales of the sky were studied and no hint for signal above expected background level was found below 57 EeV. There is no excess from the directions of local Galactic magnetic spiral arm and no lack of events coming from perpendicular directions to the local Galactic magnetic field arm. The explanation of this pattern could be a large fraction of heavy nuclei as primary particles of cosmic rays with either galactic or extragalactic origin or eventually very strong turbulent magnetic fields.

The anisotropy of the arrival direction of cosmic rays was observed for cosmic rays with energy higher than 57 EeV [Abr07b]. At first the measured data were scanned within angular distances from the positions of AGN contained in the 12th edition of the Veron & Veron-Cetty catalogue [Ver06], within the redshifts of AGN and also within the energies of observed cosmic rays. The maximal signal was found for the angular distances less than 3.1°, maximal redshift z =0.018 and minimum energy of 56 EeV. In the sample data 12 from 15 measured events with reconstructed energies above 56 EeV had angular distance between their arrival direction and the positions of tested AGN lower than 3.1 degrees.

A sequential statistical test was then constructed for an examination of a posteriori-found anisotropy and it passed already after 8 observed events. The new maximal signal was found with following parameters: maximal angular distance 3.1°, maximal redshift 0.017 and minimum energy 57 EeV. The area with radius equal to 3.1° around the positions of AGN closer than 75 Mpc (i.e. redshift less than 0.018) covers 21% fraction of the sky weighted with the exposure function of Pierre Auger Observatory [Som01]. Altogether 20 from 27 events hit tested fraction of the sky as can be seen in Figure 5.8. The hypothesis of an isotropic distribution of arrival directions of observed cosmic rays above 57 EeV in the sky was rejected with at least a 99% confidence level.

Data sample contains 5 from 7 non-correlating cosmic ray events which arrived very close to the position of Galactic disk, where astronomical observations of AGN are limited. The interstellar matter in our Galaxy obscures observations of any object behind it. In addition the influence of the Galactic magnetic field becomes very important for such particles passing through the Galactic disk and their deflection is therefore larger that from other directions.

The possible correlation of the highest-energy cosmic rays with the positions of nearby active galactic nuclei was discussed in [Abr08]. Current data still does not prove that the AGN are sources of the observed cosmic rays. The uncertainty of arrival directions is too large and moreover the chemical composition remains unclear. Therefore the magnetic deflection cannot be estimated. The observation of energy-dependent structures in measured data might be of help to identify the sources of the most energetic cosmic rays.

The comparison with matter distribution in local Universe shows lack of observed cosmic rays from the region where the Virgo cluster is located. Especially when this region is compared with cosmic ray events arrived close to the position of the nearest quasar Cen A. However, we have to be aware that the exposure of the Pierre Auger Observatory for the position of Cen A is about 2.7 higher than for the region with the Virgo cluster.

If the nearest AGN to the positions of events observed by the Pierre Auger Observatory are real sources of these events, than large fraction of protons as primary particles will be favorized. Otherwise the angular deflections are expected to be larger than 3° as leads from the results presented in Chapter 3.

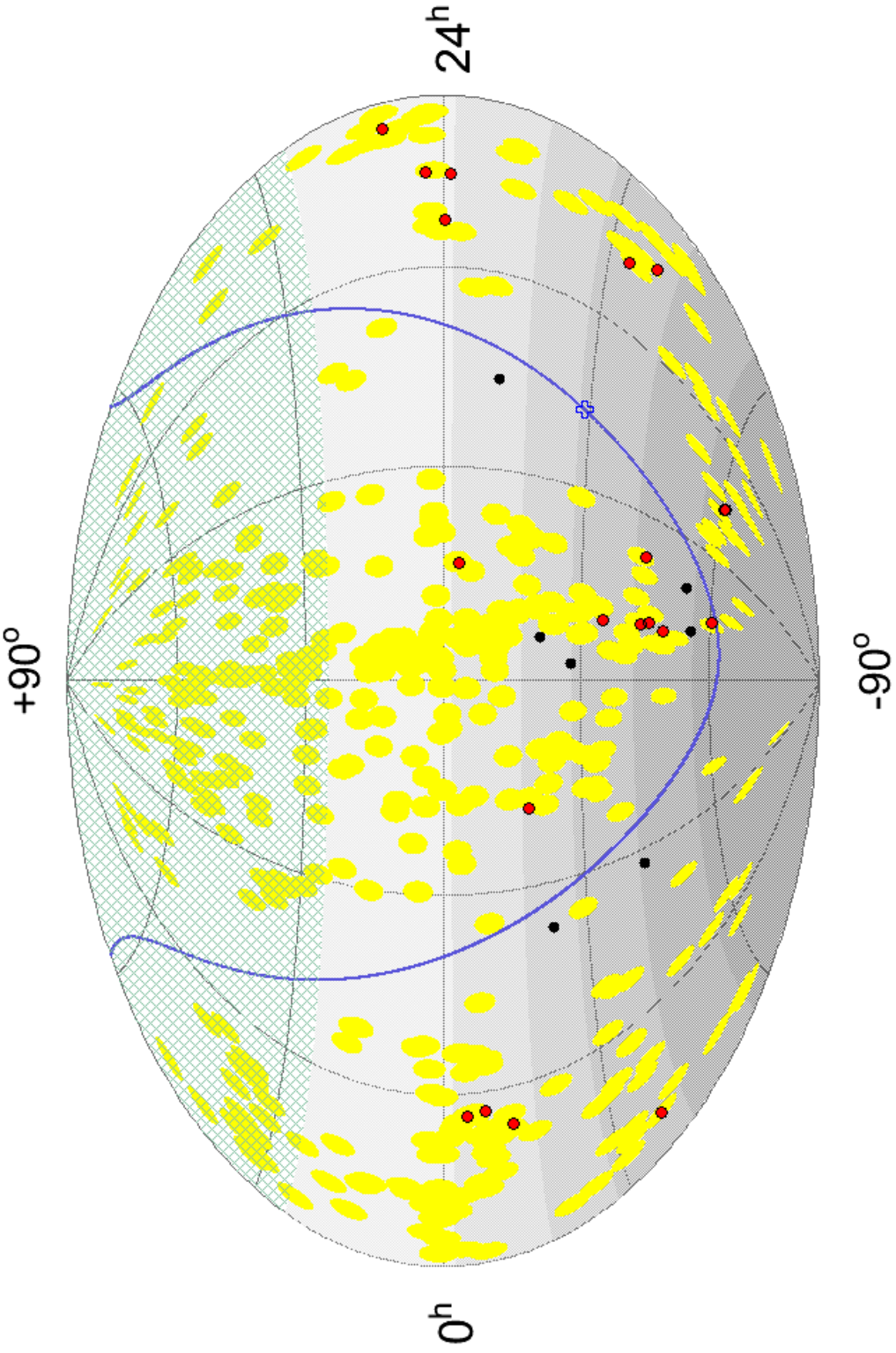

Figure 5.8: Aitoff projection of the celestial sphere in equatorial coordinates. Yellow areas indicate 3.1°-radius neighbourhoods around the positions of AGN with redshifts less than 0.018. Gray-shaded zones indicate equal exposure areas and green-shaded sky area is not visible by the observatory. The positions of observed cosmic rays with $E > 57$ EeV are red (black) points for those which lie inside (outside) yellow areas.

Chapter 6

Gamma-Ray Bursts

Gamma-ray bursts (GRBs) were since their first observation considered as a possible source of ultra-high energy cosmic rays. Gamma-ray bursts are the most energetic known sources of γ-rays yet and are continuously observed since 1970s [Kle73] by satellite experiments. Several authors predicted a conversion of significant fraction of the energy of the GRB into the burst of cosmic-ray particles (e.g. [Wax00] and [Der03]).

Although the most energetic processes occur in them, there is a big difficulty with observations of UHECRs coming from their sites. They are located at large cosmological distances and the incoming flux of particles with the energies above 40 EeV from them will be affected by the GZK mechanism. We will not discuss several mechanisms which could lower energy losses during the propagation of UHECRs, but we will rather focus on experimental data. The study of space-time relation between the data observed by γ-rays satellite detectors and cosmic rays measured by the Pierre Auger Observatory will be presented in the following chapter.

6.1 Catalogue of Gamma-Ray Bursts

The catalogue of 397 GRBs located more accurately than 1° observed since January 1, 2004 till May 1, 2008 was compiled using two online databases: Jochen Greiner's webpage [Gre] and GRBlog [Grb]. Both databases compile data primarily from the Swift mission complemented by measurements from additional GRB observing satellites, including HETE, INTEGRAL, and others. The sky positions of all GRBs in equatorial coordinates are shown in Fig. 6.1. As expected ([Mee92] and [Pac99]) they cover the whole sky isotropically.

Out of the total GRB sample, 298 bursts are within the field of view of Pierre Auger Observatory defined by maximal zenith angle $\theta_{max} = 70°$ (i.e. a declination of such positions of GRBs must satisfy the condition $\delta_{grb} < (\theta_{max} - \mid a_0 \mid)$). Moreover the positions of 123 GRBs were observable during their burst, i.e. $\theta_{grb} < \theta_{max}$ (see Table 6.1). These directly observed GRBs during their γ-ray activity are important for the monitoring of CR which could arrive within a few seconds before or after the bursts.

It has been proved that GRBs are cosmologically distant objects [Met97]. Till

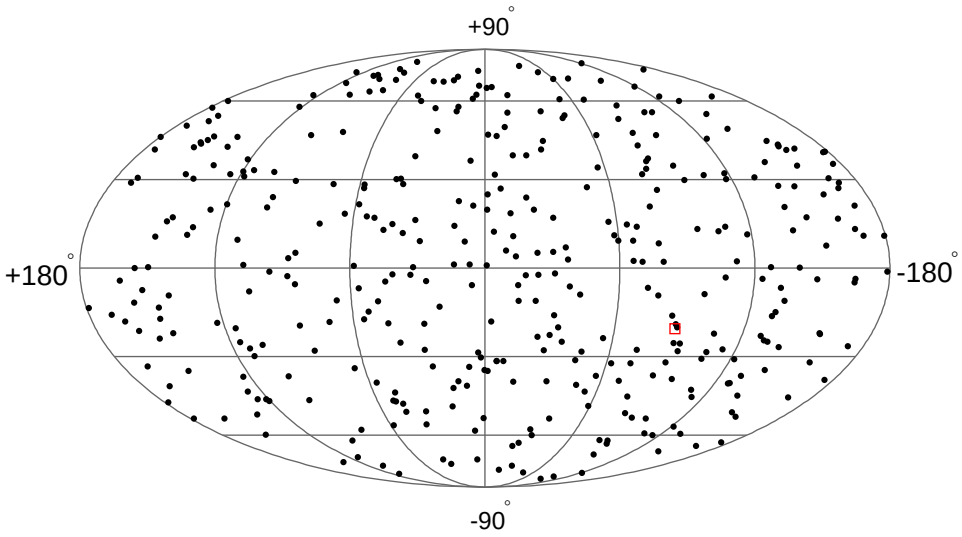

Figure 6.1: Black points indicate positions of 397 well-localized GRBs in equatorial coordinates from the catalogue. Red square shows position of magnetar SGR 1806-20.

Table 6.1: Numbers of GRBs (N_{grb}) observed for three ranges of zenith angle θ with an airmass for maximal zenith angle. The maximal values of the declinations for the circumpolar position in the sky (δ_{cp}) and numbers of circumpolar GRBs (N_{cp}) are written in two rightmost columns.

θ	airmass	N_{grb}	δ_{cp}	N_{cp}
$< 60°$	1.99	92	-84.8°	0
$60° \div 70°$	3.05	31	-74.8°	6

the end of April 2008, 148 redshifts of GRBs were measured [Gre]. The values of redshift spread wide range from $z \approx 0.0085$ to a very high redshift at $z \approx 6.29$, see Fig. 6.2. Knowing their redshifts, distances of GRBs can be estimated within current cosmological model (we used following parameters for ΛCDM cosmological model: Hubble constant $H_0 = 70$ km/s/Mpc, matter density $\Omega_m = 0.3$ and cosmological constant $\Omega_\Lambda = 0.7$). The mean path travelled by γ-rays coming from GRBs was calculated to be about 3 Gpc adopting an average redshift $\langle z \rangle \approx 1.8$.

6.2 Time Delay of Massive Particles

As was shown in the previous section the typical path length travelled by γ-ray originated in a GRB to the Earth is a few Gpc. The time delay of a massive particle after γ-ray, both starting from the GRB at the same time, depends upon particle mass and charge. The first step of the analysis is the calculation of time delay between γ-rays and massive particles.

The time delay of a neutral massive particle created simultaneously as γ-rays can be estimated from their path difference ΔD. After time T, an ultra-relativistic

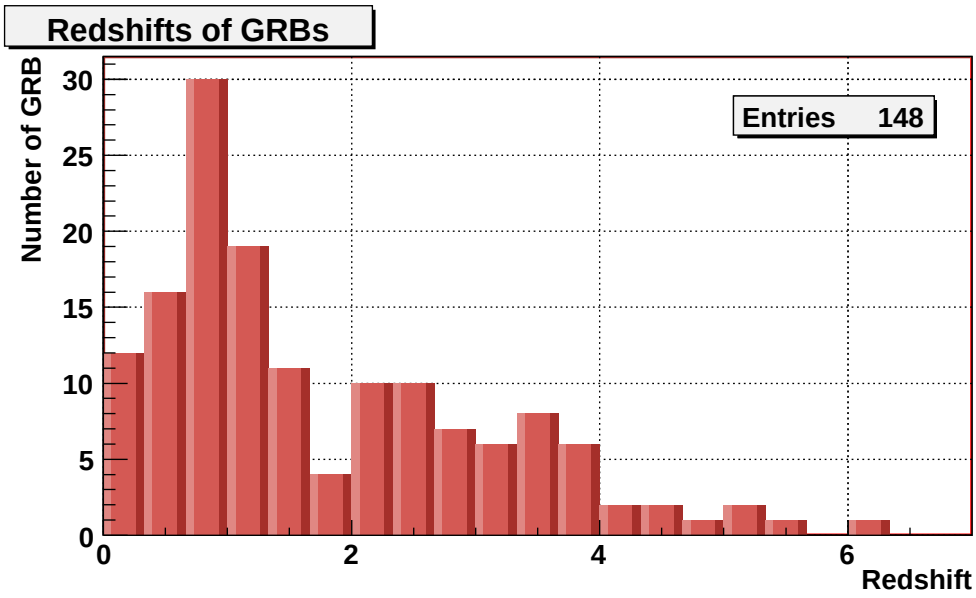

Figure 6.2: Distribution of measured redshifts of GRBs detected till May 2008.

massive particle[1] lags behind γ-rays. The neutral massive particle with Lorentz factor Γ and born within a region of GRB at the same time as γ-ray comes to the Earth atmosphere with the time delay ΔT

$$\left(\frac{D}{\mathrm{Mpc}}\right)\ \mathrm{s}.\Delta T \approx 5\times 10^{13}\,\Gamma^{-2}\left(\frac{D}{\mathrm{Mpc}}\right)\ \mathrm{s}. \tag{6.1}$$

For example, an ultrarelativistic neutral particle coming from a 3 Gpc distant source of GRB with a Lorentz factor $\Gamma \approx 10^{11}$ ($E \approx 100$ EeV for the rest mass $m_0 \approx 1$ GeV) is delayed about $\Delta T \approx 15\,\mu$s ($\Delta D \approx 4.5$ km) with respect to associated incoming γ-rays.

The particle with an electric charge is deflected in extragalactic magnetic fields (EGMF). Although the strength of EGMF is still unknown, there was placed the upper limit on its strength $|\overrightarrow{B_{EGMF}}| < 10^{-9}$ G. In the Universe the regions can be found, where the strength of EGMF is much stronger, such as in the vicinity of the group of galaxies (see Fig. 3.1), but we adopt only one value of EGMF to make a simple estimate. The deflection of a very high energy proton with the energy E propagating the distance D in the extragalactic magnetic field B with a correlation length l_c leads to the time delay (see [Wax95]):

$$\Delta T \approx 200\left(\frac{D}{100\ \mathrm{Mpc}}\right)^2\left(\frac{E}{100\ \mathrm{EeV}}\right)^{-2}\left(\frac{B}{10^{-11}\mathrm{G}}\right)^2\left(\frac{l_c}{10\ \mathrm{Mpc}}\right)\mathrm{yr}. \tag{6.2}$$

Because of the presence of EGMF, the time of flight of a charged particle is very large compared with time of flight of a neutral one. The proton with the energy

[1]The velocity of the particle with the Lorentz factor $\Gamma \gg 1$ is approximately $\beta = \sqrt{1-\Gamma^{-2}} \approx c\left(1-\Gamma^{-2}/2\right)$, where $\beta = v/c$ and c is the speed of light in the vacuum.

$E \approx 100$ EeV born simultaneously with γ-rays at the distance $D = 3$ Gpc and travelling inside cells with the correlation length $l_c = 10$ Mpc containing EGMF with the strength B $= 10^{-10}$ G comes approximately $\Delta T \approx 18$ Myr later behind corresponding γ-rays.

To summarize, only stable neutral particles, e.g. neutrinos or photons, can survive a long path from GRBs situated at cosmological distances and arrive undeflected by the magnetic fields to the Earth within a time interval ΔT before or after γ-rays detected by satellite experiments.

Extensive air showers induced by neutrinos or photons can be identified and separated from EAS initiated by nuclear primaries. EAS initiated by high energy photons are in general expected to have a relatively large depth of shower maximum X_{max} and fewer secondary muons compared to nuclear primaries (see [Abr07a] and [Abr08a]). The neutrino can penetrate deeply into the atmosphere due to the small cross-section and interact at all possible slant depths. The most promising identification of neutrinos would be highly inclined showers (i.e. zenith angle $\theta > 80°$). Another channel in which one of three flavors of neutrinos, τ neutrino, could be observed are the transits through the Earth. Such Earth-skimming neutrinos could convert into τ lepton in the Earth's crust which will then decay into the shower in the atmosphere above the detector [Abr08b].

6.3 Dataset of Cosmic Rays

The events collected by the Pierre Auger Observatory from January 1st, 2004 to May 1st, 2008 were used in the analysis. They have to pass the reconstruction quality criteria, but the criteria for maximal zenith angle were relaxed to higher value, $\theta < \theta_{\rm max} = 70°$. No effect of the detection efficiency as a function of zenith angle θ was adopted in our analysis.

Since January 2004, during 52 months of the data taking, the Pierre Auger Observatory detected more than one million CR events satisfying above-mentioned conditions. Those CR events that came from a direction defined by a spherical cap of a given radius ϑ_{sep} around a position of GRB were considered. Time differences between arrival times of collected CR events and observation times of corresponding GRBs (GRB-CR time differences) were determined. The rates of CR events observed around each position of GRB were calculated for two spherical caps with $\vartheta_{sep} = 5°$ and $30°$.

Most of the positions of GRBs are observable only during a part of a day and the rate of CR in their vicinity can be given only for the separate parts of time differences. The rates of CR events arriving from their directions can be determined only for corresponding time differences between their observation and CR detection. The special cases are 6 circumpolar positions of GRBs. These objects with the declination less than $\delta_{CP} = \theta_{max} + \mid a_0 \mid -180°$ do not leave the detector's field of view. Their equatorial and horizontal coordinates at the Pierre Auger Observatory location during the time of the bursts are shown in Table 6.2.

Although circumpolar positions of GRBs are observable full time the rates of CR in their vicinity could be restricted by the detector acceptance and efficiency.

Table 6.2: Table shows six circumpolar GRBs for $\theta_{max} = 70°$. Name of GRB, UTC time, equatorial coordinates (right ascension α_{grb} and declination δ_{grb}) and zenith angle at the location of the Pierre Auger Observatory (zenith angle θ goes from zenith to horizon) during their bursts are mentioned.

GRB	UTC	α_{grb}	δ_{grb}	θ
071112A	1194891813	260.2	-80.9	45.7
070509A	1178678908	238.0	-78.7	46.3
070508A	1178597899	312.8	-78.4	56.0
061027A	1161944102	270.8	-82.2	61.7
061006A	1160153151	111.1	-79.2	54.8
041219C	1103488233	344.0	-76.8	42.2

We will not give any limits on CR fluxes from GRBs, so the question about detector behaviour at given zenith angle for given energy will not be discussed. An area of a spherical cap around a position of GRB is inside the field of view of Pierre Auger Observatory only if the radius of an area satisfies the condition $\vartheta_{sep} < (\mid \delta_{GRB} \mid - \mid \delta_{CP} \mid)$. Such condition is valid for all GRBs shown in Table 6.2 and the radius $\vartheta_{sep} = 5°$.

We bin CR events coming from directions defined by spherical caps of radii $\vartheta_{\rm sep} = 5°$ and $\vartheta_{\rm sep} = 30°$ around GRB positions. We determine the total number of coincidence candidates by counting the number of CRs found within each of the specified cones. The number of coincidence candidates for 30° is $\mathcal{N}_{30°} = 3,699,269$ whereas for 5°, $\mathcal{N}_{5°} = 104,987$. Note that for 30° the number of coincidence candidates is larger than the total number of CRs in the sample, since a given CR may lie within 30° of more than one GRB. Differences between the observation times of the GRBs and the arrival times of CR events in the same angular bin were determined. In Fig. 6.3, we show the rates of CR events as function of the GRB-CR time difference for the two angular radii $\vartheta_{\rm sep}$ around the positions of GRBs. We consider a 100-day period before and after the GRB observation.

Since neutral CR particles originating in GRB cannot arrive from a direction more than 5° away from a particular position of GRB, the rate of CR events observed in the larger regions around the positrons of GRBs ($\vartheta_{sep} = 30°$) should be lower if neutral particles coming from GRB were detected. However, both distributions are consistent within statistical errors. No significant excess after the time of the bursts is evident in the data (see [Anc07]).

6.4 Flare from Magnetar SGR 1806-20

The giant flare on December 27th, 2004 from SGR 1806-20 represents one of the largest events captured in almost three decades of monitoring the γ-ray sky. The burst saturated many satellite γ-ray detectors [Pal05]. This unique flare lasted about 5 minutes (the duration of the initial spike was ~ 0.2 s), had the peak luminosity of $\sim 2 \times 10^{40}$ W and the total energy emission of $\sim 5 \times 10^{39}$ erg [Woo06].

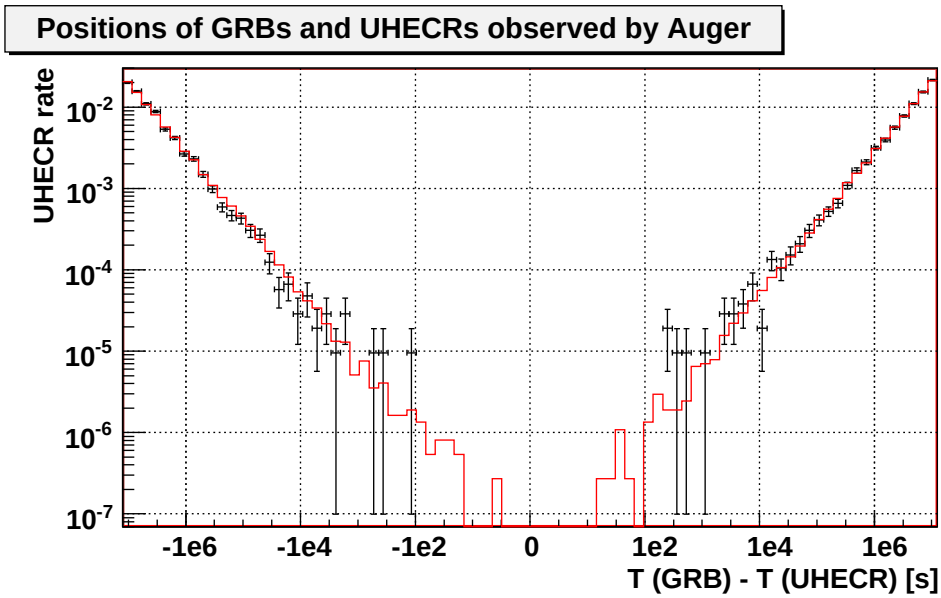

Figure 6.3: Rates of CR events as a function of the difference between the GRB time and the CR arrival time. Data falling within 30° of a GRB are indicated by red-lined histogram and within 5° by black points. For clarity, statistical errors are shown only for the 5°-distribution.

Soft gamma repeaters (SGR) are high energy sources that emit large burst of γ-rays at irregular time intervals. Their bursts have typical durations of the order of a few hundred milliseconds and are emitted during sporadic active periods that can last from weeks to months.

The proposed model is that of a magnetar, i.e. a neutron star with a huge magnetic field, $\vec{B} \sim 10^{15}$ G, located in our Galaxy. The origin of the flare can be explained as global crustal fractures due to $\vec{B}$-field rearrangements liberating a high flux of X-rays and γ-rays [Tho95]. The exceptional energetics of this hyper-flare makes SGR 1806-20 an attractive candidate source of UHECRs, high energy neutrinos, and gravitational waves [Iok05]. Assuming that the source lies in our Galaxy and it was able to generate high-energy neutrons then a significant fraction of these neutrons could arrive at Earth before decaying. Searches for neutrino and gravitational wave emission have been reported by the AMANDA [Ach06], AURIGA [Bag05], and LIGO scientific [Abbo07] collaborations. In all these searches the data revealed no significant signal.

The flare constitutes potential candidate for the acceleration of UHECRs. Secondary neutrons can be produced in collisions of relativistic protons (and nuclei) with the ambient plasma. Interestingly, those produced with an energy $E > 10^{18}$ eV have a boosted $c\tau_n$ sufficiently large to serve as Galactic messengers. The mean decay path of the neutron is $c\Gamma_n\overline{\tau}_n = 9.15(E/10^{18}\text{ eV})$ kpc and the lifetime is boosted from its rest frame value $\overline{\tau}_n = 886$ s to its lab value by the factor $\Gamma_n = E/m_n$. Because of the exponential depletion, about 20% of the neutrons survive the distance to the Earth at 10^{18} eV, and about 58% at $10^{18.5}$ eV.

SGR 1806-20 is located about 14.5 ± 1.4 kpc from the Earth [Cor97]. The

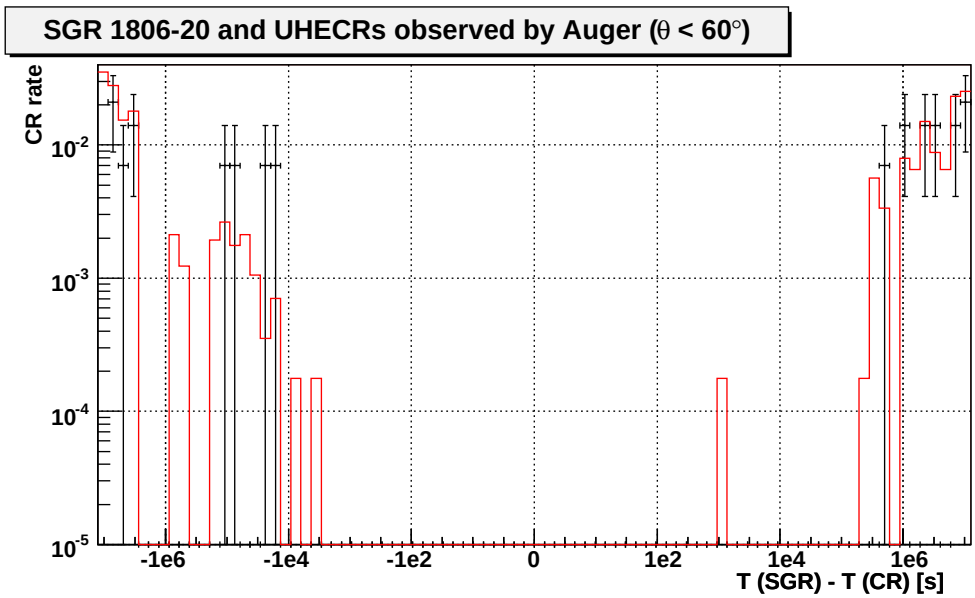

Figure 6.4: Rates of CR events from the direction of SGR 1806-20 as a function of the γ-CR time difference. Conventions are the same as in Fig. 6.3.

location of the source, right ascension 18h 08m 39.34s and declination $-20^\circ\ 24'\ 39.7''$, is within the FOV of the Pierre Auger Observatory. The source is below zenith angle $\theta = 60^\circ$ for about 9 hours per day. During the time of flaring emission 21:30:26.5 UTC the zenith angle of the object was $\theta_{\rm SGR} = 70.3^\circ$, and it remained for next 50 minutes above the horizon. Unfortunately, this is outside the currently best understood region of the detector, i.e. $\theta_{\rm max} = 60^\circ$.

The analysis described in the previous section was repeated for this exceptional burst. The results of the analysis are shown in Fig. 6.4, indicating that as in the case of GRBs no significant excess in the CR flux is evident after the burst. (The number of events coming from the direction of SGR 1806-20 within a 30° cone is $\mathcal{N}_{30^\circ} = 5,596$ whereas for 5°, $\mathcal{N}_{5^\circ} = 139$.)

By extending our data analysis to higher zenith angles it has been verified that no events have been observed within 5° cone during the $T = 300$ s of the flare, where $\theta_{\rm SGR} \approx 70^\circ$. The absence of the signal can be used to place an upper bound on the primary neutron flux, without assumptions on the Galactic magnetic field. To do so, the effective detection area A and the trigger efficiency $\epsilon(E)$ must be determined. We adopt the elementary hexagonal cell approach discussed in Ref. [All05]. On December 27th, 2004 an average of 364 hexagons were fully active, each corresponding to 1.95 km^2 on the ground (which amounts to 0.66 km^2 as seen with the zenith angle of $\approx 70^\circ$). Hence, the experiment represents target area A of 239 km^2 for the potential beam of neutrons coming from the source. The trigger efficiency for 70° is shown in Fig. 6.5.

Using the diffuse flux of cosmic rays we estimate a background $\ll 1$, thus Poisson statistics implies an upper bound of 3.09 events at 95% CL from neutron fluxes,

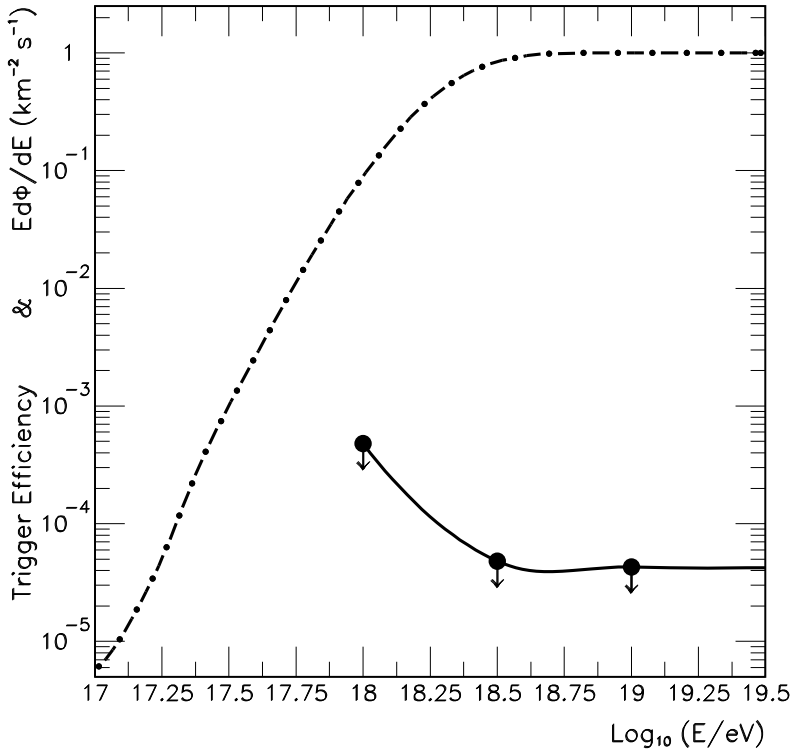

Figure 6.5: The rising dot-dashed line indicates the trigger efficiency of Auger for $\theta = 70°$. The arrowed circles indicate upper limits on the energy weighted flux of neutrons from SGR 1806-20 (valid in a logarithmic interval $\Delta = 1$). From [Anc07].

$d\Phi/dE$ [Fel98]. Equivalently, for an energy interval Δ,

$$T\ A \int_{\Delta} dE\ \frac{d\Phi}{dE}\,\epsilon(E) < 3.09\ . \tag{6.3}$$

In a logarithmic interval Δ where a single power law approximation (for the integrand) is valid, we obtain

$$E_0\ \frac{d\Phi}{dE}\bigg|_{E_0} < \frac{3.09}{T\ A\ \epsilon(E_0)}\ , \tag{6.4}$$

where E_0 is the energy at the center of the logarithmic interval taken as $\Delta = 1$. The 95%CL upper limits on the energy weighted flux of neutrons are shown in Fig. 6.5.

Chapter 7

Fluorescence Detector Performance

The fluorescence detector consists of 24 telescopes located in four buildings on the perimeter of the area covered by water tanks. The telescopes observe tracks of cosmic ray showers which are visible due to the nitrogen fluorescence. Nitrogen nuclei are ionized by many charged secondary particles borned in the atmosphere and carrying the large fraction of primary particle energy.

All fluorescence sites have been completed and are in operation. Los Leones has been in full operation since March 2004 and Coihueco since July 2004. Los Morados began its data acquisition in April 2005, and the fourth site at Loma Amarilla started its operation in February 2007.

The operation of the fluorescence detector is not fully robotized and an attendance of a shift crew is necessary. Since the first days of FD observation a presence of at least four people has been required. The responsibilities of the shift crew consist of several activities before, during and after each night. As examples it can be mentioned the relative calibration of cameras and optical components before and after observation, the starting and stopping data taking in relation with actual weather conditions and a prompt correction of some software or hardware problems.

The procedure of FD operation is still evolving and the introduction of new software transfers the responsibility of the human crew to a robotic operation. The final aim tends to take over the operation of FD telescopes into as much robotic and remotely controlled mode as possible.

We will present calculation of uptime/downtime for all FD telescopes till the end of year 2008. These results are essential for the calculation of cosmic-ray hybrid spectra measured at the Pierre Auger Observatory. Morevover, these calculations provides an effective offline control of fluorescence detector as well as lidar's performance.

7.1 Downtime

Typical data taking period of the fluorescence telescopes consists of astronomical nights (the position of the Sun is at least 18° below the horizon) during which the

illuminated size of the Moon is equal or less than 60%. One observational period typically consists of 16 days with average observational time of 10 hours (which ranges from 14 hours in June to 5 hours in December).

Everything that prevents the FD measurement to be as long as the astronomical night is considered as the downtime, except for the time period with Moon's position closer than 5 degrees to a field of view (FOV) of a particular telescope. We do not include the later time interval into downtime, because the actual sky position of the Moon can be calculated in advance and the data taking time can be optimized to it for each individual telescope. The main sources of downtime are bad weather (thunderstorms, windstorms, snowfalls etc.), power cuts (which are caused very often due to the thunderstorms during the austral summer) and high level of the night-sky background light (caused in particular by scattered moonlight). Also the operation of lidars and hardware or software problems interrupted the FD operation several times.

The stability of the fluorescence observation should be checked. It can be monitored as the ratio of real and expected uptime of fluorescence detector. This ratio is depicted in Fig. 7.1 for each observation period. The expected uptime is the sum of the length of astronomical nights during observation period for each telescope. It must be corrected for the moments when the Moon is closer than 5 degrees to telescope's FOV. The real uptime is calculated directly from the measured data. The constant value of the ratio indicates troublefree observation periods.

The ratio shows large scattering due to various conditions during the observation periods. There is a clear reason, why the ratio does not reach the value of 1.0. The reason is linked to the downtime caused by the Moon. The Moon as the brightest source of the night sky is the main origin of too high background light (see Section 8.2). If the brightness of the sky is too high, only the brightest air showers can be observed and therefore the rate of air-shower events decreases rapidly. Moreover the illumination of the photomultipliers (PMTs) placed on cameras is too high, which increases the degradation of PMT's sensitivity. Therefore the observation is suspended if the scattered moonlight is the main cause of high level of the background light. Such cases occur typically during the first and the last three or four nights of each observation period, when the phase of the Moon is around the Last and the First Quarter. Naturally the Moon has to be above (or slightly below) the horizon, which lasts approximately one third of a night. The above mentioned conditions can be expressed numerically:

$$T_{bright} \sim \frac{(4+4)\text{ days}}{16\text{ days}} \left(\frac{1}{3}\right) T_{th} = \frac{1}{6}\, T_{th} \sim 0.2\, T_{th}, \tag{7.1}$$

where T_{bright} is period with too bright night sky (for more details see Chapter 8) and T_{th} is theoretically calculated uptime from the motion of the Moon and the Sun. We can see that the difference of 0.2 in Fig. 7.1 can be attributed to the influence of the Moon. All decreases below the value of 0.8 reflect the presence of other kind of problems with the apparatus (power cuts, bad weather conditions, hardware failures etc.).

The decrease of the average value of the ratio since the second half of year 2007 (in

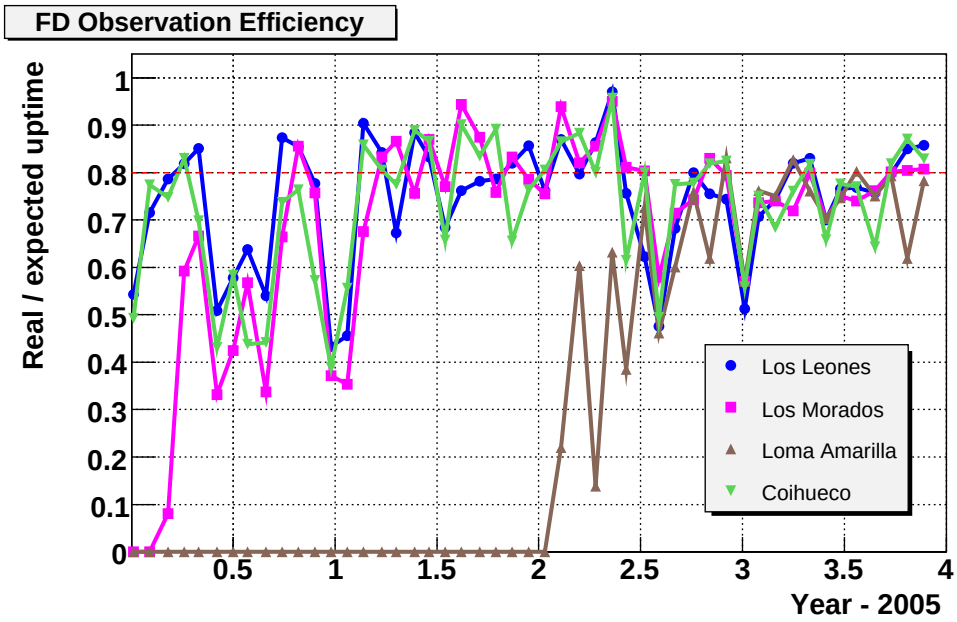

Figure 7.1: Ratio of real and expected uptime (calculated from motion of sun and moon) of FD.

comparison with the previous year) was caused by the limitation of FD measurement to the nights with not too bright night sky as is discussed in Section 8.3.

7.2 Uptime

The uptime is the sum of time intervals when a fluorescence telescope had been successfully operating in such a way, that data from this telescope can be used for physics analysis (e.g. the calculation of the hybrid spectrum). Several methods of uptime calculation have been developed, which differ in the amount of analysed data.

Here a simple method based on the analysis of two measured quantities stored separately in the central database will be described. The first group of data files - called run files - stores the information about observed events and about the status of a telescope. The second group of files - called bgloops - collect analog-to-digital converter (ADC) variances, hitrates and other parameters for each PMT.

In the analysis we pick up the events from the run file and calculate time period between the first and the last detected third level trigger (T3) event. A presence of a telescope in data acquisition (DAQ) is checked for each event. To filter out the cases, when shutters were closed during DAQ, the data from the run file are checked with corresponding bgloop data. Average ADC variances on the camera must lie between 8 and 1000 (ADC counts)^2 if the shutters were open and no electronic problem occurred. The lower value is well above basic noise of each PMT (which lies typically in the interval between 3 and 5 (ADC counts)^2). A few cases with ADC variance slightly below this level when the shutters were opened has been found, but because of their rareness such intervals did not affect the calculation of the uptime

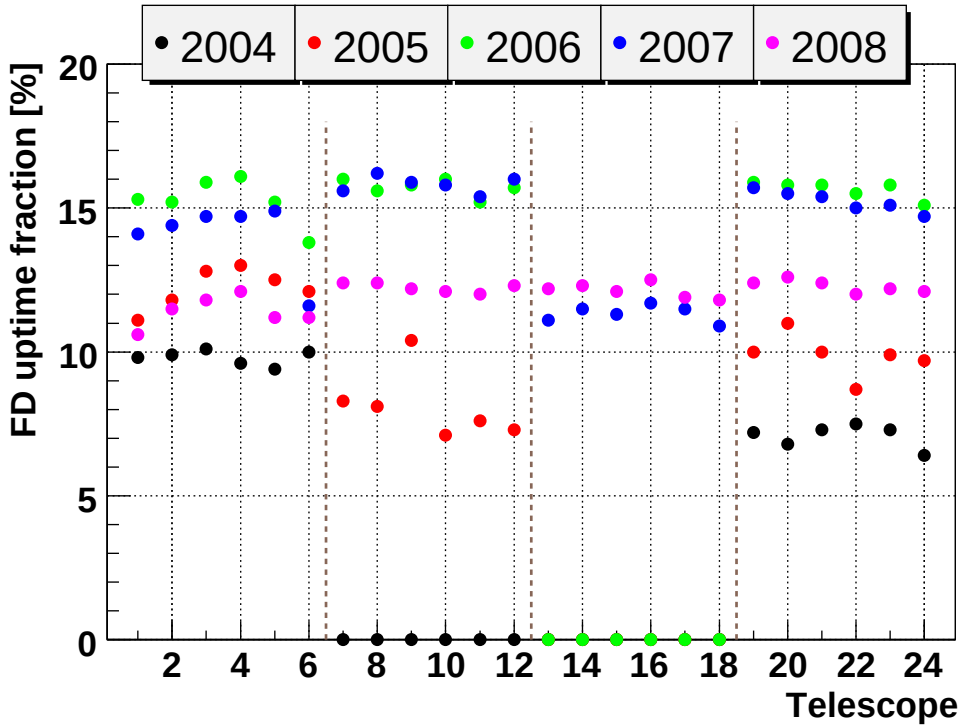

Figure 7.2: Yearly FD uptime for all 24 telescopes.

and can be neglected.

The calculated uptime fraction for all 24 telescopes is shown in Tab. 7.1 for the whole period of fluorescence observation. Yearly uptimes are depicted in Fig. 7.2. It is worth to mention, that the values are significantly higher than 10% during last years for routinely operating telescopes during at least one year. The uptime fraction of 10% is the value frequently referenced in the literature. For further data analysis other quality cuts are applied and thus the uptime values decrease down by about 1 or 2%.

The long time problems in the performance of fluorescence telescopes can be identified. Let's mention problems with fire-wire connection between detector's components during year 2005. The telescopes at Loma Amarilla on the other hand had suffered from frequent difficulties with the operation of gas generator in 2007. As typical examples of long-term hardware problems can be also mentioned light-leaking in the telescope 6 at Los Leones since April to May 2006 and non-working hardware component in the telescope 4 at Loma Amarilla between March and June 2008.

7.3 Veto Time

The important component of the fluorescence detector's atmospheric monitoring system is a set of four elastic backscatter lidar stations [Ben07]. Every FD build-

ing is equipped with one lidar station. During each hour of FD data taking, the lidars perform routine scans of the sky over each FD. These data provide important information about the properties of the atmosphere. In addition to this routine operation, the lidar system is used for real time monitoring of the atmospheric homogeneity between the fluorescence telescopes and selected cosmic-ray showers. This procedure is called shoot-the-shower, and could be used for a rejection of showers where the light profile from the track is distorted by clouds (important among others for photon-candidate showers) or by other aerosol non-uniformities that are not sufficiently characterized by the average hourly aerosol measurements.

Some shooting positions can be very close to or even inside the field of view of the FD telescopes. In order to prevent the detection of a large number of spurious FD events generated by the lidar shooting activity, buffer zones have been delimited around the FD fields of view. Every time the laser is fired inside this buffer zone, the FD DAQ is inhibited in order to avoid any interference. This is accomplished by sending a veto signal from the lidar to the nearest FD when the laser is ready to fire.

Special attention was focused on veto time and the size of buffer zones of the lidars. Each event observed by FD contains the information about downtime caused by the readout of electronics for each detected event and also by total veto time. The analysis of measured data give the total FD downtime (the sum of veto and readout time) introduced by all lidar operations. The fraction of veto time is typically at least one order of a magnitude higher than downtime produced by the readout of electronics.

The results were obtained for three FD buildings: Fig. 7.3 for Los Leones, Fig. 7.4 for Los Morados and Fig. 7.6 for Coihueco. (No lidar worked at LA during the studied time interval.) The procedure is executed after every data taking period which allows the instantaneous inspection of the lidar's operation. As we can see in Tab. 7.2 the fraction of downtime caused by lidar's veto was successfully decreased to less than 1% by the restriction putted on their operation, particularly in the buffer zones, in September 2006. The most critical situation was at Los Leones site, where the position of the lidar stands at the boundary of the field of view of the first telescope (in other sites lidar's house is located behind the FD building).

The seasonal changes of the length of the astronomical nights can be clearly seen. The longest observation period are during the austral winter (i.e. during the middle of a year).

7.4 T3 rates

The software of implemented third level trigger (T3) algorithm selects shower candidates and performs the reconstruction of the shower geometry from the timing information of the pixels with signal. A large part of the background, which is due to individual secondary particles passing through the PMTs, is rejected [Abr04].

Observed T3 rates for FD runs longer than 10 minutes are shown in Fig 7.7, 7.8, 7.9 and 7.10. Red line corresponds to T3 rate equal to 0.06 Hz, which is considered as maximal value for troublefree measurements. T3 rate equals to 0.3 Hz is the

Table 7.1: Overall uptime for all 24 fluorescence telescopes for given GPS time (since T_{start} till T_{end}, i.e. December 2008).

Tel	LL	T_{start}, T_{end}	LM	T_{start}, T_{end}
1	11.1%	766890893, 912671480	12.9%	798939861, 912671664
2	11.5%	766890893, 912671480	12.8%	797903246, 912671664
3	11.3%	758182402, 912671480	13.2%	798939861, 912671664
4	11.5%	758182402, 912671480	12.4%	795152386, 912671664
5	11.1%	758182402, 912671480	12.2%	795152386, 912671664
6	10.1%	758599035, 912671480	12.5%	795152386, 912671664
Tel	LA	T_{start}, T_{end}	CO	T_{start}, T_{end}
1	11.6%	856227441, 912671316	11.8%	773464889, 912671498
2	11.9%	856229180, 912671316	10.9%	758182587, 912671498
3	11.8%	856227441, 912671316	10.7%	758182587, 912671498
4	9.2%	856229180, 912671316	11.2%	773464760, 912671498
5	12.0%	856229180, 912671316	11.6%	773464760, 912671498
6	11.4%	856227441, 912671316	11.4%	773546843, 912671498

expected maximal value for one fluorescence building with its 6 telescopes. If we suppose that one fifth of events is triggered by two telescopes, then T3 rate for one telescope becomes 0.3/5=0.06 Hz.

The values above this line indicate problematic runs, when spurious triggers could be caused by the lidars, lightnings etc. Also the opposite cases with too low T3 rate could be identified (most probably caused by clouds, but also by hardware difficulties). Thus one can identify for example the failure of the trigger part of electronics in telescope 4 at Loma Amarilla in the middle of 2008.

Seasonal fluctuations of T3 rates are also visible. They are not caused by the fluctuations of the flux of primary cosmic rays, but probably by the seasonal changes of atmosphere visibility.

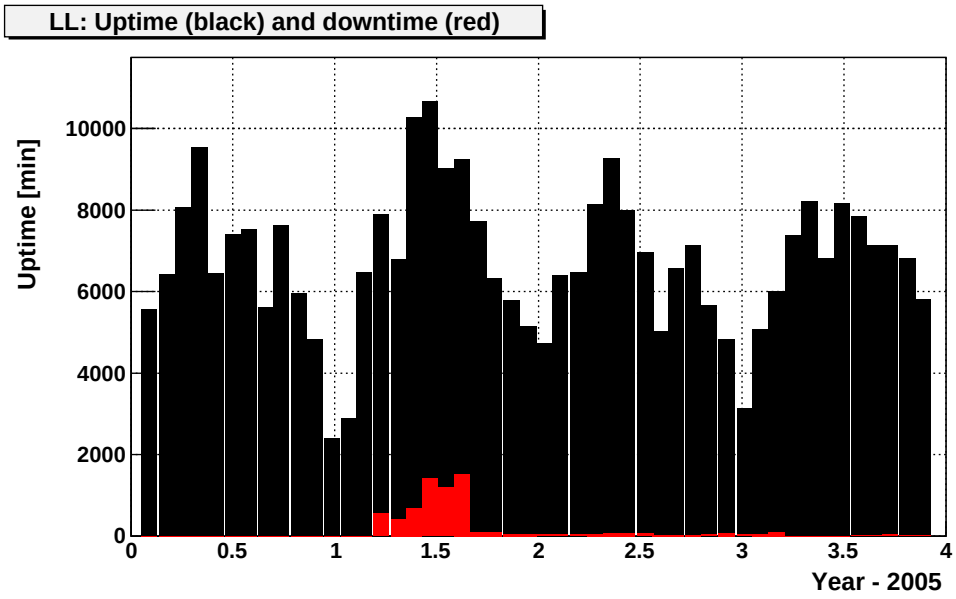

Figure 7.3: Uptime (black) and downtime caused by lidar's veto (red) for Los Leones since January 2005.

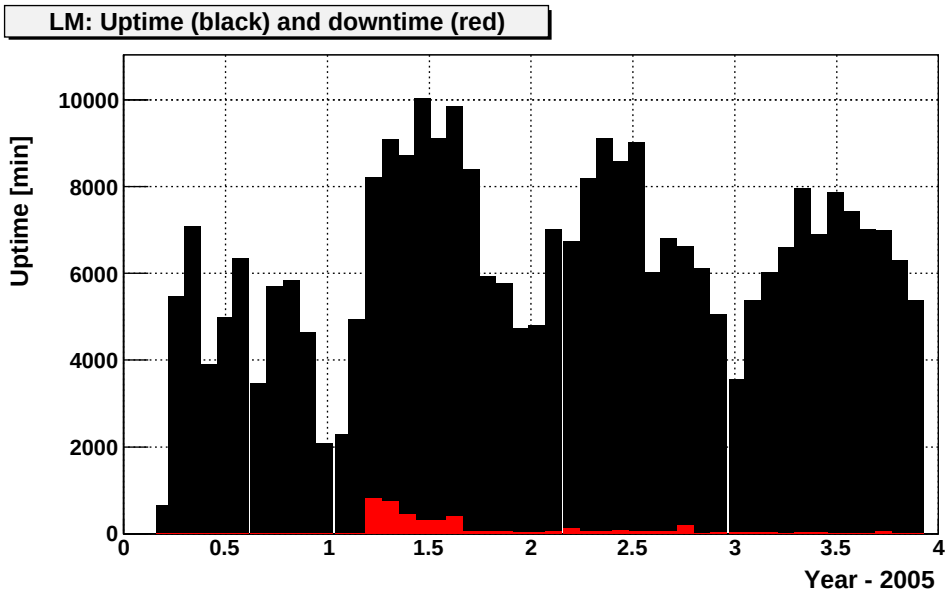

Figure 7.4: Uptime (black) and downtime caused by lidar's veto (red) for Los Morados since March 2005.

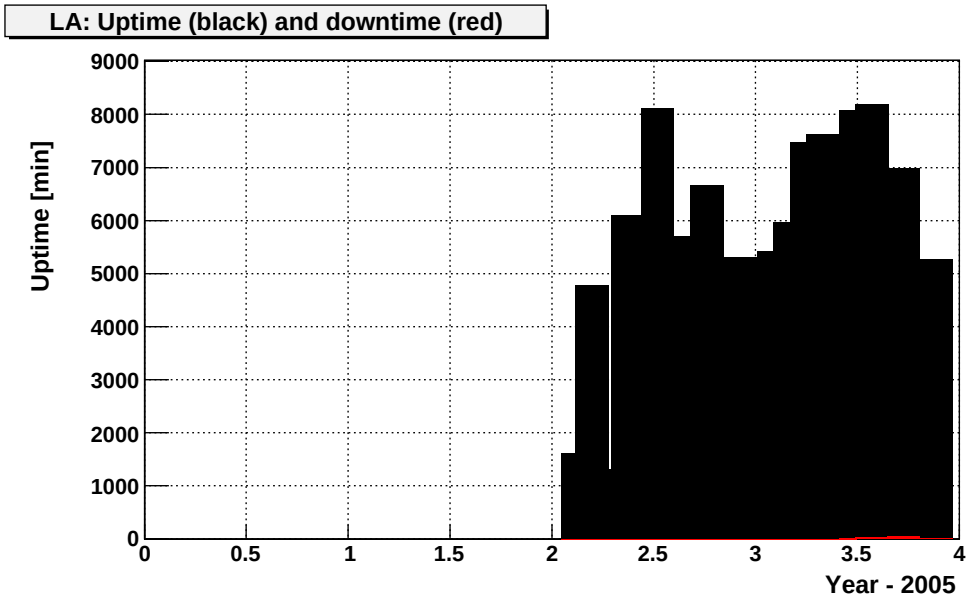

Figure 7.5: Uptime (black) and downtime caused by lidar's veto (red) for Loma Amarilla since February 2007.

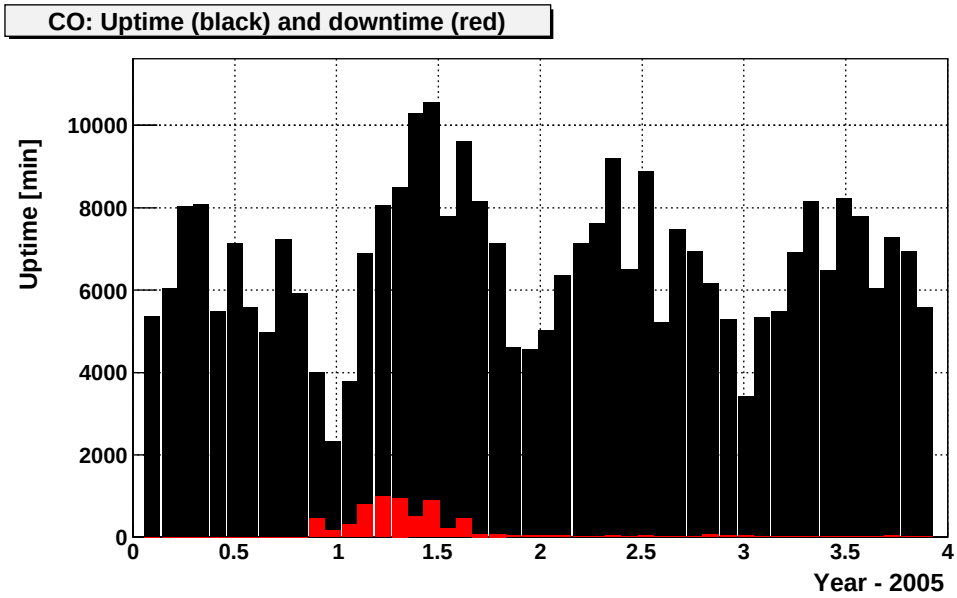

Figure 7.6: Uptime (black) and downtime caused by lidar's veto (red) for Coihueco since January 2005.

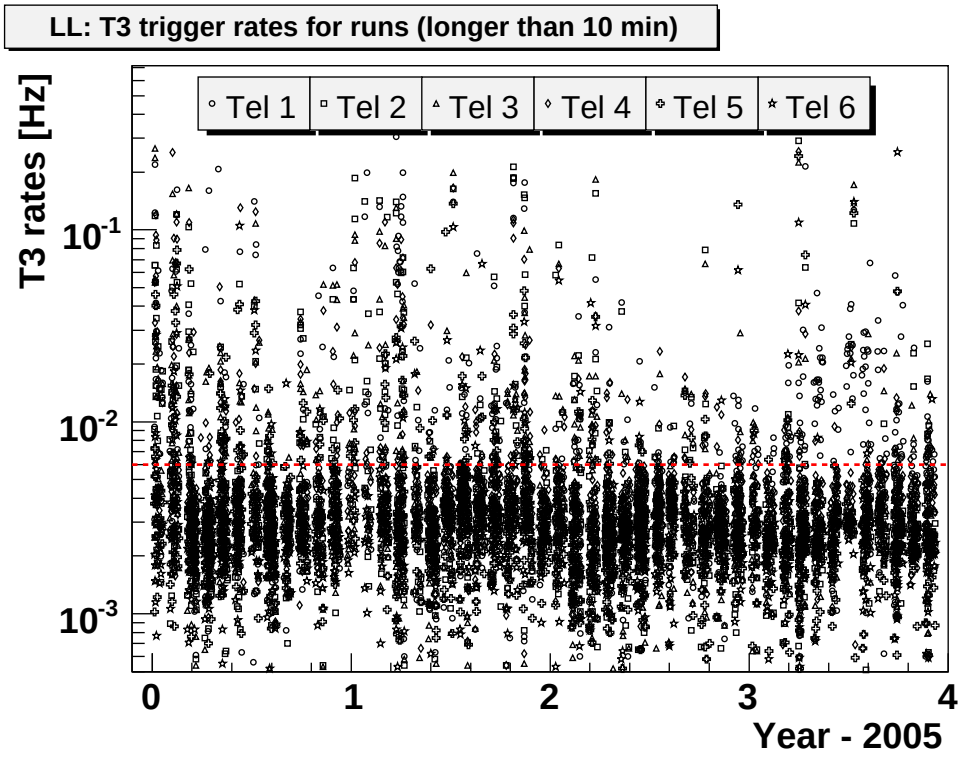

Figure 7.7: T3 rates for Los Leones.

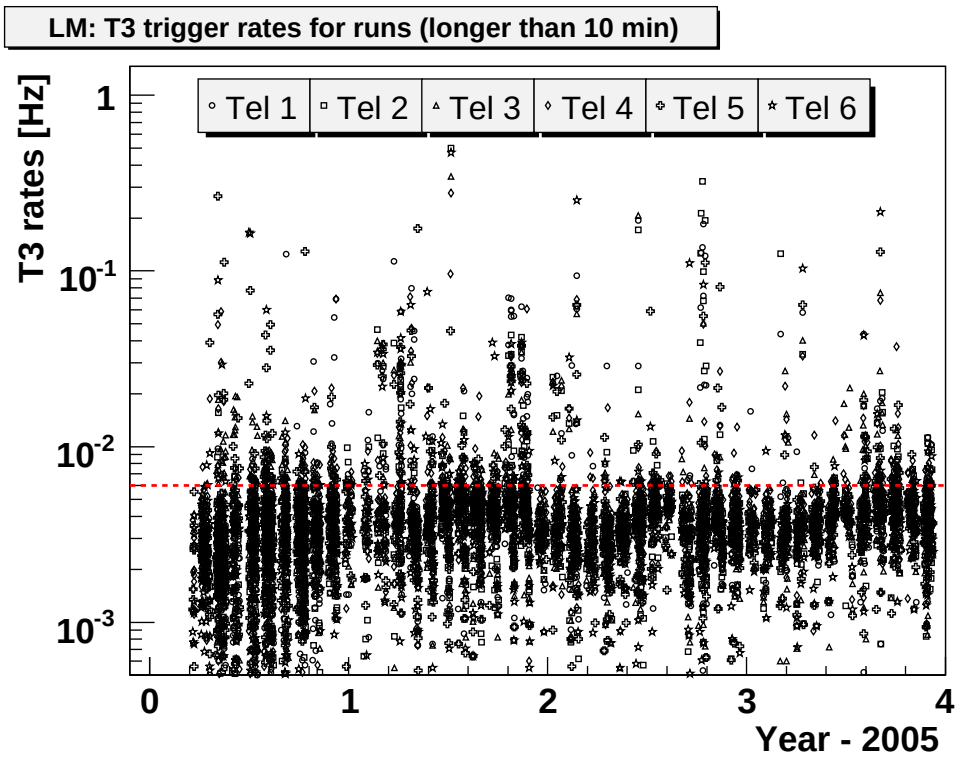

Figure 7.8: T3 rates for Los Morados.

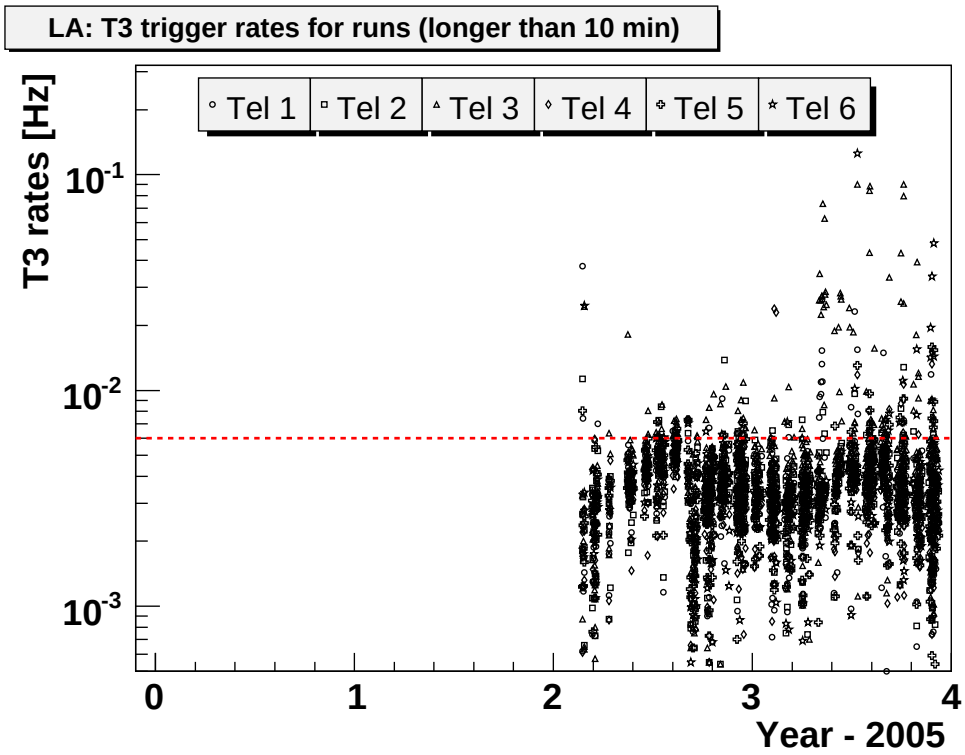

Figure 7.9: T3 rates for Loma Amarilla.

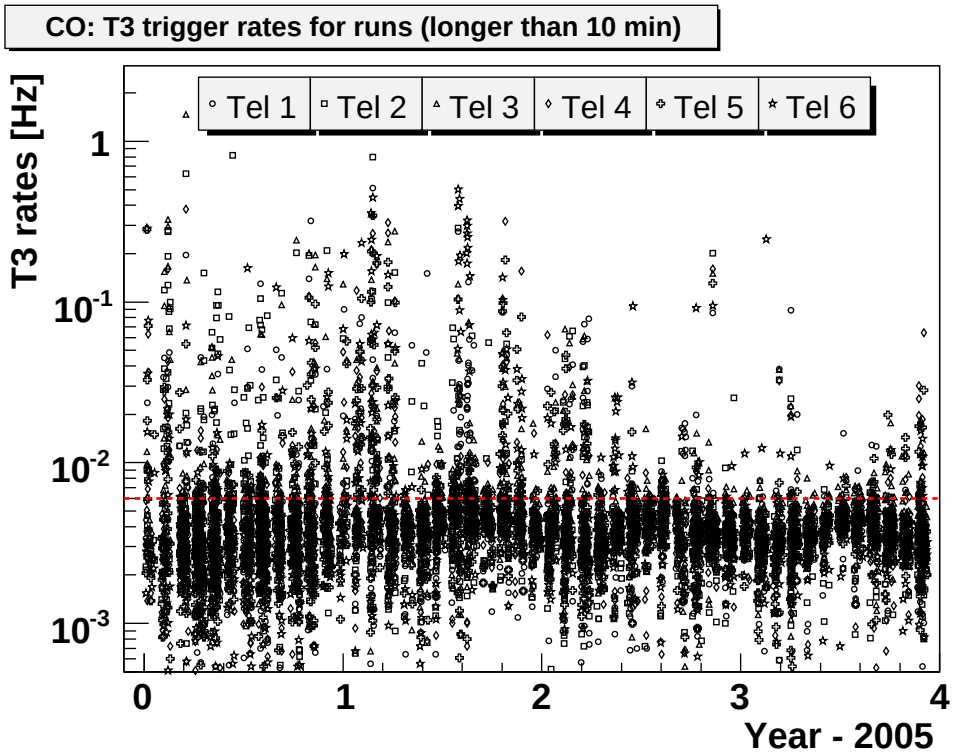

Figure 7.10: T3 rates for Coihueco.

Table 7.2: Veto time since Jan 2006 as a percentual fraction of FD uptime. Numbers in first row denote months. Lidar at Loma Amarilla (LA) was operated since June 2008.

Year	Eye	1	2	3	4	5	6	7	8	9	10	11	12
2006	LL	0.0	0.0	7.19	6.15	6.76	13.28	13.33	16.54	1.51	1.76	1.06	1.05
	LM	0.0	0.40	9.88	8.23	5.23	3.21	3.30	3.99	0.70	0.99	0.90	0.69
	LA												
	CO	8.20	11.56	12.32	11.17	4.96	8.41	2.73	4.80	1.01	1.13	0.97	0.80
2007	LL	0.91	0.78	0.78	0.64	0.95	0.96	1.04	0.68	0.47	0.41	0.73	1.93
	LM	0.83	0.68	1.72	0.63	0.69	0.75	0.61	0.96	0.82	2.81	0.10	0.69
	LA												
	CO	0.74	0.54	0.28	0.33	0.42	0.16	0.50	0.59	0.33	0.43	0.88	0.65
2008	LL	1.48	1.13	1.69	0.0	0.0	0.0	0.17	0.24	0.30	0.68	0.31	0.34
	LM	1.13	0.56	0.43	0.31	0.31	0.41	0.24	0.19	0.26	0.62	0.13	0.18
	LA							0.14	0.26	0.37	0.73	0.28	0.32
	CO	0.94	0.20	0.22	0.24	0.21	0.20	0.25	0.23	0.28	0.63	0.22	0.24

Chapter 8

Variances of ADC Signal

Photomultipliers (PMTs) placed on cameras record background lights of the night sky in addition to the measurement triggered by short pulses initiated by cosmic-ray showers. Background light is not measured directly, because PMT's cathodes are grounded and therefore static component of anode current (which is proportional to background light) is removed. An alternative method to measure night-sky background light based on the statistical analysis of ADC (analog-to-digital converter) counts is used. As was described in [Kle03] there is a direct relation between the variances of the signal and its average. Therefore the variance of measured signal is proportional to an incoming photon flux. Variances of ADC signal come every 6.5 ms from values recorded during 100 ns integration periods and are stored into bgloop files every 30 seconds.

The measurement of ADC variances is particularly important for long-time control of the level of the sky background light and the protection of the PMTs against light excess of artificial or natural origin (i.e. Sun, Moon). It can be further used for the tracking of UV-bright stars across a camera. This has been used to estimate the exact pointing of the telescopes and for the calculation of light exposure of the PMT (which is essential for estimation of total anode charge accumulated on the anode). The optimal trigger conditions also depend on the light level at each pixel.

The night-sky brightness originates from sources both outside and within the Earth's atmosphere. Zodiacal light, light reflected from interstellar dust and the integrated brightness of faint stars and galaxies are the main extraterrestrial components, in descending order of brightness. Within the atmosphere, the most of sky brightness is due to airglow emissions in the atmospheric layer around the altitude of 130 km, the so-called van Rhijn layer [vRh21]. This is caused nightly by recombination of atoms and molecules in the upper atmosphere following ionization by ultraviolet solar radiation during the day. For more details see [New06].

The sky brightness can dramatically change also during clear and moonless nights and therefore its value is regularly monitored already during FD measurement. The night-sky brightness defines the proper conditions for FD measurement as will be discussed later. In addition its value strongly affects the range of the visibility of fluorescence telescopes and the actual value must be considered further in physical analysis. The finding of the suitable value of maximum value of night-sky brightness

for fluorescence detector measurement is presented here. Also the illumination of sensitive photomultipliers with extremely high night-sky brightness and its influence on the detector performance are described.

8.1 Typical ADC Variances

Total fluctuations of ADC signal are directly proportional to the sum of an electronic noise background and a sky background. When high voltage on a telescope camera is turned on at night and the shutters are closed, the level of the electronic noise lies between 3 and 5 (ADC counts)^2.

The night conditions can be divided into a few classes according to the level of the background light level measured by fluorescence telescopes. The lowest ADC variances are observed for nights with sky covered by clouds. The measured ADC variances lie between 8 and 20 (ADC counts)^2. The former number has been observed for the whole sky covered by heavy clouds and the later for the sky covered by scattered clouds.

On the contrary the highest observed night-sky background occurs typically during a few nights after the start of and before the end of the observation period, when the Moon is above the horizon and is close to one of its quarter phases. The scattered moonlight could increase ADC variances to the level of a few hundredths. Such conditions are not suitable for the observation of extensive air showers by fluorescence telescopes. These nights can be dangerous for the PMTs and the FD operation is no longer possible for such a bright sky. The fraction of FD observations above the highest allowed value for FD observation - equal to 100 (ADC counts)^2 - is typically less than 5% for the whole period of telescope's observation since 2004 till the end of 2007, see Fig. 8.1. The cut on maximal value of ADC variances for FD has been applied in January 2007 and from that time the fraction decreases.

The optimal background conditions for fluorescence observation range from 20 to 60 (ADC counts)^2, which are typical for the nights with clear sky and without moonlight. The clear moonless sky will be defined by the above conditions for ADc variances in our further analyses.

8.2 Phases of Moon

The level of ADC variances depends strongly on the illuminated size of the Moon. The measured ADC variances for different phases of the Moon are shown in Fig. 8.2. The phase of the New Moon was defined as 0.5 in the Figure.

FD observation period starts during the first night when the crescent Moon fraction area is less than 60%. For this night the Moon rises above the horizon during the second half of the night. Because of the moonset before the midnight during the last night of FD observation period, the FD measurement could continue even for the nights with the Moon phase larger than 60%.

Typical ADC variances during 16 days of FD shift illustrates Fig. 8.3. Data were measured by the telescope 3 at Coihueco during May 2006. The high values of ADC

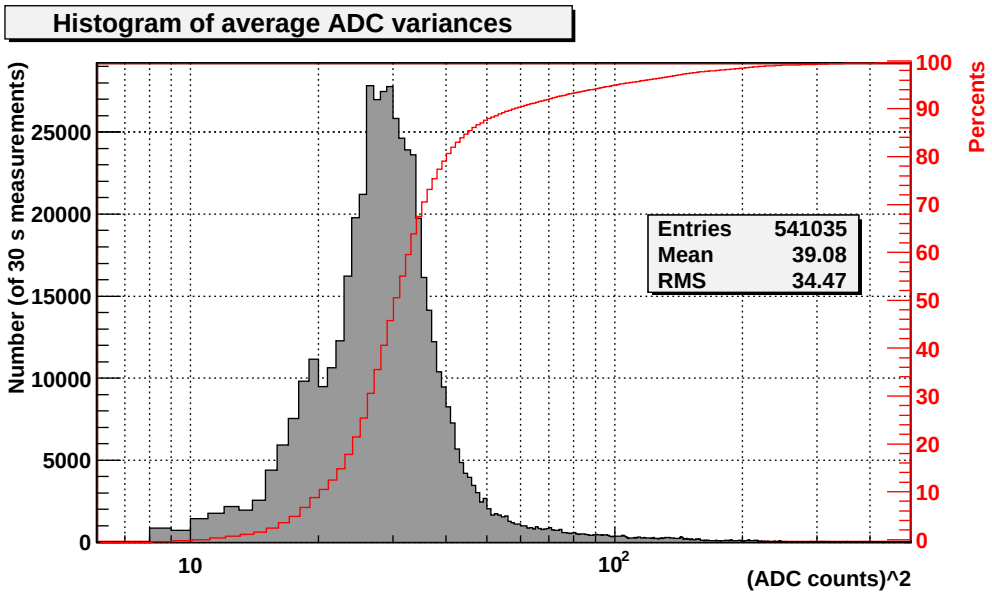

Figure 8.1: Example of ADC variances averaged over camera 3 at Coihueco. Red line shows cumulative distribution of values in histogram.

variances during the first and the last three nights caused by the Moon are clearly visible.

The dependence of two basic parameters of reconstructed air showers on the phases of the Moon was checked. No dependence of the shower distance (Fig. 8.4) and the energy of the primary particle (Fig. 8.5) on the illuminated fraction of the Moon was registered.

8.3 Maximum Value of ADC Variances

The measurement of background light shows clear connection with the phase of the Moon, see Fig. 8.2. The highest level of ADC variances are during a few first and last nights of FD observation period, when the Moon is close to its quarter phase. Since the first days of FD measurement the maximum value of night-sky brightness (measured in (ADC counts)^2) was established to protect sensitive PMTs. The value of (200 ADC counts)^2 had been determined as a suitable maximum. .

Because of the lack of an automatic control of FD operation, the above given value was from time to time overreached. Later the rapid degradation of PMT's sensitivity was found by the callibration measurements. It was not clear if this degradation had been caused by the illumination of PMTs by bright night sky, but one can suppose significant influence of high long-term photon flux level on PMTs. More details on this subject are given in Chapter 9.

The analysis of ADC variations presented in this work led to the restriction of FD measurement below the level of (100 ADC counts)^2. This restriction was successfully implemented during the second half of year 2007. There has been observed no significant influence on FD uptime (see Fig. 7.1) or on the trigger rate of measured

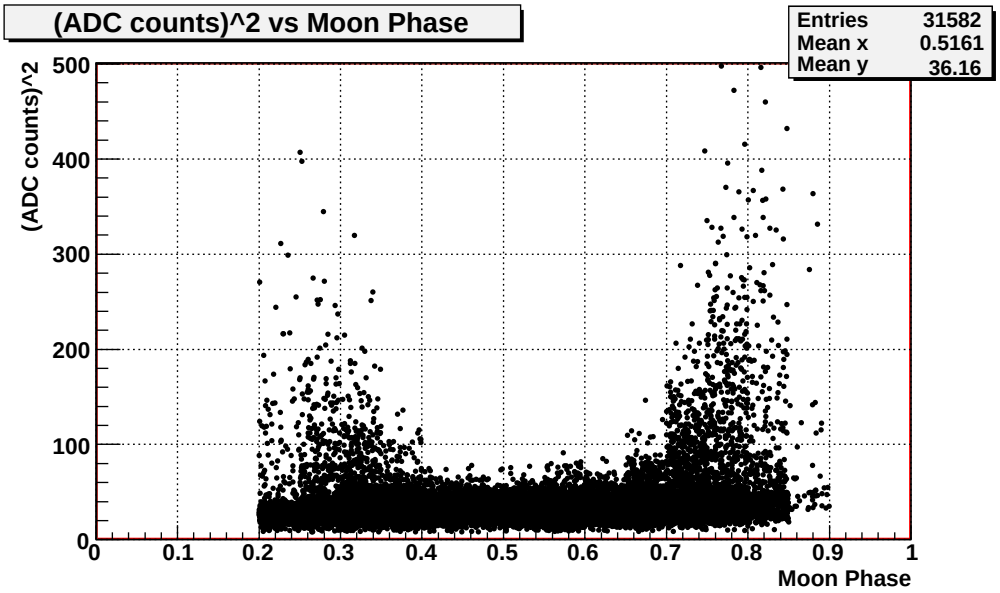

Figure 8.2: Measured ADC variances as function of Moon's phase.

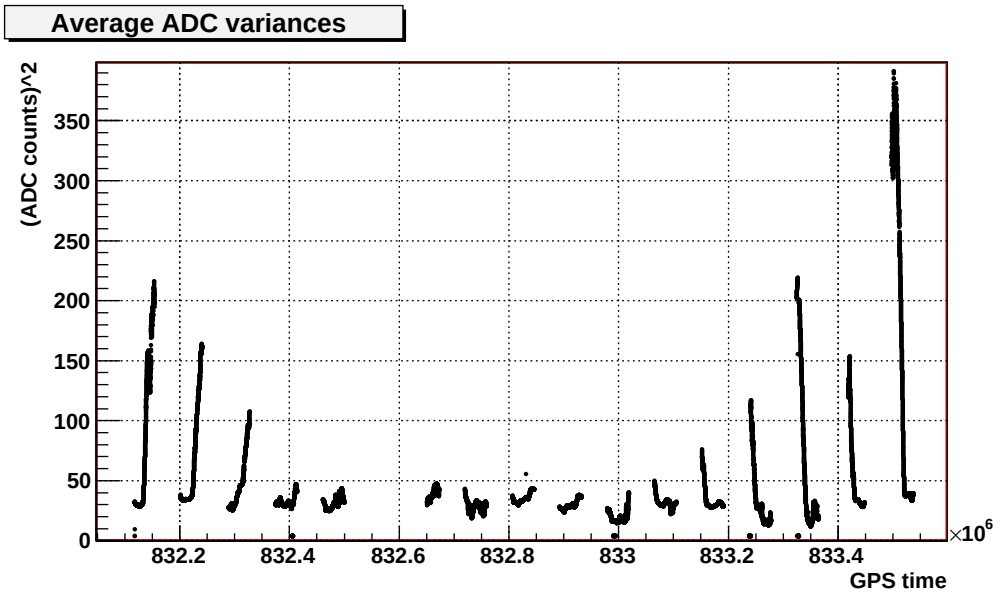

Figure 8.3: ADC variances on camera 3 at Coihueco during May 2006.

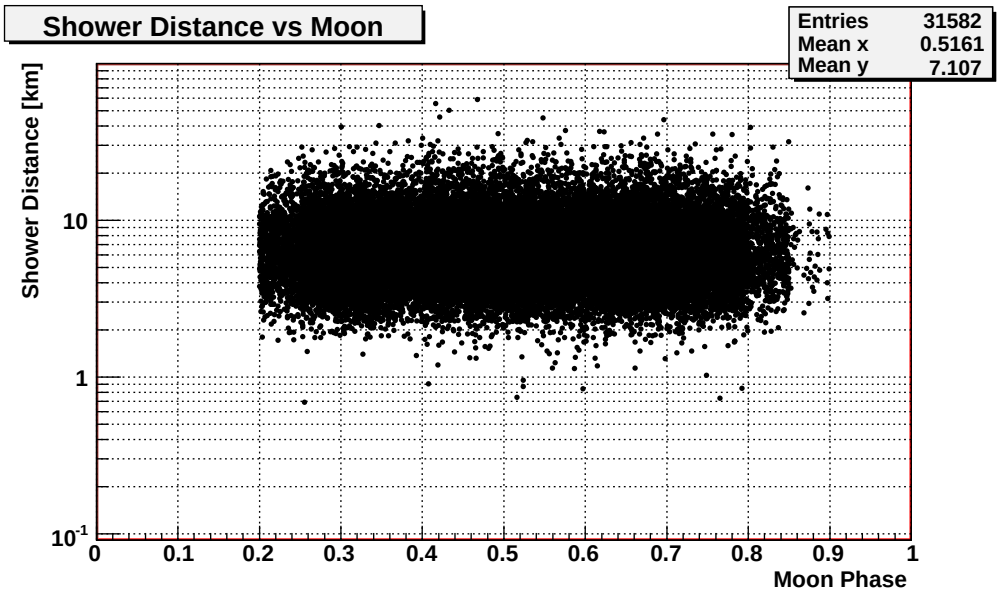

Figure 8.4: Shower distance as function of Moon's phase.

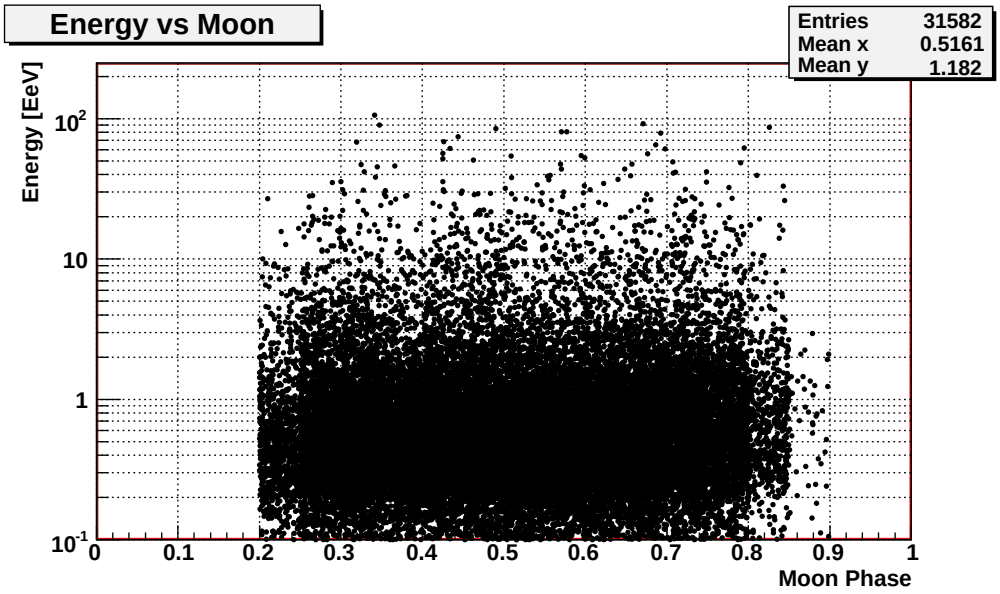

Figure 8.5: Energy as function of Moon's phase.

most energetic cosmic rays (see Section 8.7 and 8.9). Moreover, recent callibration results indicate the reduction of the degradation of PMT's sensitivity.

8.4 Average ADC Variances

ADC variances averaged over the FD observation periods could be extensively used also for another analysis. Here some of the long-time trends of measured ADC variances will be presented. These data can be among other used for checking the dates of corrector rings' installation in particular telescopes.

The first step was the selection of data. All of the measurements when the shutters stayed closed and problems occurred were removed. Hereafter only clear moonless nights have been selected by adopting the cuts on ADC variances, i.e. only time intervals with data between 20 and 60 $(\text{ADC counts})^2$ passed.

Long-time behaviour of ADC variances averaged over cameras is depicted in Fig. 8.6. The results are based on the analysis of all fluorescence telescopes, except for the telescope 6 at Los Leones and telescope 1 at Coihueco because they are affected by the light pollution coming from the city of Malargüe.

Data starts in February 2006, when the last corrector ring was installed at Coihueco. In such a way the observation interval without corrector rings and also the first FD observation periods suffering from unstable hardware/software conditions were filtered out. The last point belongs to FD observation period started in May 2008. As we can see in Fig. 8.6 ADC variations averaged over FD observation periods do not show clear seasonal dependence.

The linear fit shows constant value during the whole period. Previously indicated decrease of measured signal with a slope of 1.5 $(\text{ADC counts})^2$/year, i.e. 4.5% per year, was not confirmed by the observations in 2008. Such tendency, if confirmed, could be caused by the aging of PMTs or maybe by the variation of the solar activity. Additional measurements and further analysis are necessary to make any conclusion about the time evolution of night sky brightness. The analysis of an extensive set of cloudless nights based on the results from cloud cameras and lidars will be very important.

8.5 Installation of Corrector Rings

The installation of corrector rings into apertures of FD telescopes was made during different stages of building constructions. Some discrepancies were found between documented dates of corrector ring installation and those found in measured background data.

The installation of corrector ring would lead into outstanding increase of light flux illuminating a camera and therefore it would be easily identified in ADC variances. The increase can be simply calculated from the increase of the aperture of a telescope from the diameter of 1.7 m to 2.2 m. Only at Loma Amarilla the corrector rings were mounted already before the startup of telescopes.

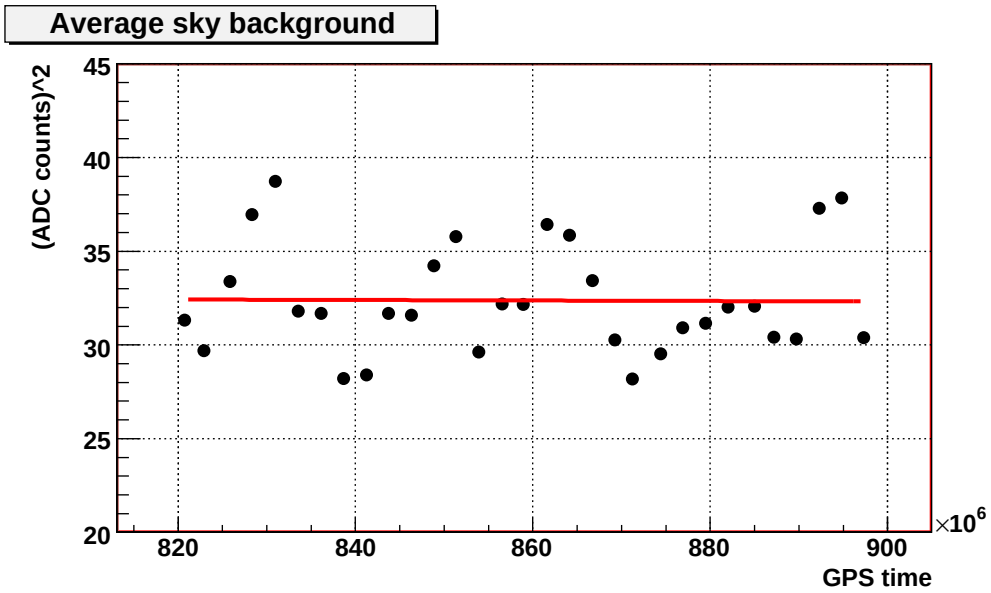

Figure 8.6: ADC variances averaged over telescopes and FD shifts since the last complete installation of corrector rings (January 2006). Data from LL6 and CO1 were not used. Line shows linear fit of points.

The observed ADC variances averaged over FD observation periods show very large spread and no clear increase of light flux was found after the installation of corrector rings in some telescopes. Only six telescopes from 18 show significant increase of the observed light flux close to the documented time of the corrector ring installation, i.e. telescopes 2, 5, 6 at LL and telescopes 1, 5, 6 at Coihueco. See for example Fig. 8.7.

In addition the measured increase of the measured light background for selected telescopes was lower than the value given by geometrical calculations [Car04]. The observed factor equals to 1.4 instead of 1.66.

8.6 Catalogue of Cosmic-Ray Showers

The "Observer" catalogue of hybrid data [Obs] measured by the Pierre Auger Observatory was used in further presented analyses. Standard cuts were applied to select the reconstructed events. These are following: the reconstruction level (a set of several quality criteria) equals to 10, the error of the reconstructed energy smaller than 20% and the shower maximum visible by the fluorescence telescope and reconstructed with the error less than 40 g/cm^2.

The catalogue of reconstructed hybrid events (i.e. those with a signal from at least one active water Čerenkov tank) do not include all fluorescence data. Hybrid and fluorescence data may not overlap particularly at the lowest energies because of differences in SD and FD trigger efficiencies.

The showers were selected till the end of year 2006, when the maximum allowed ADC variances was changed from 200 to 100 (ADC counts)^2 (see Section 8.3). Alto-

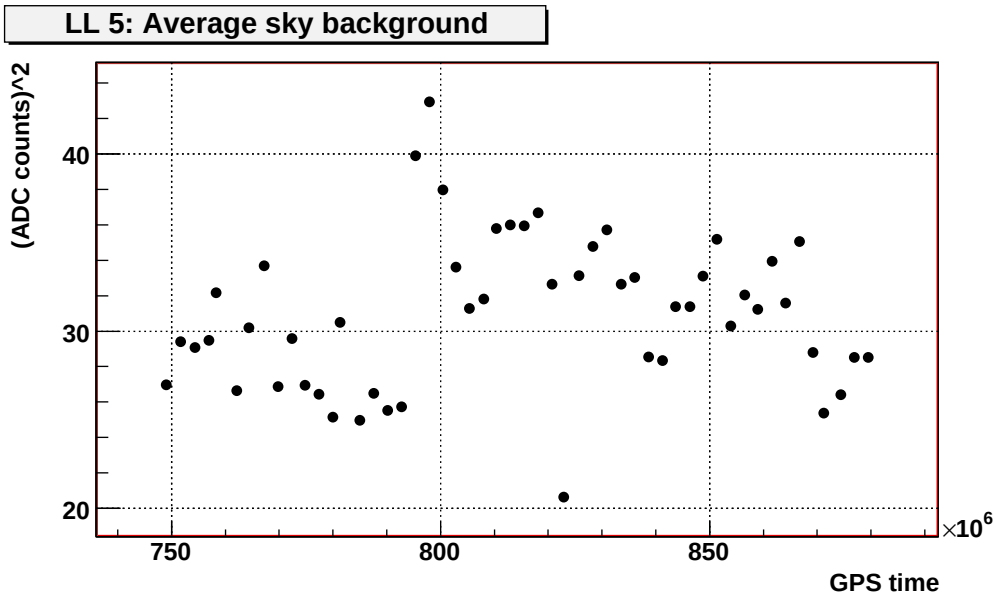

Figure 8.7: Increase of light background at Los Leones telescope 5 after installation of corrector rings in February 2005 (GPS time 791350000).

gether there were more than 30,000 reconstructed showers in the Observer catalogue till the end of year 2006.

8.7 Shower Distance and Energy

The extensive air showers are observed during variable sky conditions. Thus the FD measurement for different background light conditions must be studied. In order to model this effect the large sets of detailed MC simulations are used. The response of fluorescence telescopes has been simulated and tested as a function of the energy, of the particle type, the atmospheric conditions etc.

Here the dependence of observed air showers as a function of ADC variances will be presented. Two parameters of reconstructed air showers passing the chosen quality criteria (described in Section 8.6) were chosen: the shower distance (i.e. the distance between the shower maximum and FD telescope) and the reconstructed energy of the air shower. These two parameters characterize fluorescence detector's ability to detect air showers with different brightness.

The distribution of both variables is strictly limited by the observation time for given ADC variances: typically more than 85% of total observation time had ADC variances between 15 and 80 $(\text{ADC counts})^2$ (see Fig. 8.1). Therefore the number of observed air showers is naturally the highest during clear moonless periods of the nights.

Reconstructed air shower distances and energies are shown in Fig. 8.8 and Fig. 8.9, respectively. The majority of events have ADC variances within the boundaries typical for clear moonless sky, i.e. in the interval of 20 and 60 $(\text{ADC counts})^2$.

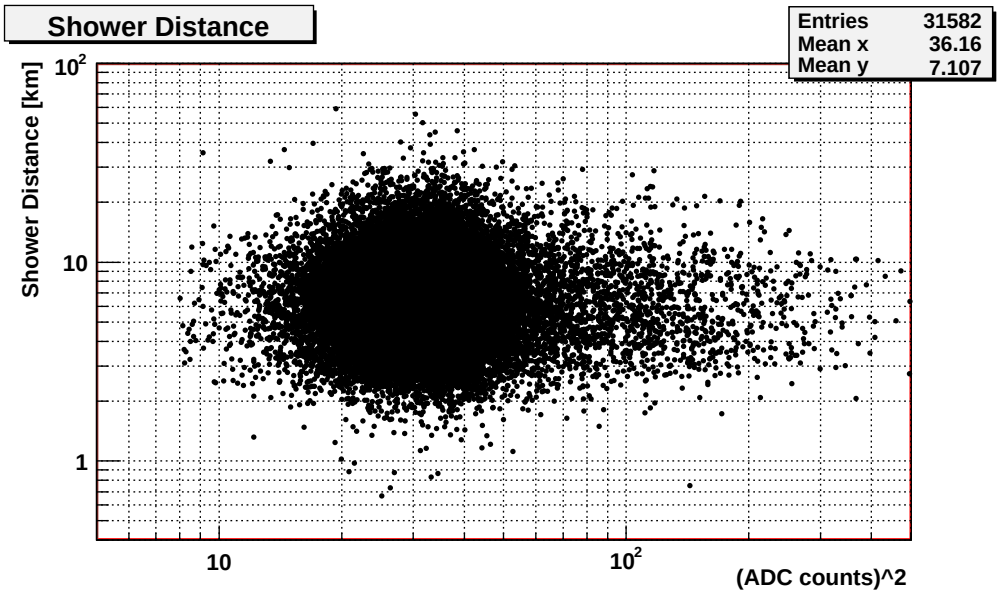

Figure 8.8: Reconstructed distances of measured air showers as function of ADC variances.

The number of air showers which have been possibly lost by the restriction on FD measurement of ADC variances below 100 (ADC counts)^2 in January 2007 can be checked in Fig. 8.9. Depicted data had been observed before the introduction of the cut. The distribution of events in the energy within individual bins of ADC variances does not show any significant difference. No abundance of the most energetic events for ADC variances above 100 (ADC counts)^2 has been found. Further study of this topic will be presented in the Section 8.9.

The average shower distance and energy as a function of ADC variances stays almost constant within the interval defined for clear moonless sky. Beyond the interval from 20 (ADC counts)^2 till 60 (ADC counts)^2, much lower fraction of cosmic rays has been observed and the values significantly fluctuate.

Within the above discussed interval of ADC variances the average shower distance is almost constant (see Fig. 8.10). The average energy only slightly changes with ADC variances from the value of 0.7 EeV up to 1.0 EeV (see Fig. 8.11). But this trend lies within statistical fluctuations.

8.8 Cosmic-Ray Rate

To monitor the observed cosmic-ray rate as a function of night-sky brightness conditions the data has been divided into four groups. Each group is defined by the range of the values of ADC variances. The data were analyzed for each group separately and some interesting differences between the results were found. However, one has to have in mind that only hybrid data were used here.

The first set of events has the ADC variances below 20 (ADC counts)^2. The majority of events have been measured, as expected, within 20 and 60 (ADC counts)^2

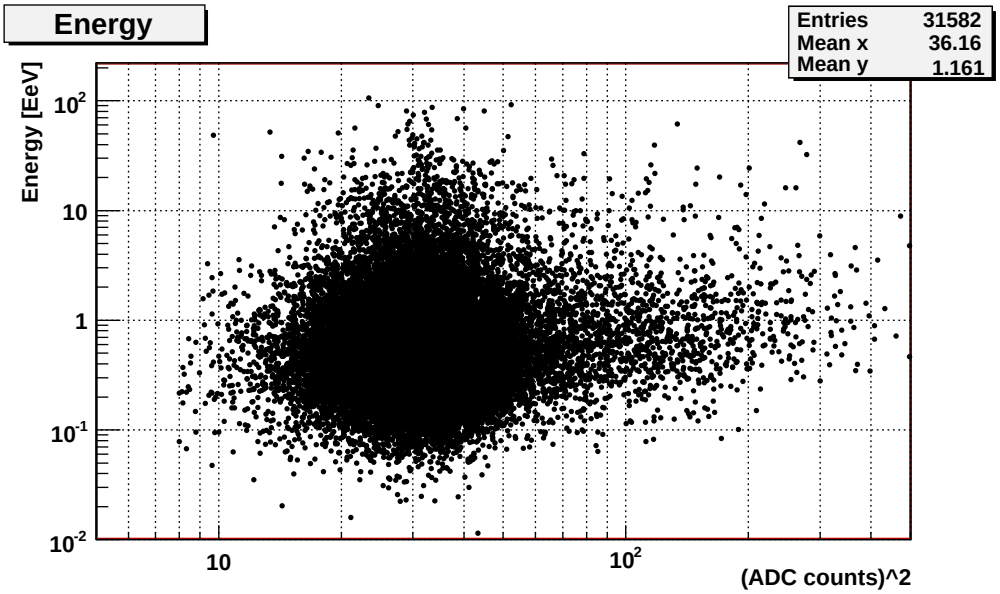

Figure 8.9: Reconstructed energies of measured air showers as function of ADC variances.

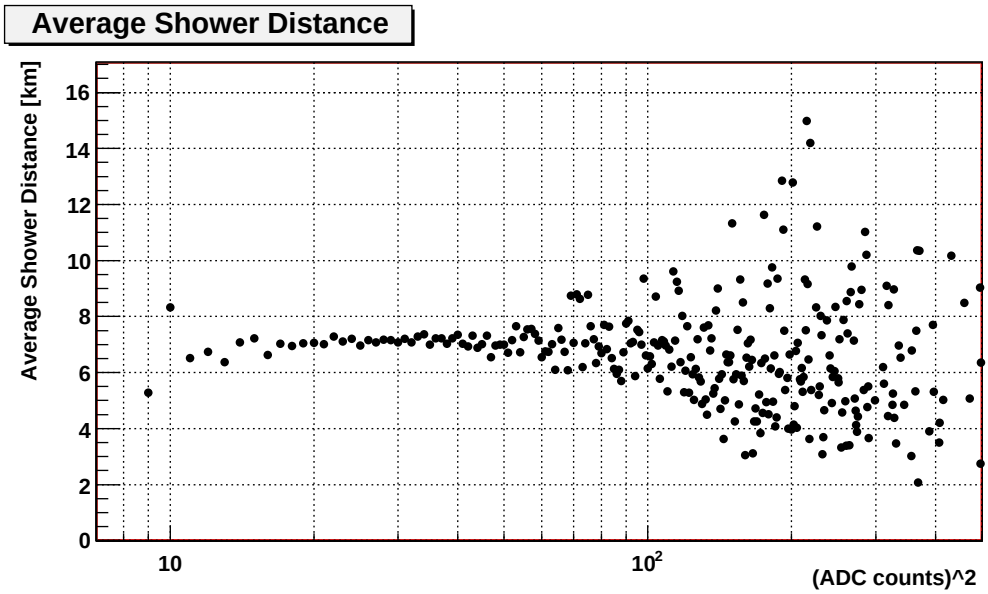

Figure 8.10: Average shower distance of measured air showers as function of ADC variances.

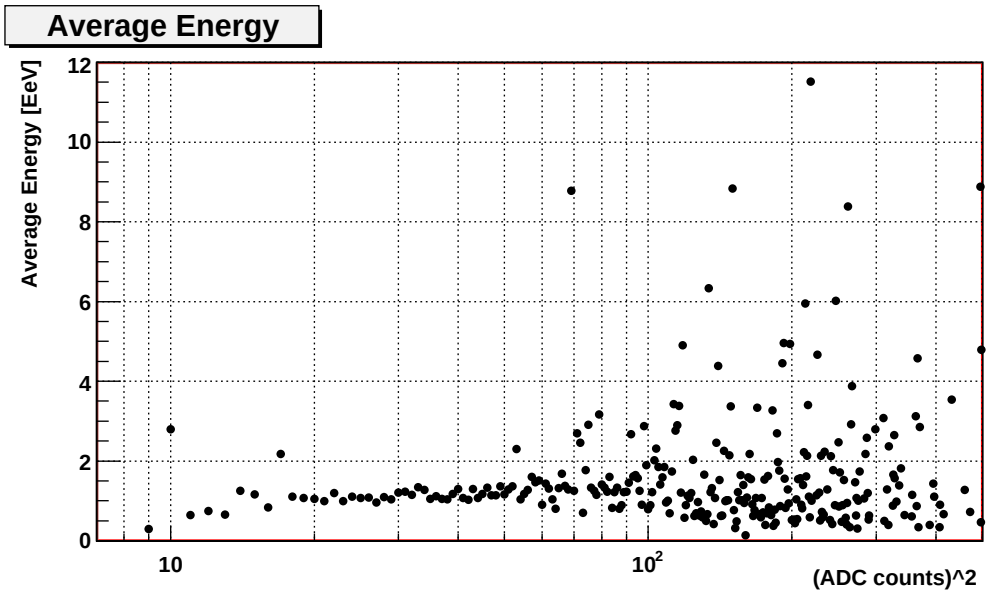

Figure 8.11: Average energy of measured air showers as function of ADC variances.

during clear moonless nights. The last two groups, one with ADC variances between 60 and 80 (ADC counts)^2 and the next one with ADC variances above 80 (ADC counts)^2, suffer from the lack of measured data. The sum of the number of depicted data were normalized to 1 for each set.

The shape of cosmic-ray rate is not the same for all four groups, see Fig. 8.12. There are clear differences for the cosmic rays below 1 EeV. The most significant difference is between cosmic-ray rates for cloudy nights and nights without clouds. It tells us the brighter sky background, the worse triggering of low-energy and therefore fainter air showers.

8.9 Observation Rate

The number of measured events depends on the night-sky brightness, here described by ADC variances. Because of the unclear influence of the installation of corrector rings on light flux, only data from telescopes equipped with corrector rings are described in the following analysis.

Data passing the following conditions have been used in our analysis: the uncertainty in energy reconstruction is less than 20% and the uncertainty of the shower maximum is less than 40 g/cm^2. For each event were assigned ADC variances for the triggered telescope, which were subsequently converted into the photon flux. (The conversion from ADC variances into photon flux is described in the Chapter 9.)

Event rate of the observed air showers as a function of background light is given in (ADC counts)^2 and photon flux for the telescopes is shown in Fig. 8.13. The optimal background interval for fluorescence observation ranges from 20 to 60 (ADC counts)^2 which corresponds to photon background flux from approximately 100 to

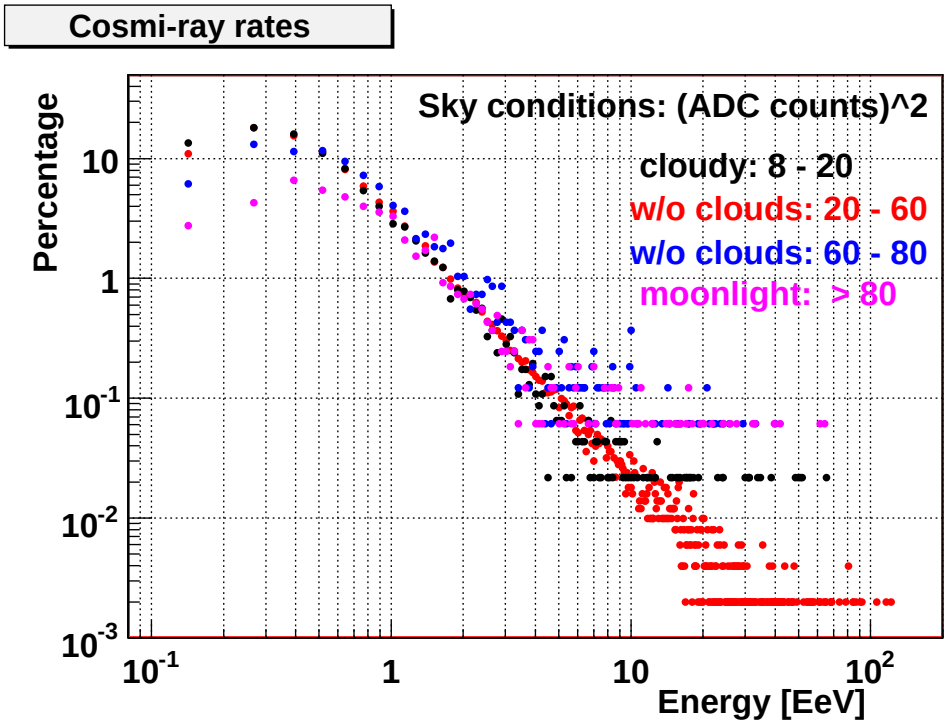

Figure 8.12: Cosmic-ray rates for measured events till June 2008.

250 $m^2 deg^2 \mu s^1$. This range corresponds to clear moonless nights. Under such conditions, more than one cosmic ray shower is observed every 2 hours.

If clouds or scattered moonlight are present the number of air showers significantly decreases. In the first case the light incoming from air showers is shadowed by clouds. In the second case, the signal is mixed up in photons coming from sky background. Let's remind that the operational threshold of the sky background on the camera is set to 100 $(\text{ADC counts})^2$. Observations with background levels higher than this value lead to a loss of sensitivity for more distant air showers. This threshold also preserves the lifetimes of the PMTs, and does not significantly reduce the number of observed showers.

Figure 8.13 shows rather narrow maximum close to the value of 30 $(\text{ADC counts})^2$. For lower and higher values of ADC variances the event rate starts to decrease, more rapidly for the lower values. The former decrease can be easily explained by the presence of clouds. The later decrease may be connected with the reduction of the excess of incoming fluorescence signal above the night-sky background.

The conversion from ADC variances to photon flux is explained in Section 9.2.

8.10 Summary of Sky Brightness Conditions

Four groups of night-sky brightness conditions have been discussed in previous sections. These groups have been defined by the interval of ADC variances measured

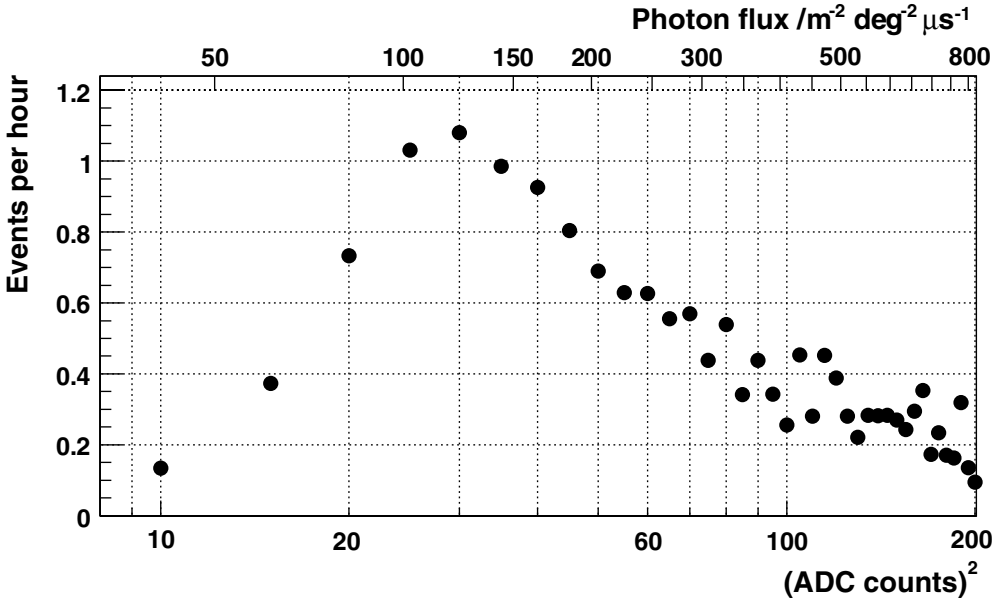

Figure 8.13: Event rate for observed air showers as a function of background light given in (ADC counts)^2 (lower x axis) and photon flux (upper x axis).

by photomultipliers on cameras. They are shown in Tab. 8.1. Also well reconstructed events (they have been described above) observed by fluorescence telescopes at Coihueco were used in this analysis.

The implication of different intervals of night-sky brightness on the observation are summarized in Tab. 8.1. The average energy, the average core distance, the number of observed air showers and the length of observation (given by the number of 30-seconds data acquisition intervals) for given intervals of ADC variances are listed there.

The average energy clearly increases with background brightness from 0.9 EeV to 1.9 EeV, whereas the average core distance remains constant within 10% and its value equals to 6.8 km.

Accumulated anode charge by photomultiplier is also mentioned in the table. These quantity will be defined and closely discussed in the next Chapter. The dramatic increase of accumulated anode charge and simultaneously the lack of observed cosmic-ray showers is evident for nights with bright night-sky. This is clear motivation for the restriction of FD on ADC variances below 100 (ADC counts)^2. It was verified that the amount of lost events (less than 2%) is negligible, whereas the total illumination of photomultipliers decreases by 30%.

Several air showers with energies above 10 EeV were observed for the ADC variances above 100 (ADC counts)^2, but none of them has its energy above 50 EeV. In addition the majority of the most energetic air showers have been observed during periods with the night-sky brightness below 100 (ADC counts)^2 (see Fig. 8.9).

Table 8.1: Average energy $< E >$ in EeV and average core distance $< D >$ in km of cosmic-ray showers observed at Coihueco since Jan 2004 till Dec 2007 for ADC variances σ^2_{ADC} are shown. An average accumulated anode charge Q_A in Coulombs on a camera follows. In the last column is shown the ratio of a number of observed air showers N_{ev} and a number of 30-seconds data acquisition intervals N_σ for given range of ADC variances.

σ^2_{ADC}	N_σ	N_{ev}	$< E >$	$< D >$	$< Q_A >$	N_{ev}/N_σ
8 - 20	13415	1761	0.9	6.7	1.9	0.13
20 - 60	76592	18952	1.0	7.0	23.0	0.25
60 - 80	3599	695	1.4	6.8	2.2	0.19
> 80	7725	374	1.9	6.6	11.4	0.05
> 8	101331	21782	1.0	6.9	38.5	0.21

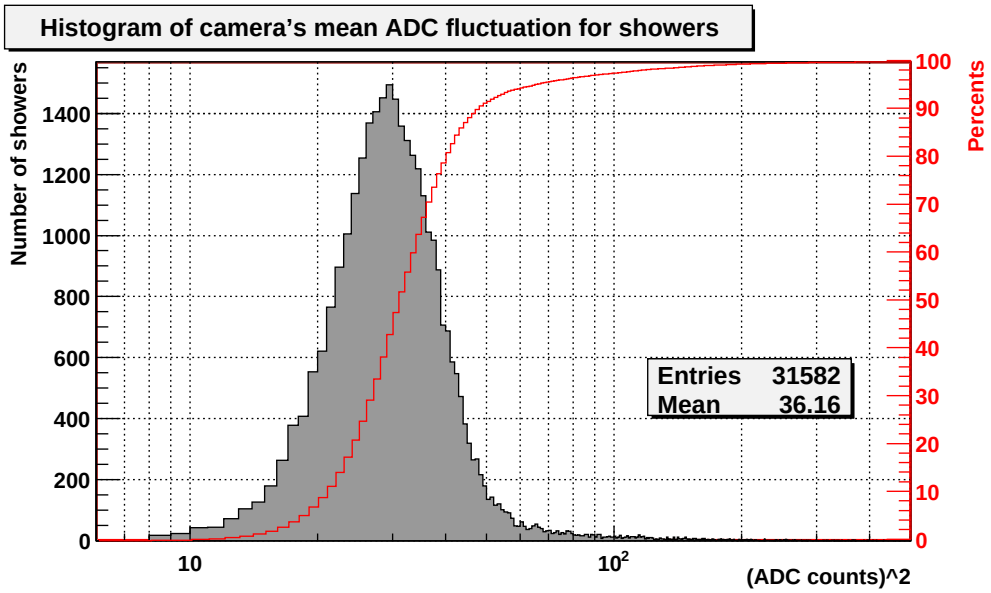

Figure 8.14: Histogram of average ADC variances for measured cosmic-ray showers. Red line shows cumulative distribution of values in histogram.

8.11 Examples of Measurements with Extremely High ADC Variances

To protect the photomultipliers on cameras of fluorescence telescopes the shutters in apertures stay closed or are closed immediately after the brightness of the sky exceed the level of 100 (ADC counts)^2. The shutters of FD telescopes can be closed automatically also in situations, when light sensors placed on the roof of FD buildings send an alert. There are also safety curtains at inner side of the aperture which would fall down. Such cases could happen during power cuts, jamming of shutter door, etc. Since January 2008 an automatic control of ADC variances on the cameras has been applied. It closes shutters if the light flux of scattered moonlight exceeds critical level. In all other cases the shutters are operated by shift crew.

In spite of the routine control of night-sky brightness, the photomultipliers had been sometimes illuminated by very high flux of background photons. The most cases when observed level of background brightness exceed a few hundreds of 100 (ADC counts)^2 were caused by sudden scattered moonlight particularly during nights with the Moon close to the quarter phase.

Sometimes the source of extremely high level of ADC variances measured by fluorescence telescopes has not been found. The number of measurement of ADC variances above the of 500 (ADC counts)^2 can be found in Tab. 9.6. The frequency of such extreme cases has been lowered during last years.

In the following subsections two examples which illustrate the response of PMTs to extremely high level of ADC variances will be presented. The first example shows the status of one camera after illumination by sunlight. The second case gives an example of blinding one part of a camera, caused by unknown reason.

8.11.1 PMT 183 on Camera 3 at Coihueco

The first example concerns FD observation made by the telescope number 3 at Coihueco on January 7th, 2006 during the last night of FD observation period. Astronomical night started at 22:45 (local Malargüe time, i.e. GMT offset equals to -4 hours during winter). Very high ADC variances visible on PMT 183 in Fig. 8.15 were caused by the Moon. The Moon set below horizon at 0:47. The end of astronomical night was at 3:48 and FD operation should be stopped. However, it was not.

The rapid increase of variances since 4:10 was clearly caused by the sunlight. The civil twilight (Sun's position 6° below the horizon) was at 5:03 and the sunrise at 5:32. The shutters were not closed till 4:26 as can be seen in data. Therefore, Fig. 8.15 illustrates the increase of ADC variances before the sunrise.

All 440 PMTs on the camera were illuminated by sunlight, but only PMT number 183 showed unusual behaviour during next three FD operation periods. The ratio of ADC signal on PMT number 183 and ADC signal averaged over its six neighbouring PMTs is shown in Fig. 8.16. The ratio had increased during the first FD observation night after January 7th (i.e. January 21st, 2007). The ratio dramatically fluctuates and it was approximately ten times higher than during the previous months on

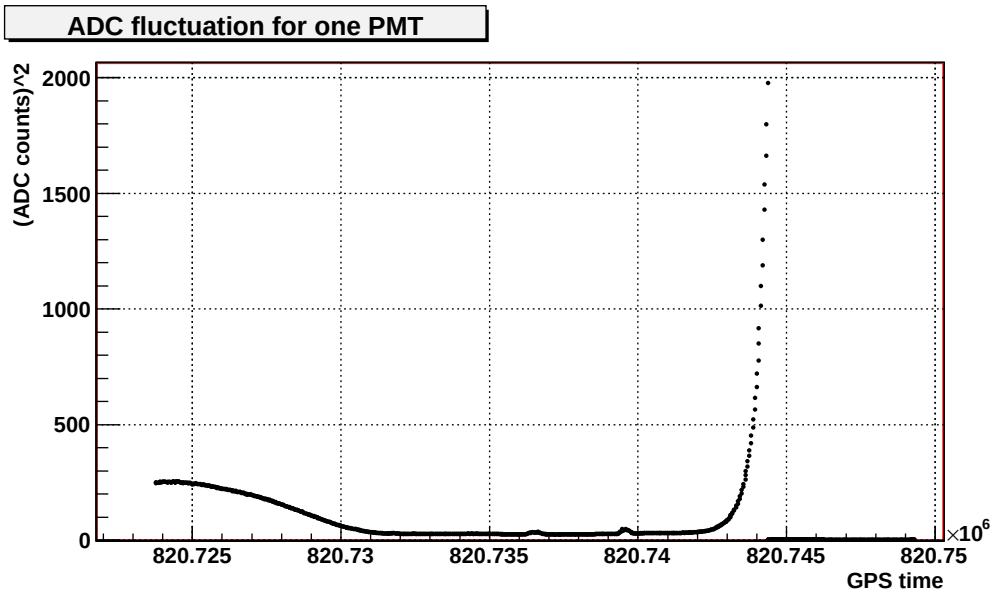

Figure 8.15: Increase of ADC variances on PMT 183 on the third camera at Coihueco. The time step between points is 30 seconds.

average. Although this PMT was not repaired, the ratio had dropped to normal value on April 1st and did not indicate any anomalous behaviour thereafter.

8.11.2 PMT 408 on Camera 4 at Loma Amarilla

The second example concerns the photomultiplier number 408 at Loma Amarilla on the camera 4. ADC signal above 14 thousands (ADC counts)^2 was recorded on September 12, 2007 (in GPS time since $T_{GPS} = 873676827$). Even during period when shutters were closed (however the high voltage on the camera was still turned on) the value did not drop down.

The rapid increase of ADC variances occurred during the 10th day of FD observation period. Very cloudy night was reported by FD shifters during the night. As is shown on Fig. 8.17 very high ADC signal was seen also on the following PMTs: the PMT 434 had comparable value but it strongly fluctuated, the signals on the PMT 374, 384, 386 and 387 were around 10 times lower than signal on the PMT 408. The ADC signal on the PMTs placed on the same part of the camera as the PMT 408 was equal to electronic noise (i.e. around 3.5 (ADC counts)^2), while more distant PMTs had values well above electronic noise.

The value of ADC variances become normal during the second day of the next FD at $T_{GPS} = 875491820$. For the distribution of ADC variances on the camera during normal operation see Fig. 10.1.

It is not clear what caused such extremely high ADC signal and if it contributes to the accumulated anode charge. However the part of the camera was not able to take data during this time period.

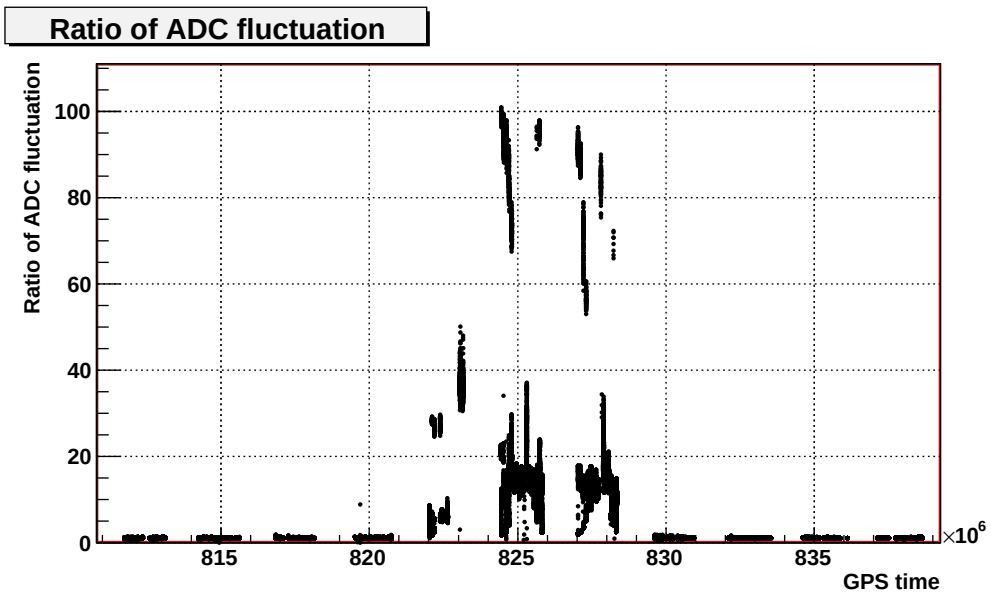

Figure 8.16: Ratio of ADC variances on PMT 183 and the average value of his six nearest neighbours on camera 3 at Coihueco.

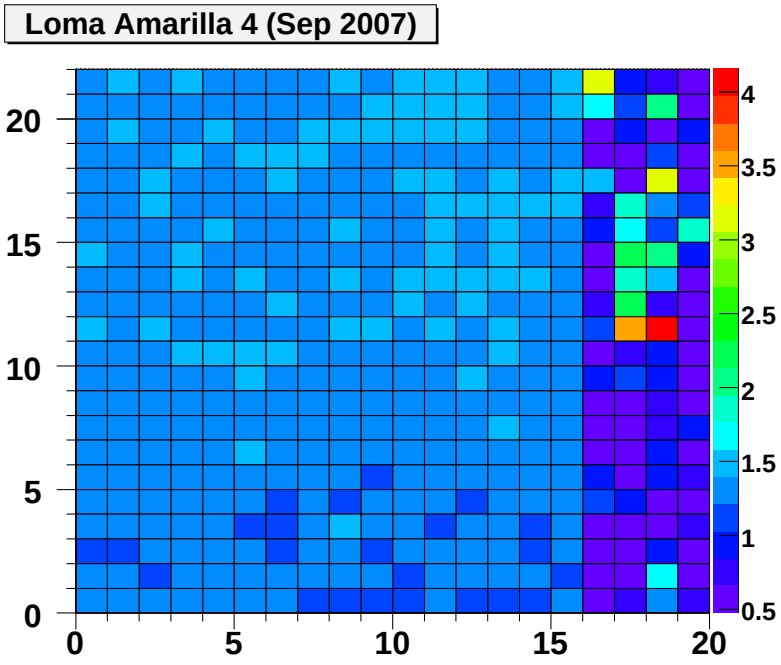

Figure 8.17: ADC variances on camera 4 at Loma Amarilla averaged over problematic period in Sep 2007. On x-axis and y-axis is shown column and row number, respectively. Scale of ADC value is logarithmic and value of 0.5 equals to electronic noise.

Chapter 9

Accumulated Anode Charge on Photomultipliers

An accumulated anode charge is a parameter which affects the decrease of PMT sensitivity at a constant high voltage. It can be calculated from a number of photoelectrons illuminating the PMT. The degradation of PMT sensitivity is caused mainly by the damage on a surface of the last dynode. Calibration measurements indicate higher decrease of PMT sensitivity than was predicted from data provided by PHOTONIS, the producer of PMTs.

Several observational parameters have been studied since the first year of data taking. The analysis presented in this chapter provides a place for search of an impact of different operation characteristics on the calibration results.

As was mentioned in Chapter 8 the fluctuations of ADC signal and its average are related. Moreover the value of ADC fluctuation is proportional to the incoming photon flux. Therefore the ADC signal also describes the flux of incident light.

9.1 Calculation of Photoelectrons

The conversion of measured ADC signal into the number of photoelectrons is described in [Kle03]. Assuming random processes at the PMT dynodes the number $N_{p.e.}$ of photoelectrons per 100 ns as a function of the ADC variance σ^2_{ADC} can be written as

$$N_{p.e.} = \frac{10\ \sigma^2_{ADC}}{2F\ (1 + V_G)\ A^2_G}\ . \tag{9.1}$$

Here V_G is the gain variance of the PMT and F is the noise equivalent bandwidth in MHz from the complete analog signal chain. The factor $10/2F$ accounts for an effect of an electronic filter. The absolute gain (in ADC counts per photoelectron) A_G of the PMT converts the sky background variance into ADC variances as follows

$$A_G = \eta\ G\ E = \frac{1}{C_{PMT}\ f_{opt}\ Q}\ , \tag{9.2}$$

where η is the PMT collection efficiency at the first dynode, G is PMT gain and E (in ADC counts per electrons) is the electronics conversion constant. The absolute gain

Table 9.1: Parameters used in calculation of photoelectrons and photon flux for telescopes without or with corrector ring (CorR).

			no CorR		with CorR	
Q	V_G	F [MHz]	f_{opt}	A [m^2 deg^2]	f_{opt}	A [m^2 deg^2]
0.29	0.41	3.3	0.47	4.6	0.49	7.7

can be calculated equivalently from a calibration constant C_{PMT} and a quantum efficiency Q of the PMT and an optical factor f_{opt} which is the product of the transmission of telescope optical components.

A photoelectron subsequently produces a flux of electrons due to striking eight dynodes in a PMT. The number of the electrons striking an anode is given by

$$N_A = G\, N_{p.e.}\ , \tag{9.3}$$

where $G = 5 \times 10^4$ is the gain of the PMT.

In our calculation the calibration constant C_{PMT} should be in principle given for each PMT. Values of other parameters can be assumed to be constant for all PMTs. As was argumented in [Kle03] the value of V_G varies within the 10% range, which induces an error of 2.5% in the number of photoelectrons. These results are similar for all other parameters. The values used for the calculation were adopted from [Car04] and are shown in Tab. 9.1 for telescopes with and without corrector ring.

9.2 Photon Flux

A photon flux per m^2 deg^2 μs is proportional to measured ADC variances. The method presented in [Car04] was employed for its calculation, it makes use of measured flux of photoelectrons

$$\Phi_\gamma = \frac{N_{p.e.}}{Q\ f_{opt}\ A\ \Delta t} = \frac{10\ C_{PMT}^2\ Q\ f_{opt}}{2F\ (1+V_G)\ A\ \Delta t}\ \sigma_{ADC}^2\ . \tag{9.4}$$

The sampling time slot Δt equals to 100 ns and A is the PMT aperture in m^2 deg^2.

The equation can be simplified in the case when the calibration constant is assumed to be same for all PMTs

$$\Phi_\gamma = T_{conv}\ \sigma_{ADC}^2\ , \tag{9.5}$$

where T_{conv} is the conversion factor for a telescope. For telescopes without corrector rings the conversion factor $T_{conv} = 7.6$ and for telescopes with installed corrector ring it equals to 4.1. In both cases $C_{PMT} = 4.5$ was taken for all PMTs.

9.3 Degradation of Sensitivity

The accumulated anode charge can be calculated as a sum of the number of anode electrons incoming during given time period. The shortest possible integration period is 30 s, which is the sampling time for measurement of ADC variances. Therefore the formula for the accumulated anode charge has the following form

$$Q_A = e\ N_{p.e.} \left(\frac{30\ \text{s}}{100\ \text{ns}} \right)\ \Sigma\sigma^2_{ADC}\ , \tag{9.6}$$

where $\Sigma\sigma^2_{ADC}$ is the sum of ADC variances measured during given period.

The relative degradation of PMT gain is the function of accumulated anode charge. As was described above, the main source of the degradation is the damage of the surface of the last dynode in PMT. This effect is much more significant than any other effect (e.g. changes of photocathode). The relative degradation in time $G(t)$ is described by the following equation

$$G(t) = 2^{-\frac{Q_A}{Q_{1/2}}} \simeq \exp\left(-0.693\ \frac{Q_A}{Q_{1/2}} \right)\ . \tag{9.7}$$

The numerical values in equation were provided by the producer of PMTs. The value of $Q_{1/2}$ could differ from one PMT to another, but should be higher than 500 C for all PMTs. This values indicates the amount of accumulated anode charge for which PMT sensitivity drops by $\exp(-0.693) \simeq 50.0\%$. However a lab experiment on some older PMTs indicates lower values for $Q_{1/2}$, usually around 200 C [Gra08]. It is clear that tested PMTs age much faster than was expected and the ageing was clearly attributed to a degradation of the last dynode's surface. The degradation of PMT sensitivity is shown in Fig. 9.1 for different values of $Q_{1/2}$.

9.4 Calibration Measurements

The fluorescence telescopes are regularly monitored by two calibration methods. The first method - absolute calibration - measures the response of PMTs to light flux with known intensity. The calibrated light source is placed at the telescope aperture and provides uniform illumination of each pixel on a camera. Light from the calibrated source propagates through all optical components of a telescope. Such measurement provides the conversion between the digitized signal (in ADC units) and the photon flux incident on telescope aperture. Therefore transmission and reflection of a whole telescope optical components are monitored. Overall uncertainties of absolute calibration are about 12% and are dominated by systematics.

The change of properties of an individual optical component can be tracked by relative calibrations. These measurements determine the response of the telescope to light pulses from either a LED source (relative calibration A) or a xenon flash lamp. Relative calibration measurements monitor short and long term changes between successive absolute calibration measurements. Relative calibration A has been the most extensively analyzed one up to the present and it has provided the most relevant data on the behaviour of the PMTs.

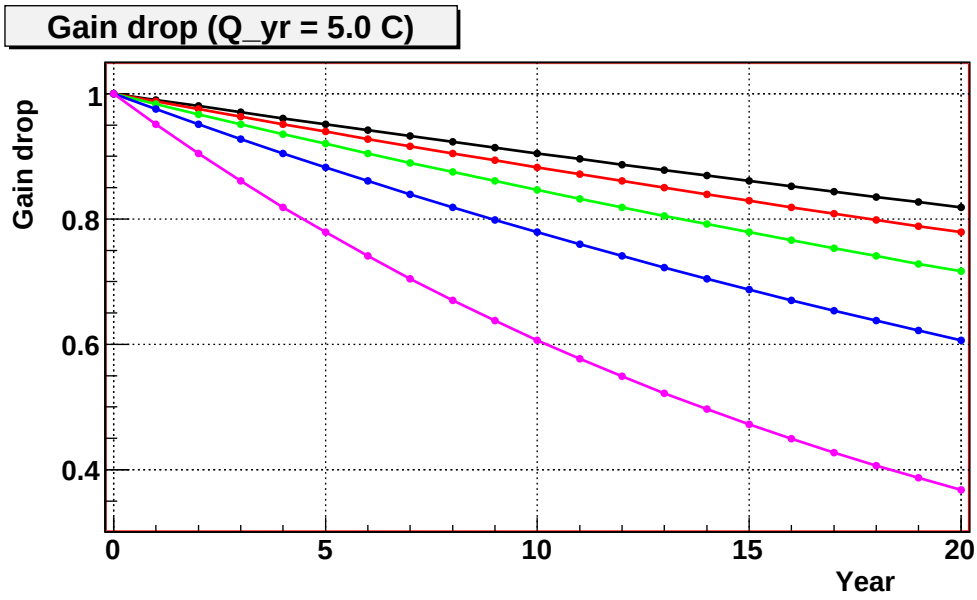

Figure 9.1: Gain drop calculated from Eq. 9.7 for yearly accumulated charge 5.0 C and several values of $Q_{1/2}$ discriminated by line's color: black for 500 C, red for 400 C, green for 300 C, blue for 200 C and magenta for 100 C.

For example night-to-night and seasonal fluctuations of the PMT response to light flux has been identified. One of the most important results is certainly the observation of the overall degradation of PMT sensitivity. In the following sections the amplitude of long term decrease of PMT sensitivity will be confronted with the geometrical orientation, the uptime, the incidence of the Moon and other parameters typical for the fluorescence telescopes.

The calibration routines and the hardware configuration were in detail described in [Bra04] and [Kna07].

9.5 Measured Degradation of Sensitivity

The decrease of PMT sensitivity was observed in all cameras in the analysis of calibration data (see Tab. 9.2). The observed changes are roughly the same for all PMTs on the same camera, but shows differences between cameras in different telescopes.

There are several possible explanations of the downgrade of PMT sensitivity. The most common explanation is PMT aging. The aging is caused by the damage of the last dynode's surface. It seems the changes of the photocathode and of the entrance window do not significantly contribute to the aging. As it is shown in Eq. 9.7, this process should be described by the total amount of accumulated anode charge.

The detailed study of PMT behaviour shows variability on different time scales (from hours to years). We will focus only on long-time scale trend. Time dependence of relative calibration data corrected by the stability of the light source shows

Table 9.2: Yearly decrease of the response of the PMTs to the calibration A (corrected to light source stability). No long-term data were available for Loma Amarilla.

	1	2	3	4	5	6
Los Leones	3.2%	2.3%	5.5%	3.0%	3.1%	4.2%
Los Morados	1.7%	$< 1\%$	1.4%	$< 1\%$	2.8%	1.0%
Coihueco	2.9%	5.5%	4.8%	3.5%	2.3%	1.0%

Table 9.3: Azimuth angle between back wall of FD buildings and direction to North.

FD	LL	LM	LA	CO
angle	60°	30°	82°	27°

complicated structure but generally can be characterized by a linear fit. The linear fit for a camera is the average of values obtained for 440 PMTs of the camera. The slope of the linear fit provides the change of PMT sensitivity per time.

The discrepancy between calculated and observed losses of PMT sensitivity has motivated the search of their source. We have analyzed the observation characteristics of the cameras that were then confronted with the calibration results. In the analysis the following parameters were chosen: the total accumulated anode charge, the observation time (it is defined as the sum of time periods when camera's high voltage was turned on), their ratio (i.e. accumulated anode charge per hour), the frequency of measurement during nights with extremely high ADC variances and the fraction of the observation time with the Moon inside and closer than 5 degrees from the telescope field of view.

9.6 Orientation of Telescopes

The orientation of FD telescopes provides a unique way to compare calibration results between telescopes observing the same part of the sky. The orientation of a back wall of the FD building can be found in Tab. 9.3. Due to the orientation of FD buildings there are many telescopes observing almost the same part of the sky, see Tab. 9.4. There is one triplet of telescopes at different buildings (LL1, LA1, CO4) oriented in almost the same direction.

Only the orientation of building back wall at Loma Amarilla significantly differs from the multiple of 30° from the direction to the North. This shift equals to 8° and thus the intersections of the field of view of a camera in this building and any in other buildings do not exactly overlap. Nevertheless the difference is rather small and equals to $8/30 \simeq 27\%$. FD buildings at Los Morados and Coihueco are sitting opposite to each other and therefore no of their telescopes is oriented into the same direction.

Surprisingly the analysis of calibration data shows differences between the cam-

Table 9.4: Triplet and doublets of FD telescopes observing almost same part of the sky.

LL 1	LA 1	CO 4	LM 5	LA 6
LL 2	CO 5	-	LM 6	LA 5
LL 3	CO 6	-	LA 2	CO 3
LL 4	LM 1	-	LA 3	CO 2
LL 5	LM 2	-	LA 4	CO 1
LL 6	LM 3	-	LA 5	LM 5
			LA 6	LM 6

eras observing the same part of the sky. The most significant discrepancy is between the results from LL3 and CO6. While camera at LL3 has the largest observed decrease of PMT sensitivity, the camera at CO6 shows one of the smallest values.

However, we must be aware of the differences between operation conditions of these two telescopes. Such differences can be for example the frequency of turning on and off the high voltages on the camera, hardware or software problems and also local weather conditions (the presence of the heavy clouds, the lightnings). The influence of such parameters may play an important role and must be considered when the measurements shown in Tab. 9.7 are discussed.

9.7 Presence of Moon

The presence of the Moon as the main source of ADC variances above 80 (ADC counts)^2 must be monitored during fluorescence detector operation. The position of the Moon is calculated in advance and telescope shutters should be closed if the position of the Moon is closer than 5° to the telescope field of view or if ADC variances go over 100 (ADC counts)^2. Despite of the knowledge of the actual Moon position, the night sky brightness must be carefully monitored. The scattered moonlight is bright enough to illuminate also telescopes pointed far away from actual Moon position. In such cases, which occurred many times, the ADC variances on cameras rapidly increased. The parametrization of the light level caused by the scattered moonlight is difficult and it was not presented up to now. Also the frequency of such cases can hardly be estimated from the available data.

The calculated fraction of the observation time when the position of the Moon lies closer than 5° to field of view of given telescope is shown in Tab. 9.5. The most interesting is the comparison of telescopes having the highest fraction of time with the presence of the Moon with those telescopes which are oriented to the South and do not see the Moon at all (LA3, LA4, CO1 and CO2).

The results of the study of the presence of the Moon in the telescope field of view on the degradation of PMT sensitivity are summarized in Section 9.10.

Table 9.5: Fraction of time with the position of the Moon within 5° to telescope FOV.

	1	2	3	4	5	6
Los Leones	4.0%	3.2%	2.6%	0.4%	0.6%	3.1%
Los Morados	0.4%	0.6%	3.1%	3.6%	4.7%	0.8%
Loma Amarilla	3.9%	0.1%	0%	0%	1.7%	4.1%
Coihueco	0%	0%	1.1%	4.1%	3.2%	2.4%

9.8 Accumulated Anode Charge

The accumulated anode charge is the crucial parameter for the calculation of the aging of PMTs (see Eq. 9.7). It is calculated from the measured data by the equation 9.6. Calculated sums of ADC variances for individual PMTs are shown in Fig. 9.2. The PMTs on two cameras (telescope 4 and 5 at Los Leones) have been replaced in February 2004. Before this date they were operated already in Engineering Array and during another five FD shifts since October 2003. Because of the PMTs replacement the data from that time interval are not used in the presented analysis.

As can be expected the brightness of the night sky alters with the zenith angle. The elevation dependence appeared naturally in total anode charges accumulated by PMTs. The upper part of camera (looks closer to the horizon) has accumulated around two times higher ADC signal (which can be easily converted into accumulated anode charge) than the lower part. The differences between lower and upper parts of the cameras are significant and should be seen in the calibration data.

The unique examination can be done at Los Leones. The upper left part of the camera in the telescope number 6 observes the light pollution from the city of Malargüe. The right part of the camera observes the same part of the sky, but it is not affected by the light pollution. Hence, the total anode charge accumulated by the two different parts of this camera must differ. The difference is apparent indeed. The part of the camera pointed towards the city has accumulated two times higher anode charge than the second part of the same camera. The light from the city of Malargüe can also be found at the camera 1 at Coihueco, but it is much less prominent because the telescope is located almost 30 km from the city.

Another interesting feature in Fig. 9.2 are the strips on the upper part of the camera 6 at Los Morados (see Fig. 9.3). By comparison of the high-voltage classes of PMTs mounted on the camera (see Fig. 9.4) this feature can be explained. The camera was assembled from different classes of PMTs. The colours in Fig. 9.3 show different high-voltage classes: those with purple colour belong to the classes with lower high voltage (class G, H and J) and those with red colour belong to the class with higher high voltage (class A). Others parts of the camera contain PMTs belonging to classes with similar characteristics. Therefore the pixels in the lower right part of the camera (the PMTs mounted here belong also to the class G) do not show significant differences in the comparison with surrounding pixels.

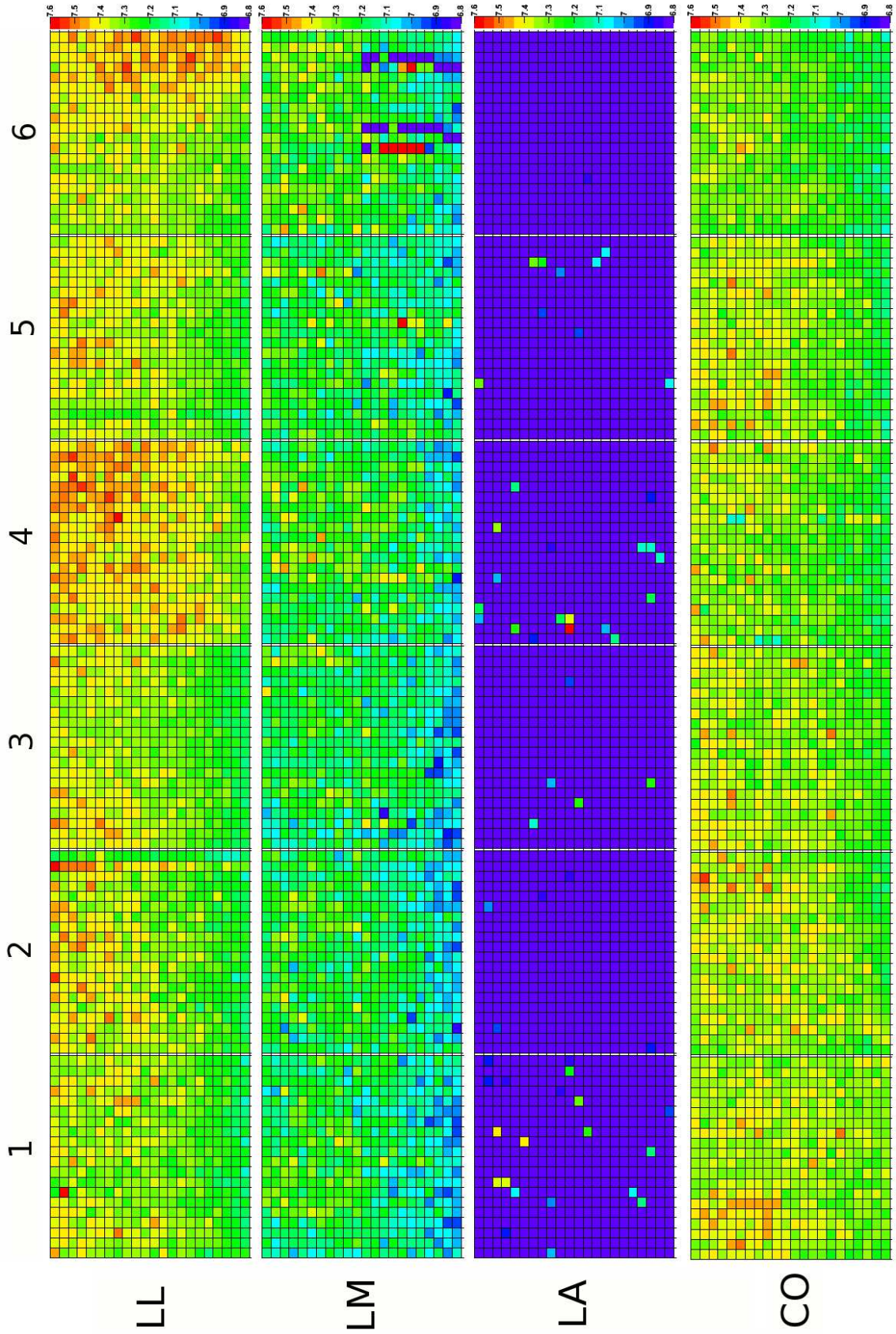

Figure 9.2: FD cameras with sum of ADC fluctuations collected till end of 2007. Logarithmic scale goes from 6.8 (magenta) to 7.6 (red) in (ADC counts)^2. Orientation of telescopes can be found in figure 4.1.

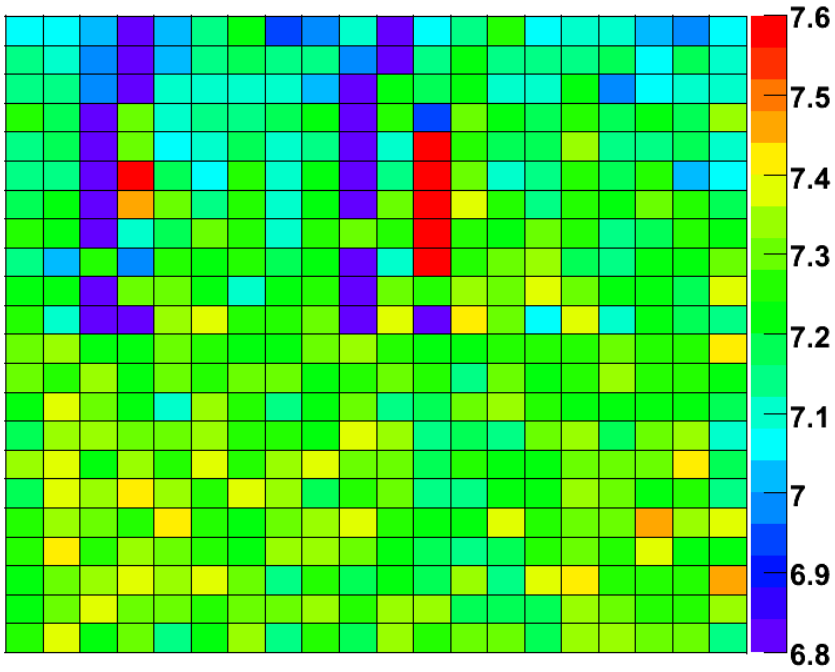

Figure 9.3: Sum of ADC variances on camera 6 at Los Morados. Figure was rotated by 180° to agree with figure 9.4.

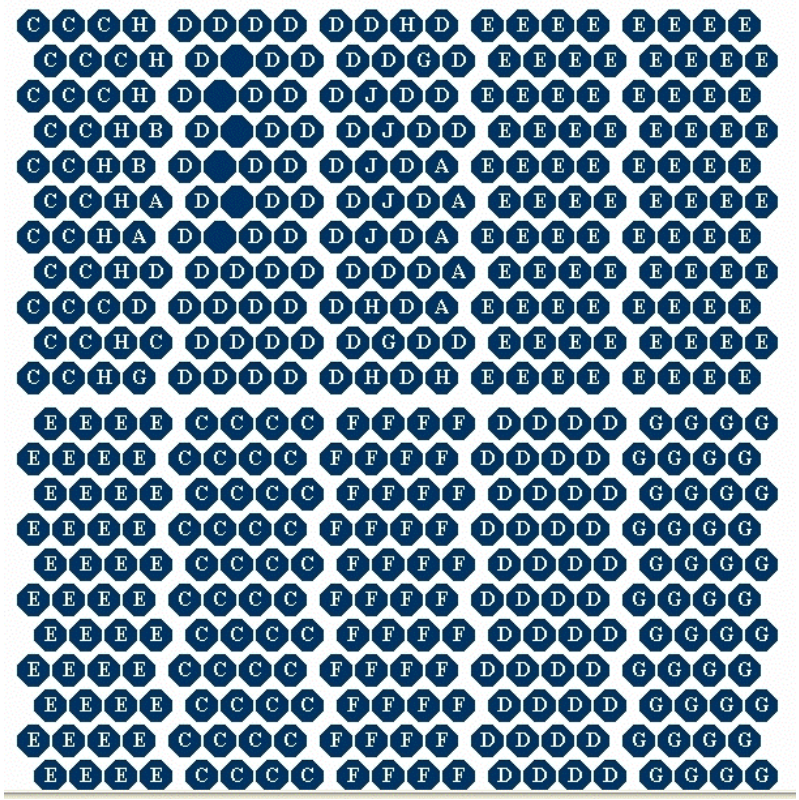

Figure 9.4: Classes of PMTs on camera 6 at Los Morados.

9.9 Measurements with High ADC Variances

For safety reasons ADC variances on a camera should not exceed 100 (ADC counts)^2. Unfortunately there has been some cases when it happened for whatever reasons. The main sources of the extremely high ADC variances could be the Sun, direct and scattered light from the Moon and lightnings. The true source of high ADC variances cannot be always revealed without supplementary information (such as actual cloud coverage, the height of the clouds, the distance of the lightnings etc.).

In many cases the identification of the true source is possible if the Moon was above the horizon. The Moon itself and also scattered moonlight are very bright sources, in particular during a few nights after and before Moon's the first and the last quarter, respectively. If an observer does not keep an eye out for the rapidly varying level of ADC variances during these nights, the measured ADC variances could easily become extremely high. Already a few minutes delay in closing shutters can cause problems.

There is a question, if extremely high ADC variances can cause larger losses of PMT sensitivity than is predicted by Eq. 9.7. The number of intervals, when ADC variances were above 250, 500 and 1000 (ADC counts)^2, were counted for FD telescopes. In Tab. 9.6 numbers for ADC variances above 500 (ADC counts)^2 are shown. If the answer to the above question is affirmative we will expect the highest numbers in cameras showing the largest degradation of PMT sensitivity. Such hypothesis has not been confirmed.

9.10 Relation of Studied Parameters to Degradation of Sensitivity

The most illuminated telescopes are those at Los Leones and Coihueco, which have started regular operations as the first one. The total observation time – in other words total illumination – is the primary factor for the accumulated anode charge. Averaged values for the telescopes are given in Tab. 9.6. Other studied parameters which can play role in the degradation of PMT sensitivity observed by the calibration measurements are also written in the table. All results are for data measured till the end of the year 2007.

The highest accumulated anode charge can be found on cameras 3, 4 and 6 at Los Leones. The situation of camera 6 at Los Leones has been affected by the light pollution from the city of Malargüe. The comparison of the results for these telescopes with others can be used for detailed investigation of the degradation tendency found by the absolute and relative calibration measurements. Nevertheless also other effects experienced in the performance of fluorescence telescopes must be considered, namely the frequency of the presence of the moonlight, the accumulated anode charge per year and some others.

The accumulated anode charge Q_A (see Eq. 9.6) per time has also been studied. The value of ADC variances is the average of $2^{16} - 1 = 65,535$ measurements, each obtained during 100 ns ADC integration period. Therefore the constant value of the

measured ADC variances during each 30 s period was assumed. The observation time of a telescope T_{obs} is calculated as (30 N_{30}) s, where N_{30} is the number of 30 s intervals of ADC variances measurement. Only telescope callibration constants (i.e. not values for each PMT) were used.

As was demonstrated on two PMTs from HiRes experiment by [Gra08] the value of $Q_{1/2}$ seems to equal to 200 C instead of 500 C. The comparison of Q_A with the calibration results can also provide estimates of $Q_{1/2}$ calculated by Eq. 9.7. Expected values of PMT degradation for measured data by FD telescopes are shown in Tab. 9.7. By the comparison with the calibration measurements (see Tab. 9.6) the value of $Q_{1/2}$ for the particular telescope can be estimated. The same procedure can be applied also for the individual PMT. It seems that the real values of $Q_{1/2}$ are significantly lower than 500 C.

Other effects can also contribute to PMT losses of sensitivity and we have discussed some of them. Because the downgrade of PMT sensitivity is comparable for all PMTs mounted on the same camera, it evokes that some other effect compensates the elevation dependence of the camera's illumination (see Section 10.2).

However, new callibration measurements show the reduction of PMT degradation since the the second half of year 2007. It could be attributed to the implementation of new maximum value of ADC variances during FD measurement, as discused in 8.3. Also the reduction of the fraction of yearly accumulated anode charges and the number of measured high ADC variances (e.g. N_{500}) has been observed since the same time period.

Table 9.6: The studied parameters and observed values for FD telescopes measured till end of year 2007: the fraction of calculated observation time with the Moon's position inside 5° to telescope FOV f_{Moon}, the accumulated anode charge Q_A during telescope observation period T_{obs}, their ratio in mC per hour, the number of 30 second periods with ADC signal above 500 (ADC counts)^2 N_{500} and yearly decrease of PMT sensitivity in percents given by relative calibration A (Cal A).

Eye	Parameter	1	2	3	4	5	6
LL	f_{Moon} [%]	4.0	3.2	2.6	0.4	0.6	3.1
	Q_A [C]	22.8	23.4	30.6	30.7	27.4	31.2
	T_{obs} [h]	4729	4785	5441	5122	4971	4861
	Q_A/T_{obs} [mC/h]	4.8	4.9	5.6	6.0	5.5	6.4
	N_{500}	119	288	154	302	260	254
	Cal A [%/yr]	3.2	2.3	5.5	3.0	3.1	4.2
LM	f_{Moon} [%]	0.4	0.6	3.1	3.6	4.7	0.8
	Q_A [C]	14.0	13.4	16.2	16.7	16.3	16.1
	T_{obs} [h]	3452	3429	3595	3515	3472	3497
	Q_A/T_{obs} [mC/h]	4.0	3.9	4.5	4.7	4.7	4.6
	N_{500}	92	72	479	1051	698	544
	Cal A [%/yr]	1.7	< 1	1.4	< 1	2.8	1.0
LA	f_{Moon} [%]	3.9	0.1	0	0	1.7	4.1
	Q_A [C]	3.8	3.5	3.9	4.4	4.0	3.8
	T_{obs} [h]	917	928	902	928	928	897
	Q_A/T_{obs} [mC/h]	4.1	3.8	4.3	4.7	4.3	4.2
	N_{500}	412	2	7	5	5	9
	Cal A [%/yr]	(8.9%)	(7.0%)	(10.4%)	(7.0%)	(4.3%)	(8.7%)
CO	f_{Moon} [%]	0	0	1.1	4.1	3.2	2.4
	Q_A [C]	21.8	26.9	27.6	18.7	20.2	21.1
	T_{obs} [h]	4347	4879	4908	4220	4333	4309
	Q_A/T_{obs} [mC/h]	5.0	5.5	5.6	4.4	4.7	4.9
	N_{500}	400	174	504	81	479	169
	Cal A [%/yr]	2.9	5.5	4.8	3.5	2.3	1.0

Table 9.7: Calculated losses of PMT sensitivity in percents for the accumulated anode charge during the whole time of operation (see Tab. 9.6) and several half-life anode charges $Q_{1/2}$ in Coulombs.

Eye	$Q_{1/2}$	1	2	3	4	5	6
LL	500	3.1	3.1	4.3	4.4	3.8	4.2
	400	3.9	3.9	5.3	5.5	4.8	5.2
	300	5.2	5.2	7.0	7.2	6.3	6.8
	200	7.6	7.6	10.3	10.7	9.3	10.1
	150	10.1	10.1	13.5	14.0	12.2	13.2
	100	14.7	14.7	19.6	20.2	17.7	19.1
LM	500	1.9	1.8	2.2	2.2	2.2	2.2
	400	2.3	2.2	2.7	2.8	2.7	2.7
	300	3.1	3.0	3.6	3.7	3.6	3.6
	200	4.6	4.4	5.4	5.5	5.4	5.3
	150	6.1	5.9	7.1	7.3	7.1	7.0
	100	9.0	8.7	10.4	10.7	10.5	10.4
LA	500	0.5	0.4	0.5	0.5	0.4	0.5
	400	0.6	0.5	0.6	0.7	0.6	0.6
	300	0.8	0.7	0.8	0.9	0.7	0.8
	200	1.2	1.1	1.2	1.4	1.1	1.2
	150	1.6	1.5	1.6	1.8	1.5	1.5
	100	2.4	2.2	2.4	2.7	2.2	2.3
CO	500	2.8	3.5	3.7	2.7	2.6	2.8
	400	3.5	4.3	4.6	3.3	3.2	3.4
	300	4.7	5.7	6.1	4.4	4.3	4.6
	200	6.9	8.4	9.0	6.5	6.3	6.8
	150	9.1	11.1	11.8	8.6	8.3	8.9
	100	13.3	16.2	17.2	12.7	12.2	13.1

Chapter 10

Night-Sky Brightness

The photomultipliers on cameras observe different parts of the celestial sphere. The measured illumination changes with both, azimuth and zenith angle. The elevation dependence is similar for all telescopes, but the latter shows clear influence of artifical light sources.

The study of the elevation dependence of measured night-sky brightness can be done only for clear moonless sky. We have used the interval of measured ADC variances on photomultipliers for the definition of clear moonless nights, see Section 8.1. Our results do not agree with the theoretical prediction and thus the measurement made by atmosphere monitoring devices will be used in a further analysis.

Despite of it the presented results are still important for the observation of the degradation of photomultiplier's sensitivity. Significant difference between the illumination of photomultipliers at bottom and at the top of a camera is clearly visible.

10.1 Observation of Night-Sky Brightness

The sighting of night-sky brightness by fluorescence telescopes during clear moonless nights is shown in Fig. 10.1. Elimination of nights with the presence of the Moon gives the possibility to study the illumination of a camera (as a function of the elevation) and also light pollution from the city of Malargüe. Also runs with hardware or electronic difficulties had been excluded from the analysis.

Light pollution affects particularly the nearest FD building at Los Leones but was noticed also in the telescope 1 at Coihueco. Los Leones is situated nearly 9 km from the city. However, the field of view of just one telescope is aimed close in the direction of the city. The other five telescopes observe the sky sufficiently diverted from artificial light sources. The light pollution from the city of Malargüe has furthermore been observed only by the telescope 1 at Coihueco. The fluorescence building at Coihueco is the second closest building to the city with the distance of 30 km. Other fluorescence telescopes are not affected, either because of their distances (39 km for Los Morados and 47 km for Loma Amarilla) or their geometrical orientations.

Because of shorter observation time, the telescopes at Los Morados and Loma

Amarilla show larger fluctuations of sky brightness measured by PMTs. The same feature had been observed previously also on cameras at Los Leones and Coihueco. Such fluctuations are caused by short-time behaviour of the detector and will be smoothened after longer observation time.

10.2 Elevation Dependence

The brightness of night sky (and consequently the illumination of PMTs) decreases with the zenith angle. The illumination depends on the amount of incoming scattered light and was described for example in [Gar89]. But the illumination can be also influenced by unpredictable events, such as a dust storm or a volcano explosion.

The elevation dependence in (ADC counts)^2 averaged over the whole time of FD measurement can be seen in Fig. 10.1. This figure shows a value for each PMT. We have averaged data from all PMTs observing same zenith angle (i.e. placed in same row on different cameras). The elevation dependence of the night-sky brightness is then clearly visible, see Fig. 10.2. From the latter analysis the telescopes affected by light pollution from the town of Malargüe (i.e. telescope 6 at Los Leones and telescope 1 at Coihueco) have been excluded. The electronic noise was not subtracted, because it does not affect the shape of the dependence.

Theoretical prediction of the night-sky brightness as a function of zenith angle was given by [Gar89]. The night-sky brightness $B(\theta)$ is in the first approximation a function of a light fraction from an airglow emission (AG), and also a function of an extinction coefficient (EC) and an airmass X:

$$B(\theta) = B_0[(1-(AG)) + (AG)(1-0.96\sin^2\theta)^{-1/2}]10^{-0.4\,(EC)\,(X-1)}. \qquad (10.1)$$

The extinction coefficient is measured in U-band (in magnitude/airmass) and the airmass in the curved atmosphere is given by the following formula [Roz66]

$$X = \frac{1}{\cos\theta + 0.025\exp(-11\cos\theta)}, \qquad (10.2)$$

which gives $X = 40$ at the zenith angle $\theta = 90°$.

Measured data does not follow the theoretical function given by Eq. 10.1. The results will be recalculated for clear moonless nights defined by the measurements of the atmospheric monitoring devices in a further study.

Here, we will present results for another study, where no cut on clear moonless nights are used. In this case, all measurements with ADC variances above 8 (ADC counts)^2 and below 4,000 (ADC counts)^2 were studied. The majority of problematic periods, either those when shutters were closed or closing or PMTs on camera suffered from some problems, were filtered out due to these cuts. Two telescopes, number six in LL and number one in CO, were excluded and the ADC variances averaged over the whole measurement period of each PMT were calculated.

The illumination of the PMTs as the function of the zenith angle is depicted in figure 10.3. The median values of the ADC variances measured by all PMTs pointed into the same zenith angle show clear elevation dependence, similar to

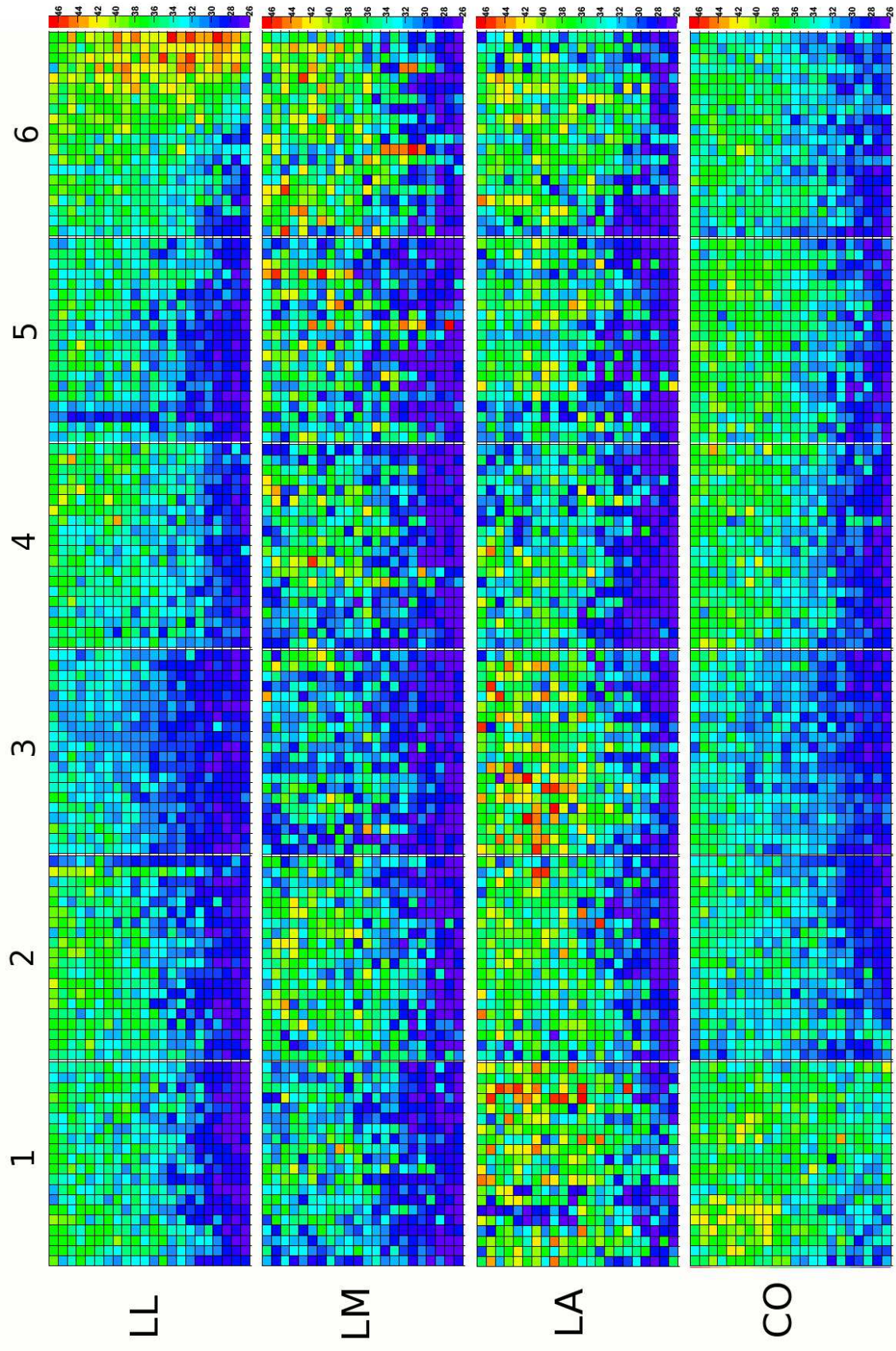

Figure 10.1: Night-sky brightness viewed by fluorescence telescopes during clear moonless nights. Logarithmic scale goes from 26 (magenta) to 47 (red) in (ADC counts)^2.

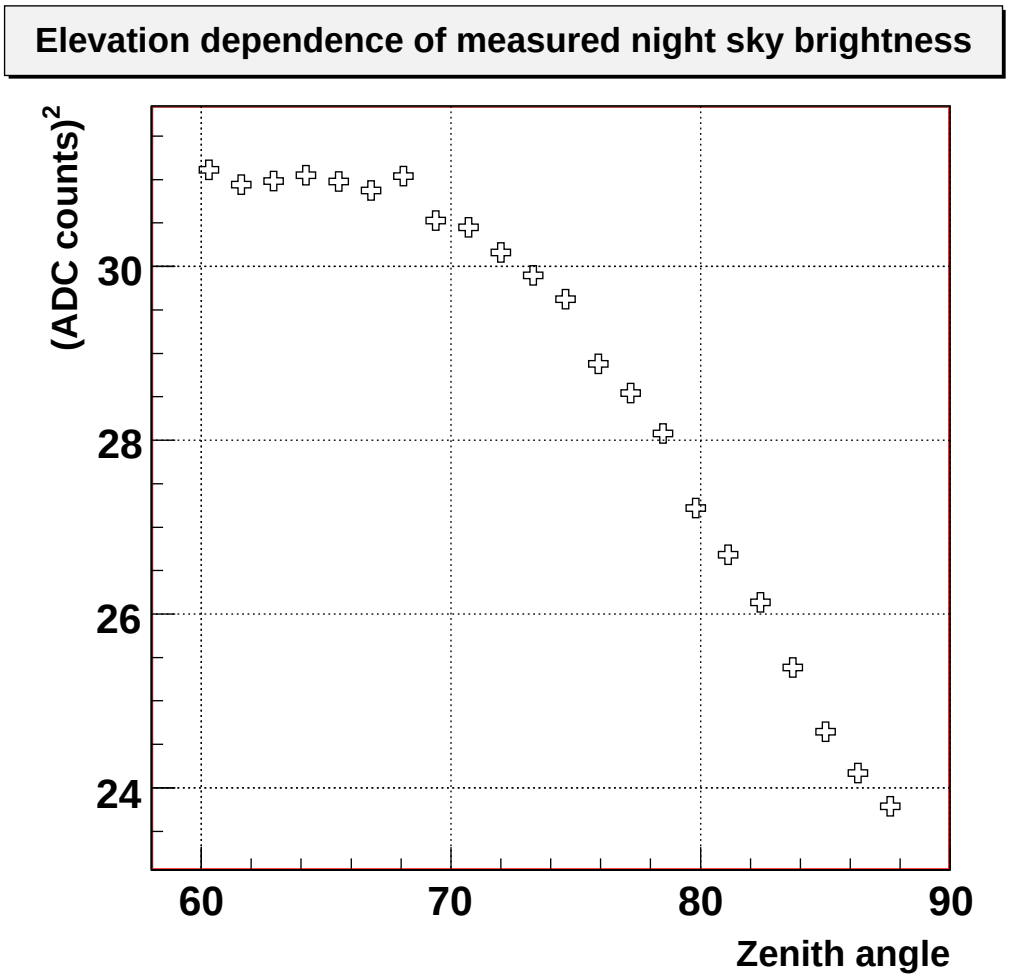

Figure 10.2: Elevation dependence of night-sky brightness for measurement during clear moonless nights. The crosses show averaged ADC fluctuations measured by FD telescopes (without LL6 and CO1).

one found in FD measurement during clear moonless night. The difference between the highest and the lowest rows of PMTs on the cameras equals to 2*(40.5-26.5)/(40.5+26.5)$\simeq$0.42. The difference of about 40% is large enough to be seen in the calibration data.

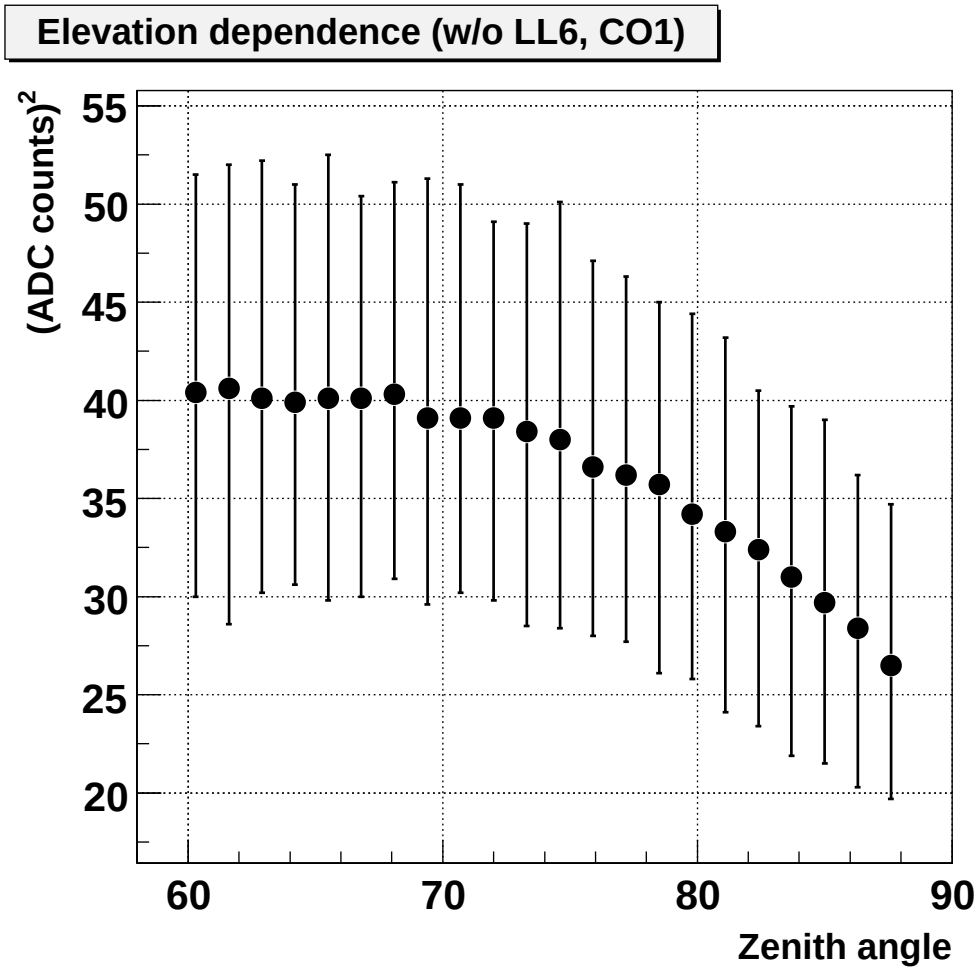

Figure 10.3: Elevation dependence of ADC variances averaged over whole measurement period of FD telescopes not affected by light pollution of city of Malargüe. Points show medians and lines indicate the 90th percentiles of values measured by studied photomultipliers.

.

Chapter 11

Conclusions

This work was focused on the most energetic cosmic rays which have been intensively studied by the Pierre Auger Observatory during last years. Author has participated in the construction of the observatory and also in the measurement during his several stays in Malargüe, Argentina. His contribution to the experiment includes also data analysis and theoretical works, which are described in this work.

The main attention has been given to the performance of the fluorescence telescopes. Uptimes and downtimes of individual telescopes were calculated (Chapter 7). These values have been successfully used to check the measurements and the identification of hardware difficulties. Particularly the interference between lidars and fluorescence telescopes was detected and promptly solved. The uptime fraction is currently well above 10% per year even after restrictions applied in the physical analysis (e.g. the calculation of hybrid spectra).

The determination of night-sky brightness suitable to fluorescence observations was studied by author. The introduction of the highest level of night-sky brightness above which the fluorescence observation is not allowed has significantly reduced the level of accumulated anode charges on the photomultipliers. The calibration results indicate the reduction of the losses of photomultiplier sensitivity since the introduction of the restriction on night-sky brightness. Moreover, the difference of about 40% was found between the illumination of photomultipliers located at the bottom and the top of a camera. The results are summarized in Chapters 8, 9 and 10.

The propagation of cosmic rays through the Galactic magnetic field have been studied and the predictions for expected angular deflections are presented in Chapter 3. The obtained results have significant consequences for any comparison of cosmic-ray arrival directions and the positions of possible astronomical sources. Our calculations show that the observed correlation is possible only for protons as the primary particles.

Furthermore the data observed by the Pierre Auger Observatory were used to search for eventual signals coming from gamma-ray sources. This study was relevant particularly for the giant flare from the magnetar SGR 1806-20 located in our Galaxy. No clear signal from gamma-ray bursts as well as for the magnetar has been identified up to now.

The results were already published and presented at conferences ([Pro03], [Boh06], [Anc07], [Boh08], [Smi09] and partially in [Abr08c]). These results are also used in several publications of the Pierre Auger Collaboration under preparation. Full list of author's publication and presentations is available at website address http://www-hep2.fzu.cz/ smida/publication.html.

Appendix A

List of Abbreviations

- ADC – analog-to-digital converter
- AGASA – Akeno giant air shower array
- AGN – active galactic nuclei
- APF – aerosol phase function
- ASS – axisymmetric
- BSS – bisymmetric
- CDAS – central data acquisition system
- CLF – central laser facility
- CMB – cosmic microwave background
- CO – Coihueco
- CR – cosmic ray
- DAQ – data acquisition
- EAS – extensive air shower
- EGMF – etragalactic magnetic field
- EeV – exa electron volt
- FD – fluorescence detector
- FLT – first level trigger
- FOV – field of view
- FRAM – fotometric robotic telescope for atmospheric monitoring
- GeV – giga electron volt

- GMF – Galactic magnetic field
- GRB – gamma-ray burst
- GZK – Greisen-Zatsepin-Kuzmin
- HAM – horizontal attenuation measurement
- LA – Loma Amarilla
- LDF – lateral distribution function
- LL – Los Leones
- LM – Los Morados
- Mpc – megaparsec
- PMT – photomultiplier tube
- SD – surface detector
- SGR – soft gamma repeater
- SUGAR – Sydney university giant air shower recorder
- T3 – third level trigger
- UHECRs – ultra-high energy cosmic rays
- VEM – vertical equivalent muon
- XLF – extra laser facility

Bibliography

[Abb05] Abbasi, R.U. et al.: Astroparticle Physics **23**, 157 (2005)

[Abbo07] Abbott, B. et al.: Physical Review D **76**, 062003 (2007)

[Abr04] Abraham, J. et al.: Nuclear Instruments and Methods in Physics Research Section A **523**, 50 (2004)

[Abr07a] Abraham, J. et al.: Astroparticle Physics **27**, 155 (2007)

[Abr07b] Abraham, J. et al.: Science **318**, 938 (2007)

[Abr08] Abraham, J. et al.: Astroparticle Physics **29**, 188 (2008)

[Abr08a] Abraham, J. et al.: Astroparticle Physics **29**, 243 (2008)

[Abr08b] Abraham, J. et al.: Physical Review Letters **100**, 211101 (2008)

[Abr08c] Abraham, J. et al.: Physical Review Letters **101**, 061101 (2008)

[Ach06] Achterberg, A. et al.: Physical Review Letters **97**, 221101 (2006)

[All05] Allard, D. et al.: Proc. of 29th Int. Cosmic Ray Conf., Pune, India (2005), arXiv:0511104

[All07] Allekotte, I. et al.: Nuclear Instruments and Methods in Physics Research Section A **586**, 409 (2008)

[Alo07] Aloisio, R. et al.: Astroparticle Physics **27**, 76 (2007)

[Anc07] Anchordoqui, L. et al.: Proc. of 30th Int. Cosmic Ray Conf., Merida, Mexico (2007), arXiv:0706.0989

[And32] Anderson, C.D.: Physical Review **43**, 491 (1932)

[And36] Anderson, C.D. and Neddermeyer, S.H.: Physical Review **50**, 263 (1936)

[Aug38] Auger, P. and Maze, R.: Compt. Rend. Acad. Sci. (Ser.II) **207**, 228 (1938)

[Aug39] Auger, P. et al.: Rev. Mod. Phys. **11**, 288 (1939)

[Bag05] Baggio, L. et al.: Physical Review Letters **95**, 139903 (2005)

[Bec96] Beck R. et al.: ARA&A **34**, 155 (1996)

[Bel78a] Bell, A.R.: Monthly Notices of the Royal Astronomical Society **182**, 147 (1978)

[Bel78b] Bell, A.R.: Monthly Notices of the Royal Astronomical Society **182**, 443 (1978)

[Ben07] BenZvi, S.Y. et al.: Nuclear Instruments and Methods in Physics Research Section A **574**, 171 (2007)

[Ben07b] BenZvi, S.Y. et al.: Astroparticle Physics **28**, 312 (2007)

[Ben07c] BenZvi, S.Y. et al.: Proc. of 30th Int. Cosmic Ray Conf., Merida, Mexico (2007), arXiv:0706.1710

[Berg06] Bergman D.R. et al.: submission to Astroparticle Physics, arXiv:astro-ph/0603797

[Ber06] Bertou X. et al.: Nuclear Instruments and Methods in Physics Research Section A **568**, 839 (2006)

[Bere04] Berezinsky, V. et al.: Nuclear Physics B (Proc. Suppl.) **136**, 147 (2004)

[Boh06] Bohačová, M. et al.: GAP note **069**, (2006)

[Boh08] Bohačová, M. et al.: GAP note **071**, (2008)

[Bir95] Bird, D.J. et al.: Astrophysical Journal **441**, 144 (1995)

[Bla78] Blandford, R.D. and Ostriker, J.P.: Astrophysical Journal **221**, L29 (1978)

[Blu70] Blumenthal, G.R.: Phys. Rev. D **1**, 1596 (1970)

[Bot29] Bothe, W. and Kolhörster, W.: Die Natur der Höhenstrahlung **17**, 271 (1929)

[Bra04] Brack, J.T. et al.: Astroparticle Physics **20**, 653 (2004)

[Car04] Caruso, R. and Petrera, S.: GAP note **072**, (2004)

[Com32] Compton, A.H.: Physical Review **41**, 111 (1932)

[Com33] Compton, A.H.: Physical Review **43**, 387 (1933)

[Cor97] Corbel, S. et al.: Astrophysical Journal **478** 624 (1997)

[Cro97] Cronin, J. et al.: Scientific American **276**, 44 (1997)

[Cro05] Cronin, J.: Nuclear Physics B **138**, 465 (2005)

[Das08] Das, S. et al.: Astrophysical Journal **682**, 29 (2008)

[Der03] Dermer, C.D. & Atoyan, A.: Physical Review Letters **91** 1102 (2003)

[Dol05] Dolag, K. et al.: Journal of Cosmology and Astroparticle Physics **1**, 9 (2005)

[Els92] Elstner D. et al.: Astronomy and Astrophysics Supplem. **94**, 587 (1992)

[Fel98] Feldman, G.J and Cousins, R.D.: Physical Review D **57**, 3873 (1998)

[Fer49] Fermi, E.: Physical Review **75**, 1169 (1949)

[Fic06] Fick, B. et al.: JINST **1** P11003 (2006)

[Gar89] Garstang, R.H.: Astronomical Society of the Pacific, Publications **101**, 306 (1989)

[Gem00] Gemmeke, H. et al.: IEEE Trans. Nucl. Sci. **47**, 371 (2000)

[Glu95] Glushkov, A.V.: Astroparticle Physics **4**, 15 (1995)

[Goc10] Gockel, A.: Physikalische Zeitschrift **11**, 280 (1910)

[Gra08] Grant, N. et al.: GAP note **002**, (2008)

[Grb] GRBlog: http://grad40.as.utexas.edu/grblog.php

[Gre66] Greisen, K.I.: Physical Review Letters **16**, 748 (1966)

[Gre] Greiner, J.: http://www.mpe.mpg.de/∼jcg/grbgen.html

[Han94] Han J.L. and Qiao G.J.: Astronomy and Astrophysics **288**, 759 (1994)

[Has92] Haswell, C.A. et al.: Astrophysical Journal **401**, 495 (1992)

[Hea88] Heavens, A.F. and Drury, L.O'C.: Royal Astronomical Society, Monthly Notices **235**, 997 (1988)

[Hes12] Hess, V.F.: Physikalische Zeitschrift **13**, 1084 (1912)

[Hil49] Hiltner, W.A.: Astrophysical Journal **109**, 471 (1949)

[Hil84] Hillas, A.M.: Annual review of astronomy and astrophysics **22**, 425 (1984)

[Iok05] Ioka, K. et al.: Astrophysical Journal **633**, 1013 (2005)

[Jel06] Jelínek, M. et al.: Astronomy and Astrophysics **454**, L119 (2006)

[Jok66] Jokipii, J.R.: Astrophysical Journal **143**, 961 (1966)

[Kam08] Kampert, K.H.: to appear in Journal of Physics, arXiv:0801.1986

[Kei04] Keilhauer, B. et al.: Astroparticle Physics **22**, 249 (2004)

[Kes05] Keshet, U. and Waxman, E.: Physical Review Letters **94**, 111102 (2005)

[Kir87] Kirk, J.G. and Schneider, P.: Astrophysical Journal **315**, 425 (1987)

[Kle73] Klebesadel, R.W. et al.: Astrophysical Journal **182**, 85 (1973) 85

[Kle03] Kleifges, M. et al.: IEEE Trans. Nucl. Sci. **50**, 1204 (2003)

[Kna07] Knapik, R. et al.: Proc. of 30th Int. Cosmic Ray Conf., Merida, Mexico (2007), arXiv:0708.1924

[Kol13] Kolhörster, W.H.G.: Ibid. **14**, 1153 (1913)

[Kro86] Kroeger, R.: Astrophysical Journal **303**, 816 (1986)

[Law91] Lawrence, M.A.: J. Phys. G **17**, 733 (1991)

[Lin61] Linsley, J. et al.: Physical Review Letters **6**, 485 (1961)

[Lin63] Linsley, J.: Physical Review Letters **10**, 146 (1963)

[McL03] McLennan, J.C. and Burton, E.F.: Physical Review **16**, 184 (1903)

[MeT97] Medina Tanco, G.A. et al.: Astroparticle Physics **6**, 337 (1997)

[Mee92] Meegan, C.A. et al.: Nature **355**, 143 (1992)

[Met97] Metzger, M.R. et al.: Nature **387**, 879 (1997)

[Mil26] Millikan, R.A.: Proceedings of the National Academy of Sciences **12** (1926)

[Nag00] Nagano, M. and Watson, A.A.: Rev. Mod. Phys. **72**, 689 (2000)

[New06] Newman, A. et al.: GAP note **090**, (2006)

[Obe07] Obermeier, A.: PhD thesis (2007)

[Obs] http://augerobserver.fzk.de

[Ost02] Ostrowski, M.: Astroparticle Physics **18**, 229 (2002)

[Pac99] Paciesas, W.S. et al.: Astrophysical Journal Supplement Series **122**, 465 (1999)

[Pal05] Palmer, D.M. et al.: Nature **434**, 1107 (2005)

[Pen65] Penzias, A.A. and Wilson, R.W.: Astrophysical Journal **412**, 419 (1965)

[Per07] Perrone, L. et al.: Proc. of 30th Int. Cosmic Ray Conf., Merida, Mexico (2007), arXiv:0706.2643

[Pro03] Prouza, M. and Šmida, R.: Astronomy and Astrophysics **410**, 1 (2003)

[Pug76] Puget, J.L. et al.: Astrophysical Journal **205**, 638 (1976)

[vRh21] van Rhijn, P. J.: Publications of the Kapteyn Astronomical Laboratory Groningen **31**, 1 (1921)

[Ris04] Risse, M.: Acta Physica Polonica B **35**, 1787 (2004)

[Ros34] Rossi, B.: Physical Review **45**, 212 (1934)

[Roz66] Rozenberg, G.V.: New York: Plenum Press, 160 (1966)

[Rut03] Rutherford, E. and Cooke, H.L.: Ibid. **16**, 183 (1903)

[Sig01] Sigl, G.: Science **291**, 73 (2001)

[Smi09] Šmída, R. et al.: GAP note **064**, (2009)

[Som01] Sommers, P.: Astroparticle Physics **14**, 271 (2001)

[Sta97] Stanev, T.: Astrophysical Journal **479**, 290 (1997)

[Sto30] Størmer, C.: Terrestrial Magnetism and Atmospheric Electricity **35** 139 (1930)

[Tho95] Thompson, C. and Duncan, R.C.: Monthly Notices of the Royal Astronomical Society **275**, 255 (1995)

[Ung07] Unger, M. et al.: Proc. of 30th Int. Cosmic Ray Conf., Merida, Mexico (2007), arXiv:0706.1495

[Ver06] Veron-Cetty, M.P. and Veron, P.: Astronomy and Astrophysics **455**, 773 (2006)

[Wax95] Waxman, E., Physical Review Letters **75**, 386 (1995)

[Wax00] Waxman, E. & Bahcall, J.: Astrophysical Journal **541**, 707 (2000)

[Wdo72] Wdowczyk, J. et al.: J. Phys. A **5**, 1419 (1972)

[Win86] Winn, M.M. et al.: J. Phys. G: Nucl. Phys. **12**, 653 (1986)

[Woo06] Woods, P.M. et al.: Astrophysical Journal **654**, 470 (2006)

[Wul09] Wulf, T.: Physikalische Zeitschrift **10**, 152 (1909)

[Zat66] Zatsepin, Z.T. and Kuzmin, V.A.: Zh. Eksp. Teor. Fiz. Pisma Red. **4**, 144 (1966)